

ANALYTICAL MODELING AND DESIGN OPTIMIZATION OF PIEZOELECTRIC  
BIMORPH ENERGY HARVESTER

by

LONG ZHANG

A DISSERTATION

Submitted in partial fulfillment of the requirements  
for the degree of Doctor of Philosophy in the  
Department of Mechanical Engineering  
in the Graduate School of  
The University of Alabama

TUSCALOOSA, ALABAMA

2010

Copyright Long Zhang 2010  
ALL RIGHTS RESERVED

## ABSTRACT

As wireless sensor networks continue to grow in size and scope, the limited life span of batteries produces an increasingly challenging economic problem, in terms of not only the capital cost of replacing so many batteries, but also the labor costs incurred in performing battery replacement, particularly with sensor nodes in remote or limited-access locations. This growing problem has motivated the development of new technologies for harvesting energy from the ambient environment. Piezoelectric energy harvesters (PEH) are under consideration as a means for converting mechanical energy, specifically vibration energy, to electrical energy, with the goal of realizing completely self-powered sensor systems. There are three primary goals with regards to this study. The first goal is to develop an analytical model for the resonant frequency of a piezoelectric cantilever bimorph (PCB) energy harvester, aiming to study the geometric effects of both the piezoelectric bimorph and the proof mass on the resonant frequency of a PEH. The analytical model is developed using the Rayleigh-Ritz method and Lagrange's equation of motion and is validated by finite element analysis (FEA) and laboratory experiments. It is shown that this analytical model is better at predicting resonant frequencies than a model currently available in the literature. The second goal is the development of an enhanced analytical model for the voltage and power output of the PCB. The modified analytical model is realized using the conservation of energy method and Euler-Bernoulli beam theory. It is compared with a general equivalent spring-mass-damper model and an equivalent electrical circuit model, and validated by the laboratory prototype experiments. The results show that the modified model provides improved prediction of PCB voltage and power output. Simultaneously, finite element analysis

on piezoelectric structures using the commercially available software package ANSYS®

Multiphysics is also carried out to study the dynamic response of the PCB in terms of both tip displacements and the electrical potentials of the top and bottom electrodes. It is shown that the simulations are quite close to the experimental results, in terms of both peak frequencies and peak amplitudes. The third goal is the design optimization of the PCB energy harvester in order to maximize the power harvesting from the ambient vibration. Three design optimization approaches are carried out, including multi-parameter optimization of the single PCB generator using a genetic algorithm (GA), a band-pass generator design with a group of the PCB generators based on the system transfer function, and the new design features of the PCB generator for consideration of the improvements of the strain energy and the lifetime. The results of the optimized designs are validated through FEA, and the discrepancies between the theoretical derivation and FEA are also analyzed. Other optimal design considerations are also discussed.

DEDICATION

To my family

## LIST OF ABBREVIATIONS AND SYMBOLS

$A_{in}$	Amplitude of the input acceleration
$c_p$	Young's modulus of the piezoelectric material
$c_{sh}$	Young's modulus of the central shim layer
$C_b$	Capacitance of the piezoelectric bimorph
$d_{31}$	Piezoelectric strain coefficient (Poled direction: 3, strain direction: 1)
$d_{33}$	Piezoelectric strain coefficient (Poled direction: 3, strain direction: 3)
FEA	Finite element analysis
GA	Genetic algorithms
$h_m$	Thickness of the proof mass
$L$	Length of the piezoelectric bimorph
$L_m$	Length of the proof mass
$k_{31}$	Coupling coefficient
PCB	Piezoelectric cantilever bimorph
$R$	Resistive load
$t_p$	Thickness of the piezoelectric bimorph
$t_{sh}$	Thickness of the central shim layer
$w_m$	Width of the proof mass
$w_p$	Width of the piezoelectric bimorph

$Y$	Tip displacement of the PCB
$\varepsilon$	Piezoelectric dielectric constant
$\varepsilon_0$	Vacuum dielectric constant
$\zeta$	Damping ratio
$\rho_m$	Density of the proof mass
$\rho_p$	Density of the piezoelectric bimorph
$\rho_{sh}$	Density of the central shim layer
$\omega$	Driving frequency
$\omega_n$	Resonant frequency

## ACKNOWLEDGMENTS

I would like to express my deepest gratitude to Dr. Keith A. Williams for his warm-hearted academic, technical, and financial support during my study and research. His leadership and broad knowledge initiated and play an important role in this research work. Furthermore, I would like to express my sincere appreciation for his precious support for my family.

I also appreciate support from the committee: Dr. Joey K. Parker, Dr. W. Steve Shepard Jr., Dr. Xiangrong Shen and Dr. Jaber A. Abu Qahouq for teaching me the requisite classes and spending their valuable time reviewing and commenting on my dissertation.

My thanks also go out to my colleagues in the department of mechanical engineering: Minjae Jung, Zhengchao Xie, Jianwen Hu, and Feng Qin, for their friendship and technical discussion.

Finally, I need to acknowledge Yi Fan, my wife, for her continuous support and understanding during my tough times prior to completing this dissertation. I dedicate this work to my family.

## CONTENTS

ABSTRACT.....	ii
DEDICATION.....	iv
LIST OF ABBREVIATIONS AND SYMBOLS .....	v
ACKNOWLEDGMENTS .....	vii
LIST OF TABLES .....	xi
LIST OF FIGURES .....	xii
CHAPTER 1. INTRODUCTION .....	1
CHAPTER 2. LITERATURE REVIEW .....	9
Ambient Energy Sources .....	9
Solar Energy.....	10
Wind Energy .....	10
Water Flow Energy .....	11
Temperature Gradient .....	11
Mechanical Vibration.....	12
Acoustic Wave .....	13
Conversion Mechanisms of Vibration to Electricity .....	13
Electromagnetic .....	13
Electrostatic Devices.....	15
Piezoelectric Devices .....	17
Summary of Conversion Mechanisms .....	20

Configuration and Modeling of PEH.....	21
Piezoelectric Stack Converter.....	22
Piezoelectric Bender Converter.....	23
Analytical Models for Piezoelectric Energy Harvester.....	25
Summary.....	29
<b>CHAPTER 3. ANALYTICAL MODELING OF RESONANT FREQUENCY OF PCB GENERATOR.....</b>	<b>31</b>
Modeling of Resonant Frequency of PCB Generator.....	31
PCB Generator Configuration.....	31
A Previous Model for PCB Resonant Frequency.....	35
A New Frequency Model for PCB Generator.....	36
A Simplified Model for PCB Tip displacement.....	38
Geometric Effect on the Resonant Frequency.....	40
Geometric Effect of the Bimorph.....	43
Geometric Effect of the Proof Mass.....	45
Experimental Validation of Frequency Model and Tip Displacement Model.....	48
Experimental Results of the Resonant Frequency.....	49
Experimental Results of the Tip Displacement.....	51
Summary.....	53
<b>CHAPTER 4. ANALYTICAL MODELING FOR PCB ENERGY HARVESTER.....</b>	<b>54</b>
Previous Models for Power Output of PCB Generator.....	54
Mechanical Equivalent Spring-Mass-Damper Model.....	55
Electrical Equivalent Circuit Model.....	58
A Modified Analytical Model for PCB Generator.....	60

Experimental Validation and Model Comparison .....	68
Open-Circuit Voltage.....	70
Close-Circuit Voltage .....	73
Power Output .....	76
Summary .....	78
<b>CHAPTER 5. FINITE ELEMENT ANALYSIS FOR THE DYNAMIC RESPONSES OF PCB GENERATOR.....</b>	<b>80</b>
Piezoelectric Analysis in ANSYS®.....	80
FEA and Experimental Validation.....	83
Tip Displacement.....	85
Open-Circuit Voltage.....	88
Summary .....	92
<b>CHAPTER 6. DESIGN OPTIMIZATION OF PCB GENERATOR.....</b>	<b>93</b>
Genetic Algorithm Optimization of a Single PCB Generator .....	93
Band-pass Design Optimization of PCB Generators .....	103
Band-pass Design of PCB Energy Harvesters .....	104
FEA Validation of Band-pass Generator Design.....	108
Geometric Feature Design Optimization .....	112
Summary .....	116
<b>CHAPTER 7. CONCLUSIONS AND RECOMMENDATIONS .....</b>	<b>118</b>
Conclusions.....	118
Recommendations for Further Studies.....	119
<b>REFERENCES .....</b>	<b>122</b>

## LIST OF TABLES

Table 1 Pros and Cons of Three Conversion Mechanisms, Roundy (2003A & 2004).....	20
Table 2 Specific Dimension of Q220-A4-203Y .....	40
Table 3 PZT Properties of Q220-A4-203Y, Piezo System.....	41
Table 4 Material Properties of the Proof Mass, MatWeb.com .....	45
Table 5 Specific Data of Three Models and Experiment.....	50
Table 6 Design Variables for Optimization .....	96
Table 7 Optimized Design Parameters and Outputs for a Single PCB Generator.....	99
Table 8 Optimized Parameters and Outputs under Additional Constraints.....	100
Table 9 Theoretical Dimensions of a Band-pass Generator with $\gamma = 1.53$ .....	109

## LIST OF FIGURES

Figure 1. Advances in computer and battery technology since 1990 (Paradiso & Starner, 2005).	2
Figure 2. Generic Electromagnetic Generator Model, Cao et. al (2007).....	14
Figure 3. Variable Capacitor Schematic, Chiu, Kuo, and Chu (2007). ....	16
Figure 4. Piezoelectric Transducers, Priya (2007).....	18
Figure 5. Orthogonal Coordinate System and Poling-Stress Direction. ....	22
Figure 6. Piezoelectric Stack Energy Harvester. ....	23
Figure 7. 31-Type Piezoelectric Bender Converter. ....	24
Figure 8. 33-Type Piezoelectric Bender Converter. ....	24
Figure 9. A Schematic Diagram of a PCB Generator.....	32
Figure 10. Compression Mode and Tension Mode of PZT Layer.....	33
Figure 11. Series Poling and Parallel Poling. ....	34
Figure 12. An SDOF Model of PCB Generator, Ng & Liao (2005).....	38
Figure 13. Shape and Dimension of Q220-A4-203Y, Piezo System.....	40
Figure 14. First 6 Modes of PCB Generator.....	42
Figure 15. Length Effect of the Bimorph on the Resonant Frequency.....	43
Figure 16. Thickness Effect of the Bimorph on the Resonant Frequency.....	44
Figure 17. Weight Effect of the Proof Mass on the Resonant Frequency. ....	46
Figure 18. Length Effect of the Proof Mass on the Resonant Frequency.....	47
Figure 19. A Prototype of PCB Energy Harvester.....	48
Figure20. Experimental Procedures of PCB Energy Harvester.....	49

Figure 21. The Resonant Frequency Results by Models and Experiment.....	50
Figure 22. Tip Displacement Results of SDOF Model and Experiment. ....	52
Figure 23. Experimental Results of Tip Displacement vs. Resonant Frequency.....	52
Figure 24. A General Model for Vibration Energy Conversion (Williams & Yates, 1996).....	55
Figure 25. Open-circuit Model of Piezoelectric Energy Harvester .....	57
Figure 26. Close-circuit Model of Piezoelectric Energy Harvester.....	58
Figure 27. A Schematic Diagram of the Generator, Roundy (2004). ....	59
Figure 28. Circuit Representation of the Piezoelectric Generator, Roundy (2004).....	59
Figure 29. Top Surface Equivalent Elastic Strain of PCB Generator.....	62
Figure 30. Bottom Surface Equivalent Elastic Strain of PCB Generator. ....	62
Figure 31. Top Surface Equivalent Strain of PCB Generator with Longer Proof Mass.....	63
Figure 32. Bottom Surface Equivalent Strain of PCB Generator with Longer Proof Mass. ....	63
Figure 33. A Schematic Diagram of the Experiment Setup.....	69
Figure 34. An Example of the Impulse Response of the PCB Generator.....	70
Figure 35. Open-circuit Voltage of the Modified Model and Kim's Model. ....	71
Figure 36. Open-circuit Voltage Amplitude Comparison of Three Models.....	72
Figure 37. Close-circuit Voltage of Kim's Model and the Modified Model. ....	74
Figure 38. Close-circuit Voltage Comparison of Three Models.....	75
Figure 39. Power Output Comparison of Three Models.....	77
Figure 40. Finite Element Distribution of PCB Generator. ....	85
Figure 41. Harmonic Responses of the Prototype Tip Displacement.....	87
Figure 42. Experimental Harmonic Response of Open-circuit Voltage. ....	88
Figure 43. Finite Element Harmonic Analysis of PCB Generator in 0 ~ 2000 Hz.....	89

Figure 44. Harmonic Responses of the Prototype Open-circuit Voltage.....	90
Figure 45. Electrical Potential Distribution of the Piezoelectric Bimorph. ....	91
Figure 46. Basic Procedure for Genetic Algorithm (Xie, 2008).....	94
Figure 47. Formulation of Optimization Problem. ....	97
Figure 48. GA Optimization of PCB Generator with $t_p = 0.139mm$ . ....	101
Figure 49. GA Optimization of PCB Generator with $t_p = 0.191mm$ . ....	101
Figure 50. GA Optimization of PCB Generator with $t_p = 0.278mm$ . ....	102
Figure 51. Ambient Vibrations from Motor Hood and Inside Panel. ....	104
Figure 52. A Band-pass Filter and Its Frequency Response, Shahruz (2005). ....	105
Figure 53. Theoretical Bode Plot of the Band-pass Generator with $\gamma = 1.53$ . ....	110
Figure 54. Normalized Frequency Response of the Band-pass Generator FEA Simulation. ....	111
Figure 55. Two Geometric Configurations of PCB Generators. ....	112
Figure 56. Equivalent Strain Distribution of 1 <sup>st</sup> PCB Generator Design. ....	113
Figure 57. Equivalent Strain Distribution of 2 <sup>nd</sup> PCB Generator Design. ....	114
Figure 58. Two Geometries of PCB Generators. ....	115
Figure 59. Equivalent Strain Distribution of 3 <sup>rd</sup> PCB Generator Design. ....	115
Figure 60. Open-circuit Voltage Comparison of Three PCB Generator Designs.....	116

## CHAPTER 1

### INTRODUCTION

In the modern world, technology is becoming more capable, and its geometric “footprint” is becoming smaller and smaller. Portable electronics are ubiquitous, and wireless sensor nodes are expanding as never before. The overwhelming majority of electronic devices rely on the use of electrochemical batteries to provide electrical energy. Battery energy density also continues to improve significantly; however, that improvement has not matched the development of other computationally-related electronics elements. For example, as is shown in Figure 1 by Paradiso and Starner (2005), between 1990 and 2003, the disk capacity was increased by a factor of more than 1000 and the CPU speed was increased by almost as much, while the battery energy density was only increased about three times during the same period.

As society’s performance expectations and reliance on technology have increased, the issue of battery replacement has become more important. With more and more electronics embedded in the civil infrastructure and distributed in remote or limited-access areas, the limited life span of batteries produces an increasingly challenging problem, both in terms of capital and labor costs in performing battery replacement, but also in terms of basic technical difficulties, such as the replacement of batteries for electronics embedded inside of structural members.

In an effort to reduce dependence on batteries and to extend the operating life of electronic systems with limited access, researchers have begun investigating methods of obtaining electrical energy from ambient energy, with the long-term goal of realizing completely

self-powered systems. There are five major categories of ambient environment energy: solar energy, thermal energy, wind energy, acoustic noise, and mechanical vibrations.

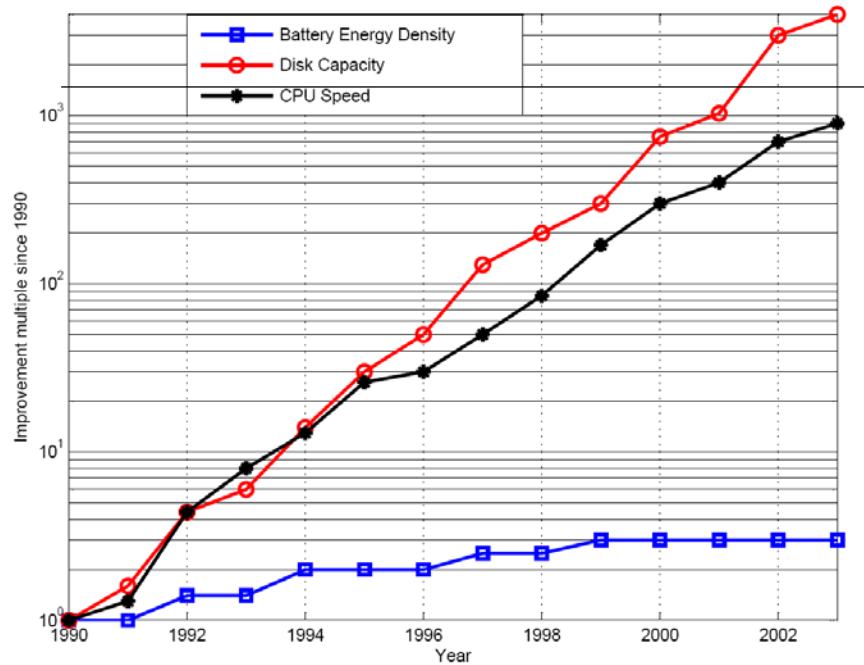


Figure 1. Advances in computer and battery technology since 1990 (Paradiso & Starner, 2005).

Solar energy is a very attractive source for powering electronics and has become more mature over the years. However, certain limitations remain: light intensity can drop significantly during cloudy weather, and relatively large surface areas may be required, depending on the power requirements of the associated electronic system. Thermoelectric energy requires large temperature differentials to provide significant amounts of electrical energy. Wind energy is also an attractive source for electricity, and many windmill generators have been distributed to coastal and mountain areas, where strong winds are common. However, the use of windmills to power individual small electronic systems is of questionable practicality. Noise energy harvesting requires high noise levels and is very sensitive to the direction of noise propagation.

Mechanical vibrations are found almost everywhere humans are present, in the running automobiles, appliances, bridges, air ducts, railways, and buildings. To a certain extent, people's

walking, breathing, and beating heart also generate vibrations, which may provide alternative sources for the harvesting of mechanical vibration energy.

There are two major groups of mechanical vibration energy harvesters. One is the non-resonant device, which is mostly applied to very low frequency vibrations and outputs relatively little electrical energy. The other is the resonant device, which could generate relatively high electrical energy and will be the main focus in this study. Several conversion mechanisms exist for obtaining electrical energy from vibration sources, including the use of electromagnetic induction, electrostatic generators, and piezoelectric materials. While all of the above conversion mechanisms may convert a certain amount of electrical energy from vibrations, the piezoelectric generator receives the most attention, because it directly converts strain energy into electrical energy using the piezoelectric effect. Further, piezoelectric devices can often be made small enough to be integrated into existing systems. Further, with no moving parts, the lifetime of the piezoelectric generator is almost unlimited, if the applied vibrations and external temperatures are within certain bounds. In addition, it has a relatively high power density and does not need an external voltage source to get the energy conversion started.

Energy generation in a piezoelectric energy harvester (PEH) is due to strain of the material. To realize sufficient strain to generate the desired electrical power, a PEH may be bonded to vibrating structures such as bridges, air ducts, buildings, and aircraft. Piezoelectric materials can be manufactured in many different configurations that prove useful in energy harvesting applications. The configuration of the energy harvesting devices can be changed through modification of piezoelectric materials, alteration of the electrode pattern, changing the poling and stress directions, the addition of a proof mass to maximize the coupling and applied strain of the material, and tuning the resonant frequency of the device in order to maximize the

harvested power for a given application.

The piezoelectric cantilever bimorph (PCB) is perhaps the simplest and most widely used configuration for a piezoelectric generator. It is typically a cantilevered 3-layer beam with two piezoelectric layers bonded to the top and bottom surfaces of a central brass layer. The brass layer is used to increase the elasticity of the structure due to the brittleness of the piezoelectric materials. Further, a proof mass is usually bonded to the tip end of the bimorph to increase the applied strain during vibrations. In this configuration, the resonant frequency of the PCB structure could be readily tuned by simply modifying the proof mass. This would allow for tuning the PCB resonant frequency to match the frequency of the ambient vibrations, causing larger structural deformations and more strain which, in turn, will produce more electrical energy for a given input.

In an effort to maximize the potential of a PCB energy harvester to generate electrical energy, it is necessary to study the theoretical relationship between its geometric configuration and its voltage and power output for a given ambient vibration condition. Numerous approaches have been developed for predicting the behavior of a PCB energy harvester, most of them based on models of piezoelectric actuators. To the best knowledge of the author, the invention and application of piezoelectric unimorph and bimorph actuators can be traced back to Baldwin (1931). Since then, a great deal of research has been done to improve analytical modeling of such devices. Many of the more recent approaches are derived based on the constitutive relations derived by Smits (1991), describing the behavior of a cantilever bimorph under static conditions. More details on the analytical modeling of piezoelectric actuators and sensors will be provided in Chapter 2. The main difference between piezoelectric materials as actuator elements and as energy harvesting elements is the geometric configuration. For the latter, a proof mass is usually

used to work as prestress and aims to increase the strain energy of PEH during the dynamic movement. Therefore, it would be useful to consider the geometric configuration effects of both piezoelectric bimorph and proof mass on the resonant frequencies and power outputs of PEH. To that end, the first goal of this research is to completely study the effect of PEH geometry on the device resonant frequency. This study will be carried out first by obtaining the equations for the motion of a three-layer beam with a tip proof mass using the Rayleigh-Ritz method and Lagrange's equation of motion. The analytical model will then be compared with a frequency comparable model available in the literature. Further, a finite element analysis using the commercially available software ANSYS<sup>®</sup> will also be performed to provide an alternate method for studying the effect of piezoelectric bimorph geometry and proof mass on the resonant frequency of the structure. Once this issue has been addressed, the analytical model will be available for use as a design tool.

For a piezoelectric energy harvester, a reasonable goal is to maximize the amount of energy produced for a given ambient vibration condition. Therefore, the second goal of the proposed research is to study the effect of PCB energy harvester geometry on the corresponding voltage and power output. A modified analytical model based on the previous studies is proposed, for both open-circuit and closed-circuit conditions. The modified model may give better results than the previous models; however, it also has limitations when compared with finite element analysis. In the design of more complex PEH structures, finite element analysis is preferred, as traditional analytical modeling for such structures may be impractical. As a result, more design options can be considered to study the behavior of PEH electrical energy generation.

After the geometric effects of the PCB energy harvester on its resonant frequency and power output are studied, it is natural to consider design optimization. To that end, another goal

of this study is to develop design optimization tools that will allow for design of a PCB energy harvester to obtain the maximum amount of electrical energy for a given ambient vibration condition. For the design optimization of a single PCB energy harvester working under the ambient vibration with a single fixed frequency, a genetic algorithm (GA) is proposed. A GA has advantages when compared to more traditional optimization techniques, in terms of the handling of constraints and multi-variable optimization, assuming, of course, that the analytical models are acceptable. For ambient vibrations with a certain frequency band, the band-pass design optimization approach based on the system transfer function is applicable by appropriately choosing the geometric configuration of each PCB among the PCB ensemble.

To realize the aforementioned goals, the research work will involve the development of (1) an analytical model of the resonant frequency of the PCB energy harvester, (2) a modified analytical model for the voltage and power output of the PCB energy harvester, (3) finite element analysis of PCB structural responses and piezoelectric responses, and (4) design optimization of PCB working under different ambient vibrations. The organization of this dissertation is summarized as follows:

Chapter 2 is the literature review, in which ambient sources for energy harvesting are first briefly introduced, and three mechanisms for converting vibration energy to electrical energy are also discussed. The principle and classification of piezoelectric energy harvesting are then presented, along with a discussion of previous modeling techniques for piezoelectric bender energy harvesters.

Chapter 3 presents the development of the analytical model for the resonant frequency of a three-layer PCB energy harvester using the Rayleigh-Ritz method and Lagrange's equations. The model is then compared with both a finite-element model and an analytical model obtained

from the literature. The model is then exercised to study the relations between the PCB geometry and proof mass and the corresponding device natural frequency.

In Chapter 4, the modified analytical model that provides the voltage and power output of a PCB energy harvester is discussed. The modified model assumes that piezoelectric materials under the proof mass do not experience the dipole deformation and thus do not generate a charge that could be collected and used for energy harvesting. That assumption is justified, as the results of the finite element analysis indicated that the strain under the proof mass is relatively small. Furthermore, through comparison with two previous models available from the literature, the modified model is partially validated, although some differences between the model and experiments exist.

Chapter 5 presents the finite element analysis of dynamic responses of PCB energy harvesters under harmonic excitations by using ANSYS®. The tip deflection and strain-induced electrical potential are validated through laboratory experiments performed using a commercially available PCB. Compared with analytical models, FEA with ANSYS® could analyze more complex design structures, and it could be used as a validation tool for future design optimizations.

Chapter 6 discusses the design optimization of PCB energy harvesters under three categories, including the multi-parameter optimization of a single PCB generator using a GA, the band-pass generator design with a group of PCB generators, and the new feature designs of the PCB generator for consideration of the improvement of electrical energy conversion and the life time of the PCB generator. Further, the electrical circuit optimizations, such as energy storage and duty cycle, are also discussed.

Chapter 7 summarizes the current research work and provides recommendations for

future work. Such recommendations include the development of a plate model for better prediction of the behavior of PCB generators with smaller length-to-width ratios. Such configurations cannot be accommodated by models based on the Euler-beam theory. Other recommendations include the active frequency tuning of a PCB energy harvester to match the frequency of ambient vibrations and the study and design optimization of energy harvesting using nano-tube transducers or nano-tube reinforced PZT transducers.

## CHAPTER 2

### LITERATURE REVIEW

With the technology advances in micro electro-mechanical systems (MEMS) and wireless sensor networks, the demand for portable electronics and wireless sensors is growing rapidly. These devices could be distributed to remote areas in such varied applications as structural sensors monitoring bridge vibration, gas monitors in a coal mine, and even wild animals as a global positioning system (GPS). In many such applications, limited access may make battery replacement excessively costly, impractical, or even impossible. Examples include devices in remote locations or devices embedded inside of civil structures. By harvesting energy from the surrounding environment, the time between battery replacements may be extended or even eliminated, depending on the power requirements of the specific application. To that end, a discussion of ambient energy sources is appropriate.

#### **Ambient Energy Sources**

Several energy sources may be directly available in a given environment, including solar, wind, water flow, temperature gradients, mechanical vibrations and acoustic waves, etc. Of course, not all such sources are available in every particular locale. Further, of the sources available in a single location, one source may have some special advantage over the others, although it is certainly possible that multiple energy sources could be utilized simultaneously if appropriate. It is important that the information regarding source capabilities and limitations are gathered. Their specific characteristics are briefly addressed as follows.

## **Solar Energy**

As an ubiquitous and renewable energy source on earth, solar energy is very attractive, and the associated technology has matured over the years. Solar technology involves the use of photovoltaic panels and solar thermal collectors to harness the radiant light and heat from the sun. According to the assumption of the U.S. Department of Energy (2006), if every single family in America had a 3 kW photovoltaic system on the roof of their home, grid-provided residential electrical energy could be reduced by more than 35% with solar energy. Under strong sunlight at mid-day, solar cells have the capability of providing a power density of  $15,000 \mu W / cm^2$  (Roundy, 2005), which can be enough for some microelectronics working intensively and power-independently outdoors (Priya, 2007). Although the prospects for growth in solar energy are significant, the low conversion efficiencies of silicon solar cells, coupled with the cost of R&D, manufacturing improvements, and installation need to be improved.

## **Wind Energy**

Wind energy can be harvested by modern wind turbines, which rotate a shaft connected to a generator. As an alternative to fossil fuels, wind energy is also renewable, clean, and widely distributed, and it has accumulated large investment and development over the years. According to WWEA (2009), world-wide wind-powered generator capacity was 159.2 gigawatts (GW) at the end of 2009, which was approximately 2% of worldwide electricity usage. Wind speed is an important parameter of wind resources, since wind energy is proportional to the cube of wind speed. As a result, most of large-scale wind farms are installed at mountains and off-shore areas and are connected to the electric power transmission network. Recently, Priya (2005) and Chen and Priya (2006) demonstrated that small-scale electrical energy can be harvested from wind using piezoelectric bimorph transducers, which are mounted as fan blades. The power density is

approximately  $4.17 \mu W / cm^3$ . However, two major challenges in the energy harvesting application of wind turbines are cost and supply and transportation. Further, the scale of wind turbines is of questionable practicality and feasibility for portable electronics.

### **Water Flow Energy**

Water flow energy or hydroelectric power is currently the predominant renewable energy. It accounted for 6% of total U.S. electricity generation and 67% of generation from renewable energies in 2008, according to the U.S. Energy Information Administration (EIA, 2009). Since water is approximately 800 times denser than air, water flow can yield considerable amounts of energy. The available water energy for turbine is mainly determined by water flow speed; thus, hydroelectric dams are commonly built in areas with high altitude descending. As in the past, hydroelectric power will continue to be a significant source in the electricity industry. However, the hydroelectric dams cause a manifest environmental impact. In addition, the water flow requirement constrains this energy source in the applications of energy harvesting for MEMS and wireless sensor systems.

### **Temperature Gradient**

Temperature gradient and heat flow is ubiquitous in natural environments and human-made settings, and it can be converted to electric voltage by thermoelectric devices, in which the temperature gradient causes charged carriers (electrons or holes) in the materials to diffuse from hot places to cold places (Wikipedia: Thermoelectric effect). Stordeur and Stark (1997) demonstrated a thermoelectric micro-device capable of generating  $15 \mu W / cm^3$  from a  $10^\circ C$  temperature gradient. Particularly, human body heat provides a potential for generating electrical energy to power medical devices, body implants, personal wireless sensors, and other

consumer devices. Roundy (2005) reported some commercially available clocks utilizing harvested energy from the thermoelectric effect of a sealed volume of fluid that undergoes a phase change right around room temperature. However, the harvested electrical energy from the thermoelectric effect is substantially low, except for systems with very large temperature gradients.

### **Mechanical Vibration**

Mechanical vibration is plentiful in human-made settings, with sources such as rotating machines, vibrating air ducts, operating motors, various appliances, and civil structures such as bridges and buildings. The vibration energy can be harvested as electrical energy by several conversion methods, such as electromagnetic, piezoelectric, and electrostatic devices, which will be discussed in the next section. Roundy (2003A) measured a variety of vibrations sources in our daily lives, including car engines, a blender, a clothes dryer, a small microwave oven, HVAC vents in an office building, and the second story floor of a busy office. In each of those locations/devices, the vibrations were dominantly in the range of 0-200 Hz and classified as “low level” vibrations, as compared to higher level vibrations that may occur around large industrial equipment. Roundy concluded that the fundamental resonant frequency of the low-level vibration energy harvester should match the ambient vibration in order to obtain maximized power. He also showed that about  $375 \mu W / cm^3$  could be generated from an optimized configuration of the piezoelectric energy harvester. Further, according to Roundy, if the projected lifetime of a device is more than a few years, energy harvesting via vibration conversion may be a more economical alternative than batteries.

## **Acoustic Wave**

Acoustic waves or noise can also be readily found in locations such as highways, airports, and factories. Although it is extremely undesirable, it has the property of being harvested as electrical energy to power sensor nodes using wave localization effect and direct piezoelectric effect. However, except for in ambient environments with extremely high-level noise, the available energy from acoustic noise is too little to be of practical use. For example, Horowitz et al. (2006) measured the feasible power density of an acoustic energy harvester to be approximately  $0.34 \mu W / cm^2$  for an incident sound pressure level of  $149 dB$  (ref.  $20 \mu Pa$ ). Such energy density is not sufficient to provide practical power for MEMS systems, which require  $10 - 100 \mu W$ , according to Jeon et al. (2005).

In a word, there may be numerous available energy sources in a given environment. Each source may provide useful energy under specific conditions. In this study, we will focus on energy harvesting from mechanical vibrations. Different conversion mechanisms and their pros and cons will be discussed first.

### **Conversion Mechanisms of Vibration to Electricity**

There are three main mechanisms used to convert vibrational energy to electrical energy: electromagnetic, electrostatic, and piezoelectric. In this section, previous research on these conversion mechanisms is reviewed.

#### **Electromagnetic**

An electromagnetic energy harvester converts vibration into electrical energy using the relative motion between wire coils and a magnetic field. According to Faraday's Law of Induction, the electromotive force (EMF) induced in a coil is directly proportional to the time

rate of change of magnetic flux through the coil. There are two ways to change the magnetic flux through a coil: one is to vary the magnetic field and the other is to move the coil through a fixed magnetic field. The latter approach is the most common way to realize vibration-to-electrical energy harvesting. A typical electromagnetic generator, taken from Cao et. al (2007), is shown in Figure 2, where the permanent magnet crosses the coils due to the base excitation, and the vibration energy is converted to the electrical energy based on the Farady's Law.

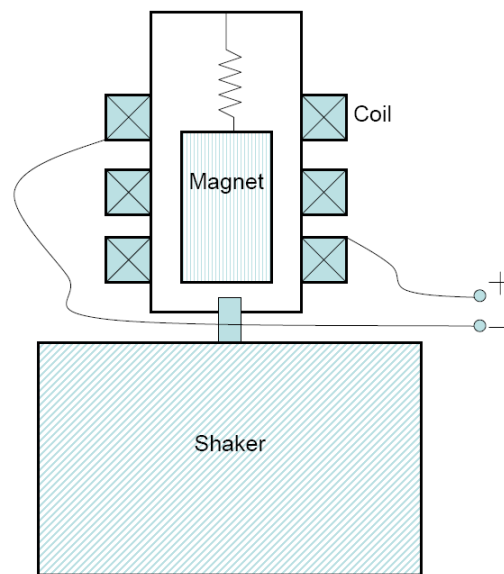


Figure 2. Generic Electromagnetic Generator Model, Cao et. al (2007).

Williams and Yates (1996) developed a general model for the vibration-to-electricity conversion mechanism, Their testing electromagnetic generator had dimensions of  $5mm \times 5mm \times 1mm$  , and power levels of  $1 \mu W$  at 70 Hz and  $0.1 mW$  at 330Hz were predicted.

Amirtharajah and Chandrakasan (1998) developed a vibration-based electromagnetic generator to power a digital signal processor. The vibration source is provided by human walking, with magnitude of  $2 cm$  around  $2 Hz$  . The result showed that a power of  $400 \mu W$  could be generated.

Roundy (2003B) developed an electromagnetic generator and tested it using vibrations with acceleration amplitudes of  $2.25 \text{ m/s}^2$  at 120 Hz. The result showed that 15 to 30  $\text{mV}$  can be produced for the maximum device size of  $1 \text{ cm}^3$ , by current technology. However, he pointed out that the generated AC voltage would be smaller than the diode voltage drop of 0.5 volts. Such a signal cannot then be directly converted to a DC voltage using a standard rectifier. Therefore, it would be impossible to implant such a generator in the small volume desired for powering microelectronics without the voltage amplification.

One advantage of the electromagnetic energy harvesters is that the design process of electromagnetic generators would not require mechanical contacts among the components (permanent magnet and coil) and thus could reduce friction losses and improve reliability. However, the generated voltage of the electromagnetic generator is too low to be used for MEMS and other electronics. In addition, a strong magnet must be manually integrated to the device and will thus increase the overall weight of the device.

### **Electrostatic Devices**

Electrostatic energy harvesters convert vibration energy to electrical energy through the relative motion of the parallel plates of the capacitor. One typical variable capacitor, taken from Chiu, Kuo, and Chu (2007), is shown in Figure 3, where the relative motion between upper plates (displacement  $y$ ) and lower plates (displacement  $z$ ) due to vibration leads to capacitance changes between any two adjacent capacitors. In such a device, if the voltage across the capacitor is constrained, an extra charge will be generated as the capacitance of the variable capacitor increases. Alternately, if the charge on the variable capacitor is constrained, a capacitance decrease will lead to a voltage increase across the capacitor. In either case, an initial charge or voltage is needed to start the conversion and vibration of the plates then allows for

harvesting of electrical energy.

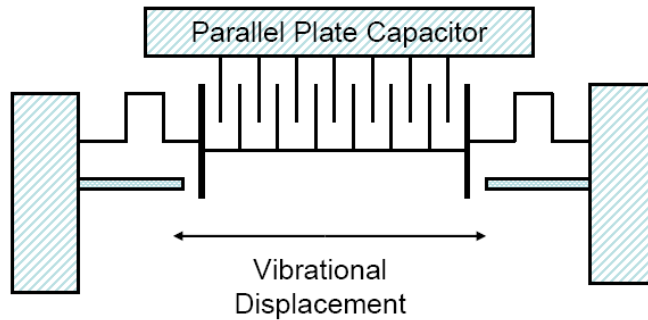


Figure 3. Variable Capacitor Schematic, Chiu, Kuo, and Chu (2007).

Meninger et al. (2001) used MEMS technology to fabricate an electrostatic energy harvester using a  $0.6 \mu\text{m}$  CMOS process. The system eventually produced  $5.6 \mu\text{W}$  with a power density of  $101.4 \mu\text{W} / \text{cm}^2$ . Tashiro et al. (2002) developed an electrostatic generator to power a cardiac pacemaker by harvesting left ventricular wall motion. The average power generation was  $36 \mu\text{W}$  and is enough for such an application. Roundy (2003B) built a capacitive MEMS electrostatic energy harvester with an optimized output power of  $42 \mu\text{W}$  for a 30 volt source. Miao et al. (2003) also fabricated and tested a micro electrostatic generator, which used a 26 V voltage source and output a high voltage of 2.3 kV and a power of  $24 \mu\text{W}$  at a vibration frequency of 10 Hz.

Mitcheson et al. (2004) proposed a new class of electrostatic generator – the Coulomb-force parametric generator (CFPG), which does not operate in a resonant manner like other vibration-to-electricity electromagnetic generators. It was demonstrated that the CFPG can better fit vibration sources with varying frequencies than resonant generators. In addition, it was concluded that a power density of a few  $\mu\text{W} / \text{cm}^3$  can be obtained from human body motion, but hundreds of  $\mu\text{W} / \text{cm}^3$  can be obtained from machine-powered applications.

Electrostatic energy harvesters can be fully integrated with MEMS and provide power for these low power consumption devices without the need of battery replacement. However, the primary disadvantage of electrostatic harvesters is the need for initial charges or voltages to get the conversion process started. Further, mechanical limit stops are needed to avoid reliability issue and to ensure that the capacitor electrodes do not come into contact and short the circuit.

### **Piezoelectric Devices**

Piezoelectric energy harvesters convert vibration energy to electrical energy through the piezoelectric effect, which was first demonstrated by the brothers Pierre and Jacques Curie at 1880. In brief, piezoelectric material undergoes a dipole deformation and charge formation when mechanical stress is applied to it. Conversely, mechanical stress is generated when a voltage is applied across a polarized piezoelectric material. Similar to ferroelectrics, piezoelectric material will lose polarity above Curie temperature. A new poling direction can be created by applying voltage across it at that moment, and it will be in the direction of the exerted electric field. More detailed descriptions can be found at Ikeda (1990).

In the initial development of piezoelectric materials, the piezoelectric effect was very small and was not useful for practical applications. With the introduction of LiTiBa ceramics, such as the first piezoelectric ceramic, Barium Titanate ( $\text{BaTiO}_3$ ), piezoelectric performance has been increased sufficiently for practical use in electromechanical devices. To date, a number of piezoelectric materials have been developed, including piezoelectric ceramics such as Lithium Niobate ( $\text{LiNbO}_3$ ), Lithium Tantalate ( $\text{LiTaO}_3$ ), Sodium Tungstate ( $\text{Na}_2\text{WO}_3$ ), and Lead Zirconate Titanate (PZT) ( $\text{Pb}(\text{Zr}, \text{Ti})\text{O}_3$ ), and piezoelectric polymers like Polyvinylidene Fluoride (PVDF). Using those materials, many commercially available piezoelectric transducers have been manufactured, such as those shown in Figure 4 (Priya, 2007). The devices shown in

that figure have different characteristics: the Thin Layer Unimorph Driver (THUNDER) is a prestressed sandwich structure (stainless steel-PZT-Aluminum) and can produce a large electric charge, but it is very brittle; active and micro fiber composites (AFC and MFC) have interdigital electrodes and uniaxially aligned glass fibers surrounded by polymer matrices, which can help overcome the rigidity and brittleness drawbacks of piezoelectric materials; a radial field diaphragm (RFD) is a thin circular piezoelectric ceramic disk sandwiched by two dielectric films and can work efficiently as an actuator. The QuickPack and piezoceramic bimorphs are the most common types of rigid PZT products and have been widely used as actuators and sensors in both on-resonance and off-resonance vibration applications. More detailed descriptions can be obtained in Priya (2007) and Sodano, Inman, and Park (2005).

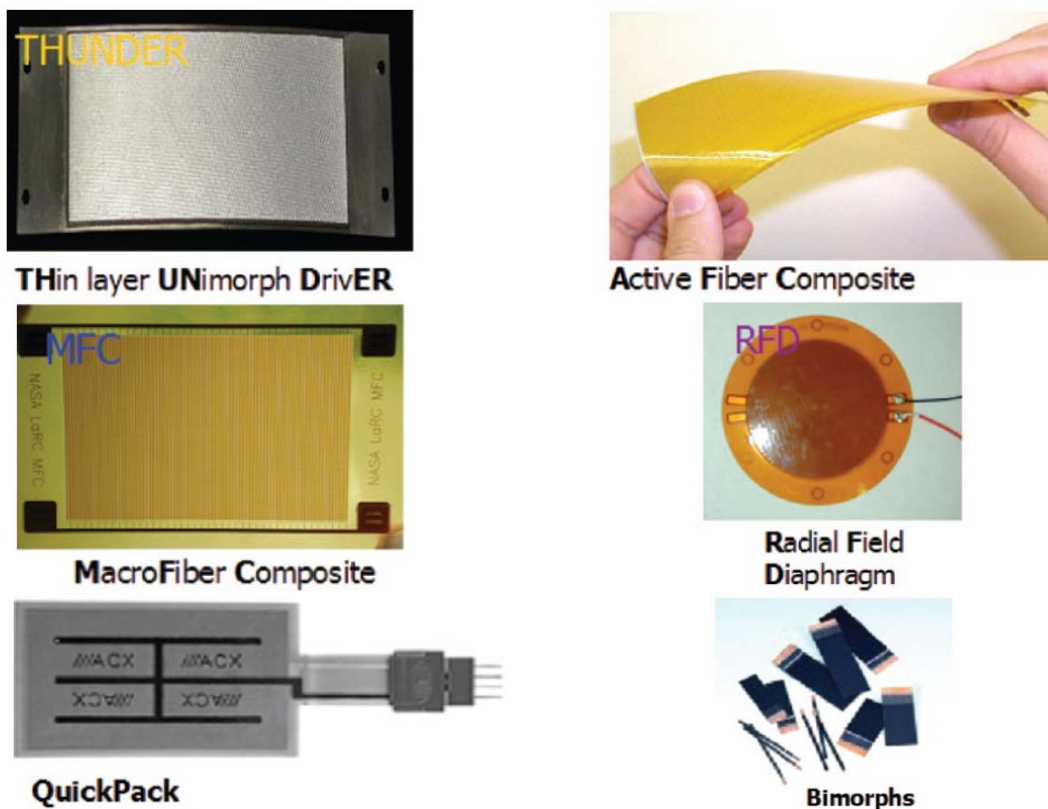


Figure 4. Piezoelectric Transducers, Priya (2007).

A number of researchers have studied the use of piezoelectric materials as energy

harvesters. Further, numerous experimental demonstrations have also been reported. Churchill et al. (2003) tested a piezoelectric element (PZT5A) consisting of unidirectionally aligned PZT fibers ( $250 \mu\text{m}$  diameter) embedded in a resin matrix. It was found that with dimensions of  $130 \text{ mm} \times 13 \text{ mm} \times 0.38 \text{ mm}$ , the device was able to generate  $0.75 \text{ mW}$  under a  $180 \text{ Hz}$  vibration. The power density was  $1167 \mu\text{W} / \text{cm}^3$ , which was sufficient to provide power for several wireless sensor nodes.

Roundy (2004) designed a piezoelectric bimorph (PZT5H) energy harvester with a total volume of  $1 \text{ cm}^3$ . That device provided a power output of  $375 \mu\text{W}$  under a vibration source of  $2.5 \text{ m} / \text{s}^2$  at  $120 \text{ Hz}$ , and it was used to power a custom-designed radio transmitter. Continuing his work, Roundy (2005) proposed an increasingly triangular trapezoidal profile, rather than a standard rectangular cantilever, so that the strain energy can be more efficiently distributed over the beam and thus can generate more electrical energy with the same volume of PZT material.

Ericka et al. (2005) investigated ways to improve the power harvested from ambient vibrations with a unimorph membrane transducer, which consisted of a circular PZT layer ( $25 \text{ mm}$  diameter and  $0.23 \text{ mm}$  thickness) bonded to a circular brass layer and was attached to the inner surface of a thick aluminum ring. A power of  $1.8 \text{ mW}$  was obtained for a resistive load of  $56 \text{ k}\Omega$  at its resonant frequency of  $2.58 \text{ KHz}$  and  $2 \text{ g}$  acceleration, with a power density of  $1455 \mu\text{W} / \text{cm}^3$ .

Choi et al. (2006) developed a MEMS-oriented PZT/SiNx cantilever structure with a proof mass added to the end. The device with dimension of  $170 \mu\text{m} \times 260 \mu\text{m}$  can generate  $1 \mu\text{W}$  of continuous power for a  $5.2 \text{ M}\Omega$  load with  $2.4 \text{ V}$  output at its first resonant frequency of  $13.97 \text{ KHz}$ , and the power density compares favorably to that of a lithium ion battery.

## Summary of Conversion Mechanisms

Three conversion mechanisms from vibration energy to electrical energy have been qualitatively and quantitatively discussed. Each mechanism can be used, under certain conditions, to generate a useful amount of electrical energy from ambient vibrations. The primary advantages and disadvantages of three types of converters, summarized from Roundy (2003 & 2004), are shown in Table 1. It appears that electromagnetic converters may be useful for large systems, or systems with large acceleration magnitudes, while piezoelectric converters exhibit most of the advantages of electromagnetic converters with no separate voltage needed to get the conversion started, which is necessary for electrostatic converters.

Table 1

Pros and Cons of Three Conversion Mechanisms, (2003A & 2004)

Mechanisms	Advantages	Disadvantages	Practical Energy Density ( $mJ/cm^3$ )	Theoretical Maximum Energy Density ( $mJ/cm^3$ )
Piezoelectric	<ol style="list-style-type: none"> <li>1. No separate voltage source.</li> <li>2. No mechanical stops.</li> <li>3. Highest Energy Density.</li> <li>4. Voltages: 2-10 V.</li> </ol>	<ol style="list-style-type: none"> <li>1. Not compatible with standard CMOS process.</li> <li>2. Piezo thin film: poor coupling.</li> </ol>	35.4	335
Electromagnetic	<ol style="list-style-type: none"> <li>1. No separate voltage source.</li> <li>2. No mechanical stops.</li> </ol>	<ol style="list-style-type: none"> <li>1. Maximum Voltage of 0.1 V.</li> <li>2. Difficult to integrate with electronics and MEMS.</li> </ol>	24.8	400
Electrostatic	<ol style="list-style-type: none"> <li>1. Easy to integrate with electronics and MEMS.</li> <li>2. Voltage 2-10 V</li> </ol>	<ol style="list-style-type: none"> <li>1. Separate voltage source needed.</li> <li>2. Mechanical stops needed.</li> </ol>	4	44

## Configuration and Modeling of PEH

The constitutive equations for a linear piezoelectric material are given in Equations 2.1 and 2.2 (ANSI / IEEE, 1988, 176-1987):

$$T = cS - dE , \quad (2.1)$$

$$D = dS + \varepsilon E , \quad (2.2)$$

where  $T$  is the mechanical stress (unit:  $N / m^2$ ),  $S$  is the mechanical strain (unit:  $m / m$ ),  $c$  is the elastic stiffness or Young's modulus (unit:  $N / m^2$ ),  $d$  is the piezoelectric strain coefficient (unit:  $m / V$ ),  $E$  is the electrical field (unit:  $V / m$ ),  $D$  is the electrical displacement or the charge density (unit:  $C / m^2$ ), and  $\varepsilon$  is the piezoelectric dielectric constant (unit:  $F / m$ ). The second term of  $dE$  in the right side of Equation 2.1 represents the piezoelectric coupling term, which provides the mechanism for energy conversion. As shown in Equations 2.1 and 2.2, the electric field across the material affects its mechanical behavior and vice versa.

The above piezoelectric constants are usually denoted as  $x_{ij}$ , where  $x$  represents the property variable, such as material elastic modulus  $c$  or strain coefficient  $d$ , and  $i$  and  $j$  represent the polarization and stress directions, respectively. The polarization direction is usually assigned 3, while other properties are assigned based on an orthogonal coordinate system, as shown in Figure 5. In this figure, the poling direction (in which the external voltage is exerted to polarize the piezoelectric material) is 3 and the strain direction is 1; as a result, the piezoelectric strain coefficient will be expressed as  $d_{31}$ . The three principle axes (Figure 5) are named 1, 2, and 3 respectively, while the shear effects around the principle axes are named 4, 5, and 6 respectively.

Due to the difference between the poling direction and the strain direction, piezoelectric

materials can be configured in many different ways that may prove useful in energy harvesting applications. This section will briefly review several common configurations of piezoelectric energy harvesters (PEH) that utilize the different poling and strain configurations, such as piezoelectric stack converters and piezoelectric bender converters. Further, some analytical modeling methods of PEH will be also discussed.

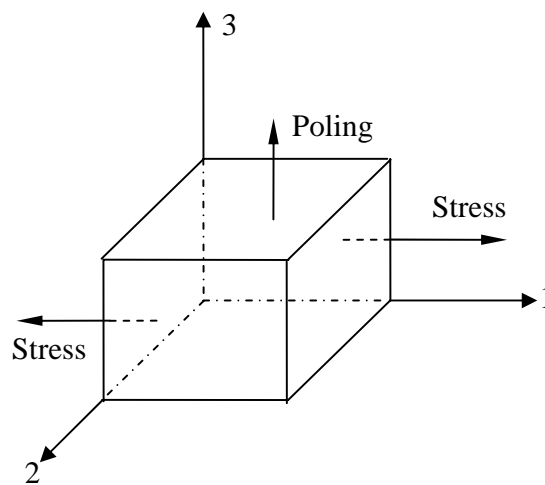


Figure 5. Orthogonal Coordinate System and Poling-Stress Direction.

### Piezoelectric Stack Converter

A piezoelectric stack converter consists of a large number of piezoelectric thin plates bonded together and wired in parallel, as shown in Figure 6. The stacking is used to increase the overall power output of the converter. It can be seen that the device operates in the 33 mode, since the applied force is in the same direction as its poling direction, and the latter is always assigned the number '3'. Although the piezoelectric strain coefficient  $d_{33}$  under this configuration is usually two-time larger than  $d_{31}$ , under bender configuration, the electrical energy could only be generated when either tensile or compressive loads are applied to the device. If there are only lateral forces available, it is necessary to convert it to longitudinal force.

In addition, since a small-sized piezoelectric stack converter is very hard to fabricate, the volume of such an energy harvester will be relatively large, limiting its application in portable electronics or MEMS.

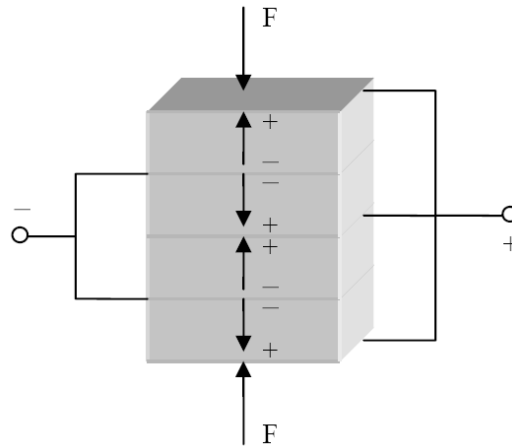


Figure 6. Piezoelectric Stack Energy Harvester.

### **Piezoelectric Bender Converter**

A piezoelectric bender converter is typically a cantilevered multi-layer beam structure, with one or more layers bonded to an elastic metal layer in order to increase the overall elasticity of the structure and overcome the brittleness of piezoelectric materials. Usually, one cantilevered beam with one piezoelectric layer bonded to a metal layer (such as brass or aluminum) is called unimorph, while a beam composed of a metal layer sandwiched by two piezoelectric layers is considered a bimorph. Two different types of bimorphs are shown in Figures 7 and 8. A piezoelectric bender converter can be constructed to have one of two different operating modes, depending on the configuration of the piezoelectric electrodes. For the bimorph shown in Figure 7, the electrodes cover the overall top and bottom surfaces of the cantilever bender, and the poling direction is perpendicular to the stress direction, so the 31 mode is used. The bimorph shown in Figure 8 has interdigitated electrodes distributed sparsely on the top and bottom surfaces

of the bender, while the poling direction and the stress direction are both in the longitudinal direction. As such, the 33 mode exists everywhere except directly below the electrodes.

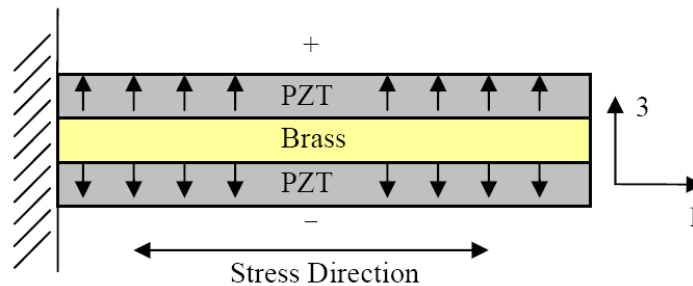


Figure 7. 31-Type Piezoelectric Bender Converter.

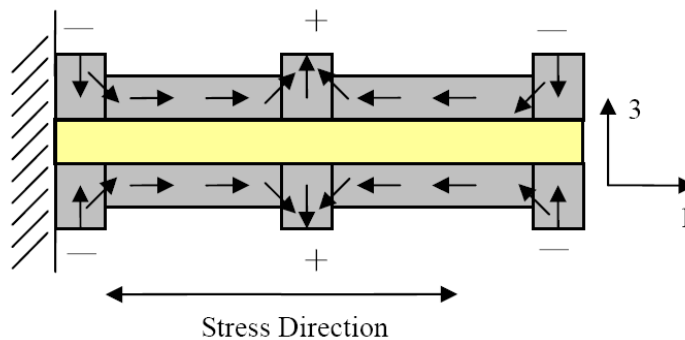


Figure 8. 33-Type Piezoelectric Bender Converter.

For a bimorph in operation, the top and bottom PZT layers are always experiencing opposite states of stress; one is in tension while the other is in compression. Therefore, if the two PZT layers are poled in the same direction and the electrodes are wired appropriately, the generated current will double, which is called parallel poling. Conversely, if the two piezoelectric layers are poled in the opposite direction, the produced voltage will double, which is called series poling. Theoretically, there is no difference in the power conversion under these two operating polings.

The 31-mode piezoelectric bimorph (as shown in Figure 7) may be the simplest and most widely-used configuration for energy harvesting. The piezoelectric material is concentrated in

regions of large strain, and the strain across the cross-section is relatively constant. Further, the construction is considerably simpler than that of the 33-mode device shown in Figure 8. A very important characteristic of the bimorph configuration is the potential for bonding additional mass at the end of the beam, such that the resonant frequency of the structure can be adjusted. This may be quite useful, as it is very important to match the resonant frequency of the designed generator with the frequency of ambient vibration, in order to produce the largest strain energy and thus obtain the largest electrical energy.

### **Analytical Models for Piezoelectric Energy Harvester**

The concept of piezoelectric materials for energy harvesting has been explored by many researchers over the past few decades. Numerous studies have demonstrated their feasibility in the field of energy harvesting. Along with experimental demonstrations, many researchers have developed analytical models to predict and optimize the amount of electrical energy that could be harvested.

Smits and Choi (1991A) derived constitutive equations for a piezoelectric bender (unimorph), consisting of a piezoelectric layer and a non-piezoelectric layer, and described the electromechanical behavior of a cantilever bender subjected to various boundary conditions, including a mechanical moment  $M$  at the end of the bender, a perpendicular force  $F$  at the end of the bender, and a uniformly distributed body force  $p$  on the entire length of the bender. The constitutive equations were derived by calculating the internal energy of the bender for thermodynamic equilibrium. With a similar derivation, Smits, Dalke, and Cooney (1991B) also derived the constitutive equations for a piezoelectric bender with two PZT layers bonded together. Following his work, Wang et al. (1999) derived the constitution equations for a piezoelectric bender (bimorph) with an elastic layer sandwiched by two PZT layers. The

dependence of the produced voltage and charge on the geometric and material properties of the piezoelectric bender was also discussed. It should be noted that there is a difference in the nomenclature between this study and Wang's research. To avoid confusion, the piezoelectric bender with one PZT layer bonded onto one metal layer will be called unimorph, while the one with a central metal layer sandwiched by two piezoelectric layers will be named bimorph, as are consistent with their commercial names.

Wang (2001) developed three analytical models, including a pin-force model, an enhanced pin-force model, and an Euler-Bernoulli model, to predict the electrical potential of a piezoelectric cantilever unimorph subjected to a bending moment or a force. The pin-force model did not take the bending stiffness of the piezoelectric layer into consideration, where the strain in the elastic layer was still assumed to follow Euler beam theory, while the strain through the piezoelectric thickness was assumed as constant. Therefore, the model is limited when the thickness of the elastic layer is much larger than that of the piezoelectric layer. The enhanced pin-force model considered the PZT bending stiffness, while the assumptions of PZT bending on its own axis and PZT connecting with the substrate layer only by the end pins still caused a drawback. The Euler-Bernoulli model was the most accurate model which assumed that the PZT layer and the elastic layer bend about a common neutral axis, as can be calculated by a modulus-weighted algorithm. Eggborn (2003) later used those three models to perform parametric studies to determine the optimal bonding locations along the substrate beam, the optimal dimensions of a PZT bender, and the input force function for the generator.

Kim (2002) developed piezoelectric constitutive equations for unimorph and bimorph generators with various poling configurations. Energy generation was analyzed by varying the thickness ratios and poling directions at various locations. In addition, the experimental

demonstration indicated the existence of an optimal electrode pattern, which leads to maximum electrical energy conversion in a given volume of piezoelectric material under an applied force, pressure, or stress.

Roundy (2003B, 2004) developed an electrical equivalent circuit model for a PZT bimorph generator, which had a proof mass on the free end and was subjected to an ambient vibration. It was shown that the maximum power output would occur where the resonant frequency of the generator matches the frequency of ambient vibrations. In addition, the model was validated and used as the basis for design optimization of a piezoelectric vibration-based generator for wireless electronics.

Richards et al. (2004) developed a formula for predicting the power conversion efficiency for a piezoelectric membrane generator. The trade-off effect on efficiency caused by the quality factor and the electromechanical coupling factor of the device was quantitatively demonstrated. It was shown that three effective ways, in decreasing order, to increase electrical energy conversion are decreasing the structural stiffness, decreasing the mechanical damping, and increasing the effective proof mass.

Sodano, Inman, and Park (2004) developed a model to estimate the potential power that could be generated using a vibrating cantilever beam with bonded PZT elements. The system equations of motion were derived using energy conservation and Hamilton's principle. The accuracy and robustness of the model were experimentally verified using a non-homogenous piezoelectric cantilever device (QuickPack QP40N).

There are also plenty of finite element models for piezoelectric structures developed by researchers over the years. Allik and Hughes (1970) presented a finite element formulation for the material possessing piezoelectric or electroelastic effect. It was demonstrated that the

dynamic matrix equation of piezoelectrics can be reduced to well-known equations of structural dynamics. Further, a tetrahedral finite element was presented and applied to 3D piezoelectric problems. Lerch (1990) developed 2D and 3D finite elements for piezoelectric devices with no restrictions other than linearity. The finite element method allowed the handling of anisotropic material tensors and almost any geometry for static, eigenfrequency, harmonic, and transient analysis. Benjeddou, Trindade, and Ohayon (1999) developed a new adaptive sandwich beam finite element capable of handling either extension or shear actuation mechanisms. The finite element had two nodes and only four mechanical degrees of freedom. It was demonstrated that the shear actuation mechanism is better than the extension mechanism for structures with high stiffness and the piezoelectric actuators with high thicknesses.

In addition, finite element (FE) modeling and analysis of piezoelectrics can also be directly carried out by using commercially available FE software such as ANSYS®, ABAQUS® and MSC/NASTRAN®. Wu et al. (2005) used a finite element simulation with ANSYS to validate the dynamic performance of piezoelectric bimorph cantilevers. The bonding effects between layers were also analyzed with both static and dynamic methods. Dong, Meng, and Peng (2006) and Malgaca and Karagulle (2009) employed piezoelectric analysis with ANSYS® to simulate active vibration control of smart beams subjected to vibrations. Their simulations and experimental results were in agreement.

In this effort, a PCB energy harvester is chosen as the research object, due to its high adaptability to match its structural resonant frequency with the frequency of ambient vibration. The objectives are: to thoroughly study the geometric effects of a PCB generator on its resonant frequency and power output; and to present design optimizations based on those theoretical analyses. As a result, an analytical frequency prediction model and a power output model for the

PCB energy harvester with a proof mass on the free end will be developed in the next two chapters. The models will be validated using FEA and experiments. Further, design optimization based on the aforementioned models will be discussed, including the optimization of a single PCB energy harvester and the design of a band-pass energy harvester with an ensemble of several PCB energy harvesters, due to the frequency band characteristics of certain ambient vibrations. Finally, some future studies on piezoelectric energy harvesting will be proposed.

### **Summary**

In the chapter, the ambient energy sources that could be harvested into electrical energy were discussed, including solar, wind, water flow, temperature gradient, mechanical vibration, and acoustic waves. Due to the ubiquitous presence of mechanical vibration in the industrialized environment, it is adopted as the ambient energy source of focus in this study. Three vibration energy conversion mechanisms were discussed, including electromagnetic, electrostatic, and piezoelectric. Due to its high power density, light weight, and MEMS-integration ability, a piezoelectric device was chosen as the object of study. Two typical piezoelectric generators, i.e. piezoelectric stack device and piezoelectric bender, were discussed, and two different operation modes of the piezoelectric generator, i.e. 33 mode and 31 mode, were also presented. Due to its ability to adapt the resonant frequency of the device with the frequency of ambient vibration through bonding a proof mass at the free end, piezoelectric cantilever bimorph is chosen as the object of study and optimization. Further, the analytical and finite element modeling techniques for piezoelectric bender generators were briefly reviewed.

In an effort to thoroughly understand the performance of a PCB energy harvester, the first goal of this research is to study the effect of the device geometry on its resonant frequency, since

matching the PCB resonant frequency with the frequency of ambient vibration leads to maximum power harvesting. Specifically, an analytical frequency model using Euler-Bernoulli beam theory, Lagrange's equation of motion, and Rayleigh-Ritz method will be presented in the next chapter.

## CHAPTER 3

### ANALYTICAL MODELING OF RESONANT FREQUENCY OF PCB GENERATOR

Due to the strain-dependent charge output characteristics of piezoelectric materials, it is very important to match the resonant frequency of the piezoelectric cantilever bimorph (PCB) energy harvester to the frequency of ambient vibration, since strain energy maximizes where structural resonance occurs. In this chapter, based on the work in Zhang and Williams (2009), an analytical model for determination of the resonant frequency of the PCB with a proof mass on the free end is presented, followed by a study of the effect of PCB geometry on the resonant frequency. Further, the analytical model is validated through finite element analysis (FEA) and laboratory experiments. It is shown that the analytical model is competent in predicting the resonant frequency of the PCB generator.

#### **Modeling of Resonant Frequency of PCB Generator**

In this section, the geometric configuration and operating mode of a PCB generator is first described. A PCB model from the literature is then presented which provides for estimation of the resonant frequency of a PCB with a proof mass on the free end. Then, the development of a new analytical frequency model is presented. The new model is developed using Euler-beam theory, Lagrange's equations of motion, and the Rayleigh-Ritz method.

#### **PCB Generator Configuration**

A typical PCB generator consists of a piezoelectric bimorph and a proof mass on the free

end of the bimorph, and the whole device is left-clamped onto a vibrating base, such as an operating machine, a running transportation tool, or a vibrating structure. A sketch of a PCB generator is shown in Figure 9, where the input to the system is the acceleration of the left-clamped end  $\ddot{y}$ .

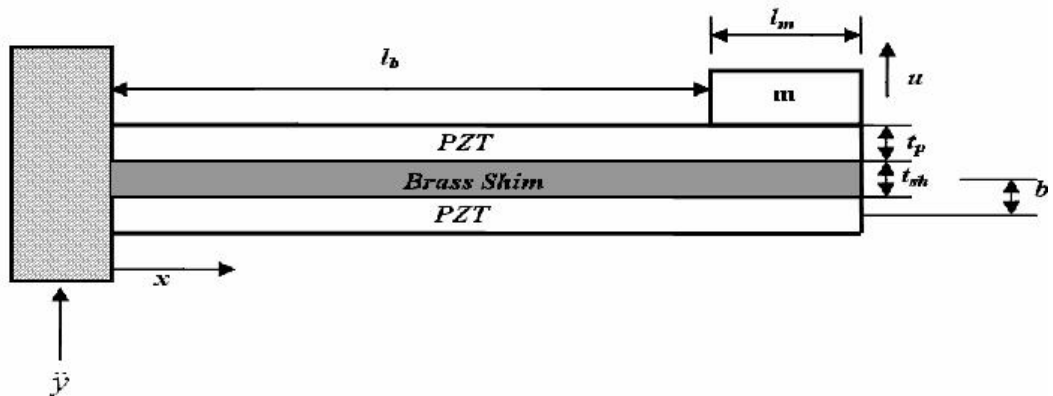
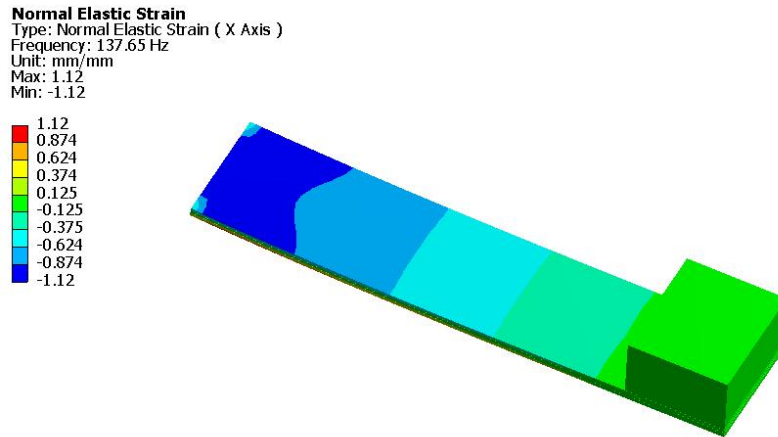


Figure 9. A Schematic Diagram of a PCB Generator.

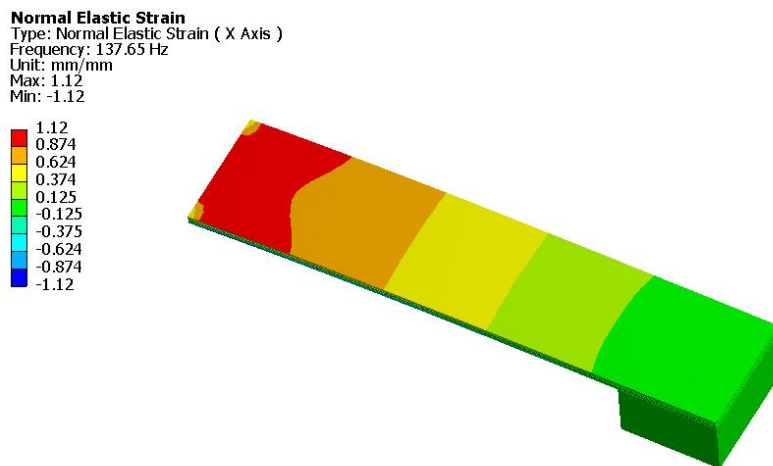
Although the electrical-mechanical coupling coefficient for the 31 mode is lower than for the 33-mode, the piezoelectric device working under 31-mode is much more compliant, since a smaller input force can produce much larger strain throughout the device, compared with the device working under 33-mode. Therefore, it is common for a piezoelectric device operating under 33 mode to have a large number of piezoelectric plates stacked together to obtain enough electrical energy, which is not preferable for the light-weight requirements of portable electronics and wireless sensor nodes.

The PCB generator is the most common type of 31-mode device. In this operating mode, a large strain will be generated in the 1(x) direction when the device poled in the 3(y) direction is subjected to a bending load. As the bimorph bends up, the top PZT layer is in compression, while the bottom PZT layer is in tension, as is shown in Figure 10, where the elastic strain distribution of the bimorph along the x axis indicates that the top and bottom PZT layers are in different

strain conditions, while they have identical absolute values of strain.



(a) Compression Mode for Top PZT Layer



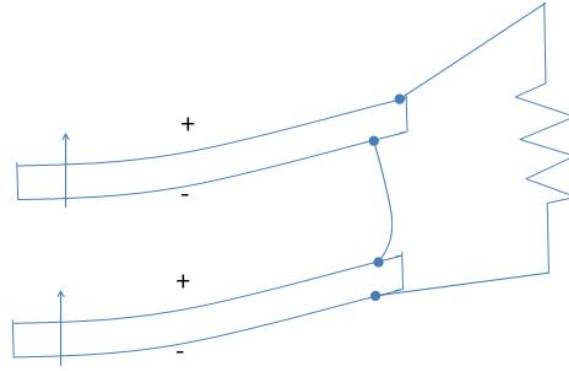
(b) Tension Mode for Bottom PZT Layer

Figure 10. Compression Mode and Tension Mode of PZT Layer.

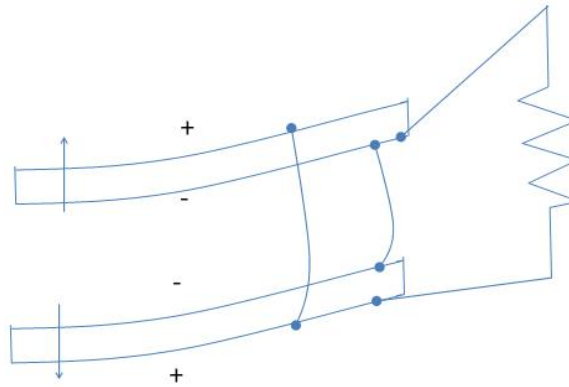
Therefore, if the top and bottom PZT layers are poled along the same axis and electrodes are wired appropriately, the electrical potential generated the combination will be twice that of the individual layers. This approach is termed series poling, as is shown in Figure 11a.

Conversely, if they are poled in the opposite direction, which is known as parallel poling, The

generated current will double, as is shown in Figure 11b. In either case, the converted electrical energy would be identical due to the identical strain energy produced throughout the top and bottom PZT layers, while only the voltage-to-current ratio will be affected.



(a) Series Poling



(b) Parallel Poling

Figure 11. Series Poling and Parallel Poling.

Roundy (2004) developed an equivalent electrical circuit model for the PCB energy harvester with a proof mass on the free end. The power output was obtained as follows:

$$P_R = \frac{1}{2R} * \frac{RC_b (2k_{31}t_{sh} / k_2)^2 c_p / \varepsilon}{\left[ \frac{\omega_n^2}{\omega RC_b} - \omega \left( \frac{1}{RC_b} + 2\zeta\omega_n \right) \right]^2 + \left[ \omega_n^2 (1 + k_{31}^2) + \frac{2\zeta\omega_n}{RC_b} - \omega^2 \right]} A_{in}^2 \quad (3.1)$$

$$k_1 = \frac{L(t_{sh} + t_p)}{4I} \quad (3.2)$$

$$k_2 = \frac{(L - L_m)^2 (4L - L_m)}{3L(t_{sh} + t_p)} \quad (3.3)$$

$$I = \frac{w_p t_p^3}{6} + 2wt_p b^2 + \frac{c_{sh} w_p t_{sh}^3}{12c_p} \quad (3.4)$$

$$b = \frac{1}{2}(t_p + t_{sh}) \quad (3.5)$$

where  $\omega$  is the driving frequency, i.e. the frequency of ambient vibration;  $\omega_n$  is the resonant frequency of the PCB generator;  $R$  is the resistive load;  $C_b$  is the PCB capacitance;  $\varepsilon$  is the PCB dielectric constant;  $\zeta$  is the damping ratio of the device;  $k_{31}$  is the piezoelectric coupling coefficient;  $C_p$  and  $C_{sh}$  are the Young's modulus of the PZT layer and the center brass layer, respectively;  $A_m$  is the amplitude of input acceleration;  $L$ ,  $w_p$ , and  $t_p$  are the length, width, and thickness of a single PZT layer;  $t_{sh}$  is the thickness of the center brass shim; and  $l_m$  is the length of the proof mass. These geometric parameters are also indicated in Figure 9. For convenience and consistency, the above notations will also be used in the following chapters.

Using Equation 3.1, it can be shown that the power output of the PCB generator is maximized when the resonant frequency  $\omega_n$  of the PCB generator matches the driving frequency  $\omega$ . Therefore, the resonant frequency is one of the key factors in the PCB energy harvester, and it is important to understand the relationship between PCB geometry and the corresponding  $\omega_n$ .

### **A Previous Model for PCB Resonant Frequency**

An analytical model of the resonant frequency of a cantilevered piezoelectric bimorph was developed by Wang et al. (1999). That model was then modified by Shen et al. (2006), who extended the model to the more complex configuration of a PCB with a proof mass on the free

end. The fundamental resonant frequency of that PCB generator can be expressed using Equations 3.6-3.9:

$$\omega_n = 0.560 \sqrt{\frac{0.236w_p E_0 (L - l_m / 2)^3}{0.236Mw_p L^7 + ml^3 (L - l_m / 2)^3}} \quad (3.6)$$

$$E_0 = \frac{2c_p t_p^3}{3} + c_p t_{sh} t_p^2 + \frac{c_p t_{sh}^2 t_p}{2} + \frac{t_{sh}^3 c_{sh}}{12} \quad (3.7)$$

$$M = 2\rho_p t_p + \rho_{sh} t_{sh} \quad (3.8)$$

$$m = \rho_m l_m w_m h_m \quad (3.9)$$

where  $\rho_p$  and  $\rho_{sh}$  are the density of the PZT material and the central shim layer, respectively, and  $w_m$ ,  $h_m$ , and  $\rho_m$  are the width, height, and density of the proof mass, respectively. The other parameters are identical to those described in the power output model derived by Roundy (2004) and represented by Equations 3.1-3.5.

### A New Frequency Model for PCB Generator

In this section, the development of an analytical model for the resonant frequency of the PCB with a proof mass on the free end (Figure 9) is presented in detail. Prior to introducing the derivation, the following assumptions are made:

- (1) The transverse displacements of all three layers of the PCB are equal.
- (2) There is no slip between the PCB layers.

With the above assumptions, the kinetic energy and potential energy of the PCB generator can be obtained in terms of the first-order time derivative and the second-order displacement derivative, respectively, as are shown in Equation 3.10 and 3.11:

$$T = \frac{1}{2} \sum_{i=1}^3 \int_0^L \rho_i A_i \left( \frac{\partial u}{\partial t} \right)^2 dx + \frac{1}{2} \int_{L-l_m}^L \rho_m A_m \left( \frac{\partial u}{\partial t} \right)^2 dx \quad (3.10)$$

$$V = \frac{1}{2} \sum_{i=1}^3 \int_0^L E_i I_i \left( \frac{\partial^2 u}{\partial x^2} \right)^2 dx + \frac{1}{2} \int_{L-l_m}^L E_m I_m \left( \frac{\partial^2 u}{\partial x^2} \right)^2 dx \quad (3.11)$$

where  $u(x, t)$  is the transverse displacement;  $\rho_i$ ,  $A_i$ ,  $E_i$ , and  $I_i$  are the density, cross-sectional area, Young's modulus, and the moment of inertia of the  $i^{\text{th}}$  layer of the bimorph, respectively; and  $\rho_m$ ,  $A_m$ ,  $E_m$ , and  $I_m$  are the density, cross-sectional area, Young's modulus, and the moment of inertia of the proof mass, respectively.

Using the Rayleigh-Ritz method, the transverse displacement of PCB can be expressed as the summation of transverse modes in the bimorph beam:

$$u(x, t) = \sum_{k=1}^n u_k(t) \psi_k(x) \quad (3.12)$$

where  $u_k(t)$  is the temporary coordinate of the transverse displacement and  $\psi_k(x)$  is the mode shape of the structure, which can be chosen appropriately to satisfy the different boundary conditions.  $k$  is the order of the mode shape function,  $n$  is the number of modes to be expanded in the analysis, and  $x$  is the location along the bimorph, with the origin at the clamped end. For a PCB generator with clamped-free boundary conditions, the mode shape can be obtained from Rao (2003) as follows:

$$\psi_k(x) = \sin \beta_k x - \sinh \beta_k x - \frac{\sin \beta_k L + \sinh \beta_k L}{\cos \beta_k L + \cosh \beta_k L} (\cos \beta_k x - \cosh \beta_k x) \quad (3.13)$$

Substituting the displacement series of Equation 3.12 into Equation 3.10 and 3.11, Lagrange's method can then be employed to derive the equation for the motion of the PCB generator. The resulting equations are found as:

$$(K - \omega^2 * M)U = 0 \quad (3.14)$$

where  $[K]$  is the truncated  $n \times n$  stiffness matrix of the structure and  $[M]$  is the truncated  $n \times n$

mass matrix of the structure, which can be conveniently used to solve for the resonant frequency of PCB.

### A Simplified Model for PCB Tip displacement

The tip displacement is also an important dynamic parameter in strain-dependent PCB energy harvesting, because it can reflect the strain condition in the piezoelectric bimorph, i.e. the larger the tip displacement, the higher strain distribution along the bimorph. The tip displacement of the PCB with a proof mass on the free end can be simplified and modeled as a single degree of freedom (SDOF) system, according to Ng and Liao (2005), where an equivalent spring-damper-mass system is subjected to a base excitation, as is shown in Figure 12, where  $M$  is the effective mass of the generator,  $K$  is stiffness of the bimorph,  $C$  is the damping coefficient of the device,  $\ddot{y}$  is the input vibration acceleration, and  $\ddot{z}$  is the induced acceleration of the effective mass. The simplified model for the tip displacement of the PCB generator is derived next.

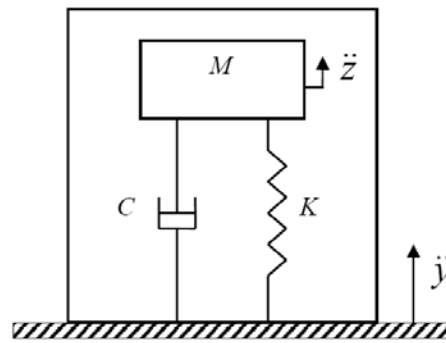


Figure 12. An SDOF Model of PCB Generator, Ng & Liao (2005).

Using Newton's second law, the equation of the damped seismic motion of the PCB generator can be obtained as:

$$M\ddot{z} + C\dot{z} + Kz = Ky + C\dot{y} \quad (3.15)$$

For sinusoidal base vibration, assuming  $\ddot{y} = A_m \sin(\omega t)$ , the tip response is

$z(t) = a \cos(\omega t) + b \sin(\omega t)$ . According to Tongue (2002), the transfer function of the system can be obtained with the initial conditions of  $z(0) = \dot{z}(0) = 0$ :

$$\left| \frac{\bar{z}}{A_{in}} \right| = \frac{1}{\omega^2} \sqrt{\frac{\omega_n^4 + (2\zeta\omega\omega_n)^2}{(\omega^2 - \omega_n^2)^2 + (2\zeta\omega\omega_n)^2}} \quad (3.16)$$

where  $\omega$  is the driving frequency of the ambient vibration,  $\omega_n$  is the resonant frequency of the PCB generator, and  $\zeta$  is the damping ratio of the device. If the resonant frequency of the device matches the driving frequency of the ambient vibration, the tip displacement of the generator can be obtained as follows:

$$|\bar{z}| = \frac{A_{in}}{\omega_n^2} \sqrt{1 + \frac{1}{4\zeta^2}} \quad (3.17)$$

The damping ratio  $\zeta$  can be obtained through experimental measurements, such as the successive-peak-ratio method, using a shock response, or the half-power method, using the harmonic response of the PCB generator, while  $\omega_n$  can be directly calculated by its definition of  $\omega_n = \sqrt{K/M}$ . According to Wang and Cross (1999), the stiffness  $K$  of the piezoelectric bimorph can be calculated as:

$$K = \frac{Dw}{4L^3} c_{sh} c_p \quad (3.18)$$

where  $D = \frac{2(3t_{sh}^2 t_p + 6t_{sh} t_p^2 + 4t_p^3)}{c_{sh}} + \frac{t_{sh}^3}{c_p}$  and where the parameter definitions are identical to

those in the aforementioned power output model of Roundy (2004). Ng and Liao (2005) state that the effective mass  $M$  can be calculated based on the experimental work:

$$M = \frac{33}{140} M_{bimorph} + M_{proofmass} \quad (3.19)$$

where  $M_{bimorph}$  and  $M_{proofmass}$  are the masses of the piezoelectric bimorph and the proof mass.

## Geometric Effect on the Resonant Frequency

Due to the importance of the resonant frequency of the PCB generator in vibration energy harvesting, an examination of the effect of PCB generator geometry on the corresponding resonant frequency will be carried out in this section. In addition, the new analytical model for the resonant frequency of the PCB generator is compared to the model of Shen et al. (2006) and a finite element analysis (FEA).

A piezoelectric bimorph PZT Q220-A4-203Y, purchased from Piezo Systems Inc., is used as the research object in this study. The shape and dimensions of the bimorph are shown in Figure 13, and the effective dimension and the key properties are shown in Tables 2 and 3.

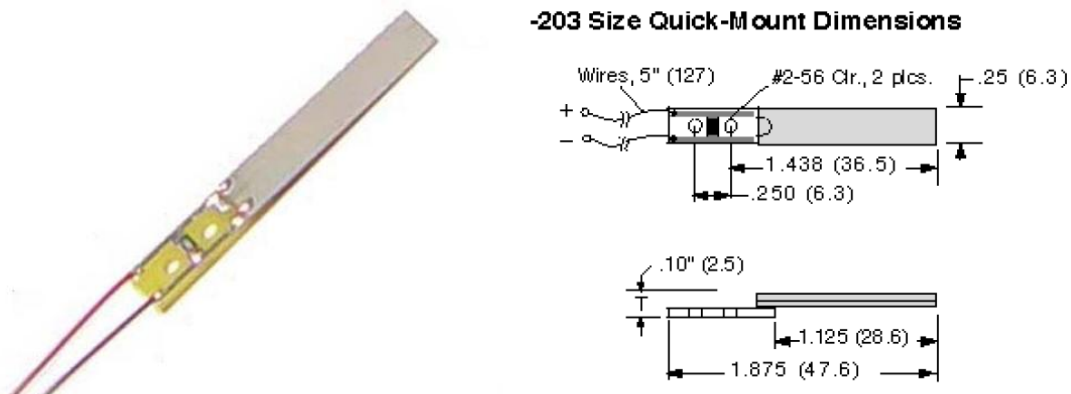


Figure 13. Shape and Dimension of Q220-A4-203Y, Piezo System

Table 2

Specific Dimension of Q220-A4-203Y

$L$ (mm)	$w_p$ (mm)	$t_p$ (mm)	$t_{sh}$ (mm)
28.43	6.35	0.191	0.127

Table 3

PZT Properties of Q220-A4-203Y, Piezo System

Property	Units	Value
Density $\rho$	$\times Kg / m^3$	7800
Strain Coefficient $d_{31}$	$\times 10^{-12} m / V$	-190
Coupling Coefficient $k_{31}$	$CV / Nm$	0.35
Relative Dielectric Constant $\epsilon$	/	1800
Dielectric Constant $\epsilon_0$	$\times 10^{-8}$	3.36
Young's Modulus	$GPa$	66
Coefficient of Thermal Expansion	$\times 10^{-6} C^{-1}$	-4.0

The two PZT layers of the bimorph are poled in opposite directions and wired for parallel operation. The central layer of the bimorph and the proof mass are made of brass, with an assumed density of  $8800 kg / m^3$ , Young's modulus of  $110 GPa$ , and Poisson's ratio of 0.35. Proof mass is bonded to the free end of the bimorph by adding successive brass shims. Each shim has a length of 4.00 mm, a width of 6.35 mm and a thickness of 1.60 mm. During the case study, the brass shims were added to the free end of the PCB one by one to vary the mass of the proof mass.

It is well-known that every structure has unlimited modes, i.e. resonant frequencies; therefore, prior to studying the geometric effect of the bimorph and the proof mass on the resonant frequency of the device, a modal analysis of the PCB generator was performed using ANSYS® 10.0. The results of the analysis are shown in Figure 14, where the first 6 modes (first 3 bending modes and first 3 torsion modes) of the device are presented.

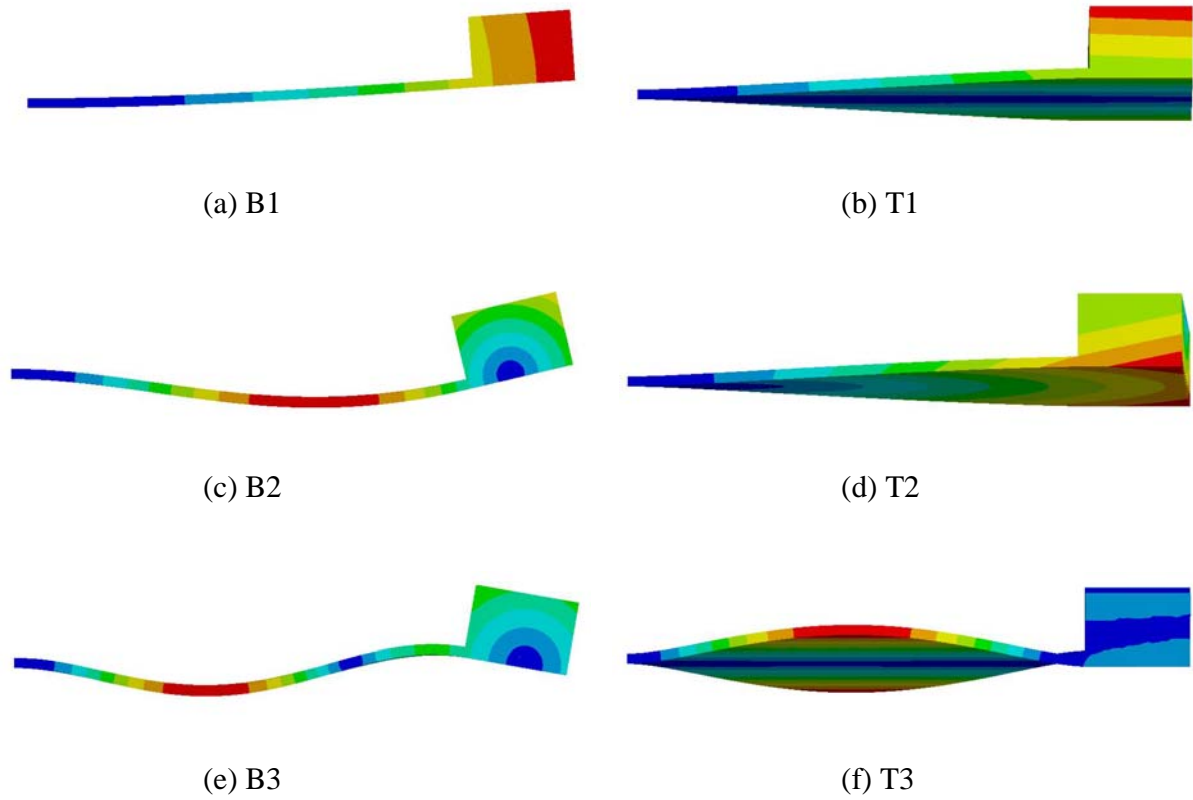


Figure 14. First 6 Modes of PCB Generator

It can be seen that each mode corresponds to a certain deformation of the structure, and thus will generate certain electrical energy. However, according to the power output model developed by Roundy (2004), shown in the Equation 3.1, where if the resonant frequency of the device matches the frequency of the ambient vibration, the power output can be derived as follows:

$$P_R = \frac{1}{\omega_n^2} * \frac{2R(C_b k_{31} t_{sh} / k_2)^2 c_p / \varepsilon}{(4RC_b \zeta^2 \omega_n^2 + RC_b k_{31}^2 + 2\zeta)} A_{in}^2, \quad (3.20)$$

It is clear that the power output is inversely proportional to the square value of the resonant frequency, i.e. the lower resonant frequency, the larger amount of generated power. Therefore, the fundamental resonant frequency (the 1<sup>st</sup> bending frequency) will be the main research object in this study.

## Geometric Effect of the Bimorph

In this section, the effect of the bimorph dimensions on the resonant frequency of the device is studied. The dimensions of particular interest are the length and thickness of the PCB. While studying the effect of one single parameter, the other parameters are kept stable. First, the length of the bimorph is increased gradually while other parameters of the bimorph are fixed and the dimensions of the proof mass are kept at  $4\text{mm} \times 6.3\text{mm} \times 6\text{mm}$  (a collection of four shims attached to the end of the PCB). The variation of the PCB resonant frequency with PCB length is shown in Figure 15, where the new analytical frequency model is simply called the Euler model. As would be expected, the resonant frequency of the generator decreases with increasing PCB length. In addition, the results of the new analytical model (termed the Euler model in the figure) are closer to the finite element analysis than those of the model presented by Shen et al. (2006).

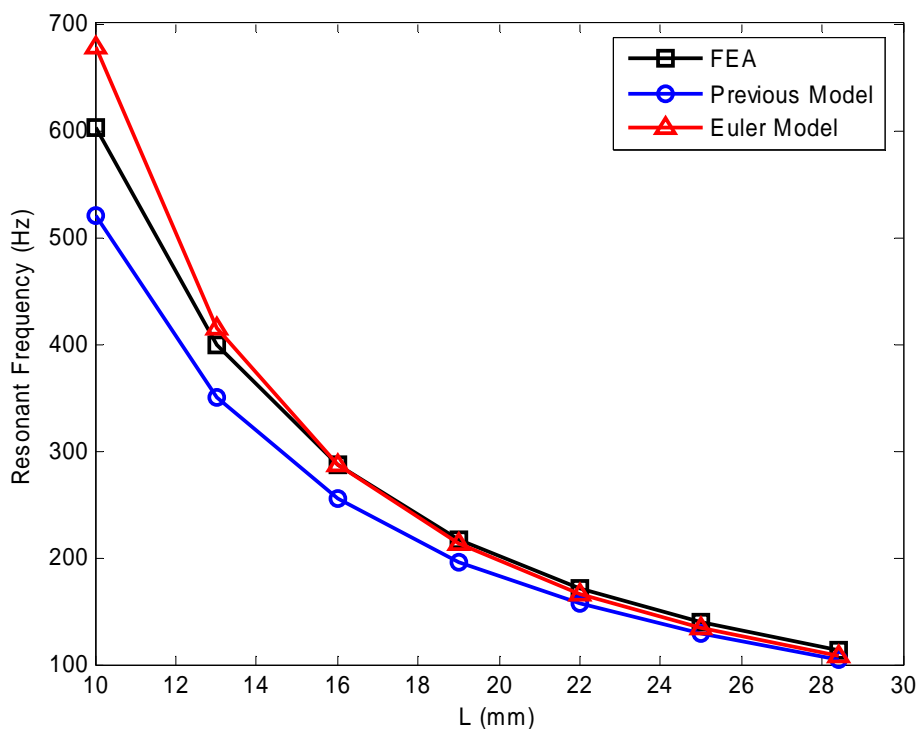


Figure 15. Length Effect of the Bimorph on the Resonant Frequency.

Next, the effect of varying PCB thickness was examined. The results are shown in Figure 16, where the new analytical frequency model is simply called the Euler model. As would be expected, it is clear that the resonant frequency increases with the thickness increase of the bimorph. In addition, both the new analytical model and Shen et al.'s (2006) model are relatively close to the finite element analysis. The results of the studies demonstrate that variation of the PCB length and thickness could be used to design a PCB with a targeted resonant frequency. In practice, however, it may not be practical to increase the thickness of a PCB, as only certain discrete thicknesses may be available from a given manufacturer. While shortening a PCB is possible through the use of an appropriate cutting tool, adding to its length is not an option. As such, modifying the amount of proof mass is really a more practical method for tuning the PCB resonant frequency. Therefore, the effect of the added proof mass will be studied next.

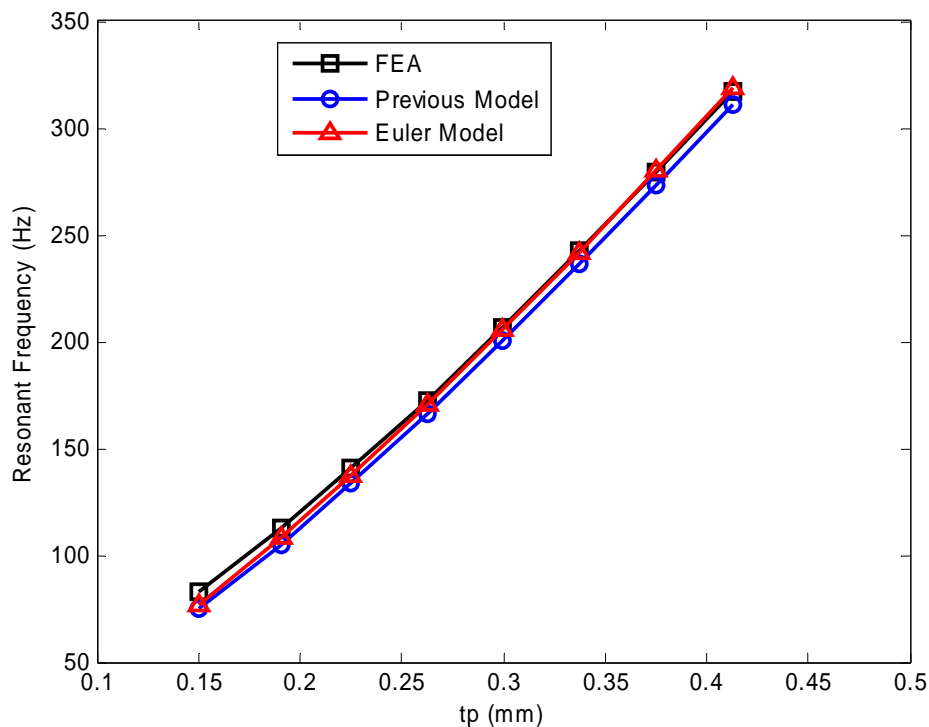


Figure 16. Thickness Effect of the Bimorph on the Resonant Frequency.

## Geometric Effect of the Proof Mass

As a PCB vibrates, tensile stress and compressive stresses will be induced in the PZT layers of the bimorph. Adding a proof mass to the end of the bimorph will increase the stress/strain generation and thus generate more electrical energy, while the effect of the proof mass on the resonant frequency of the piezoelectric device also merits study.

First, the weight effect of the proof mass on the resonant frequency is examined. The geometric dimension of the proof mass is kept stable at  $4\text{mm} \times 6.3\text{mm} \times 6\text{mm}$ , while 6 different materials are selected as the proof mass material, including aluminum, titanium, steel, brass, lead, and tungsten, respectively, with their material properties obtained from MatWeb.com and listed in Table 4.

Table 4

Material Properties of the Proof Mass, MatWeb.com

Material	Density ( $Kg / m^3$ )	Young's Modulus ( $GPa$ )	Poisson Ratio
Aluminum	2700	68	0.36
Titanium	4500	116	0.34
Steel	7800	200	0.30
Brass	8800	110	0.35
Lead	11340	14	0.42
Tungsten	19350	400	0.28

The weight effect result of the proof mass on the resonant frequency is shown in Figure 17, where the new analytical frequency model is simply called the Euler model. As shown in that figure, the PCB resonant frequency decreases with an increase in proof mass density, i.e. the

higher the proof mass, the lower the resonant frequency. In addition, the new analytical model (Euler model in the figure) provides results that are closer to the FEA than the previous model.

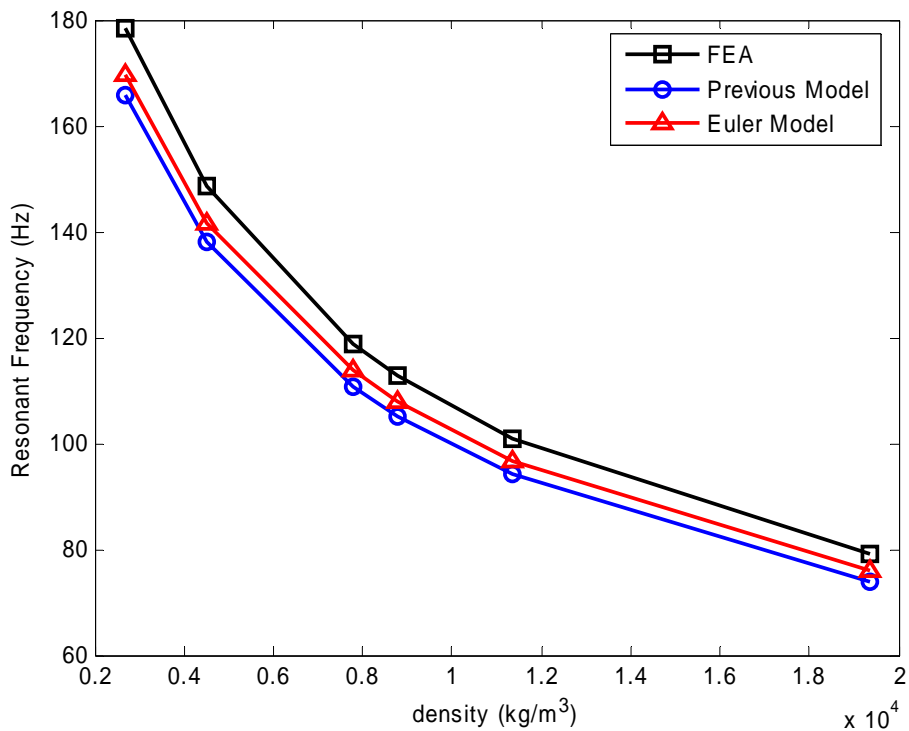


Figure 17. Weight Effect of the Proof Mass on the Resonant Frequency.

Second, the length effect of the proof mass on the resonant frequency is also studied while the mass and the width of the proof mass is kept stable, which means varying the length of the proof mass will also change its thickness. The length effect result of the proof mass is shown in Figure 18, where the new analytical frequency model is simply called the Euler model. It turns out that an increase of the proof mass length leads to an increase of the resonant frequency with the same weight of the proof mass. Further, it is clear that the result of the previous model has a very different trend from the results of the new analytical model (Euler model in the figure) and the finite element analysis, which demonstrates that the new analytical model more accurately predicts of the proof mass length effect on the resonant frequency of the PCB generator than the previous model in the literature.

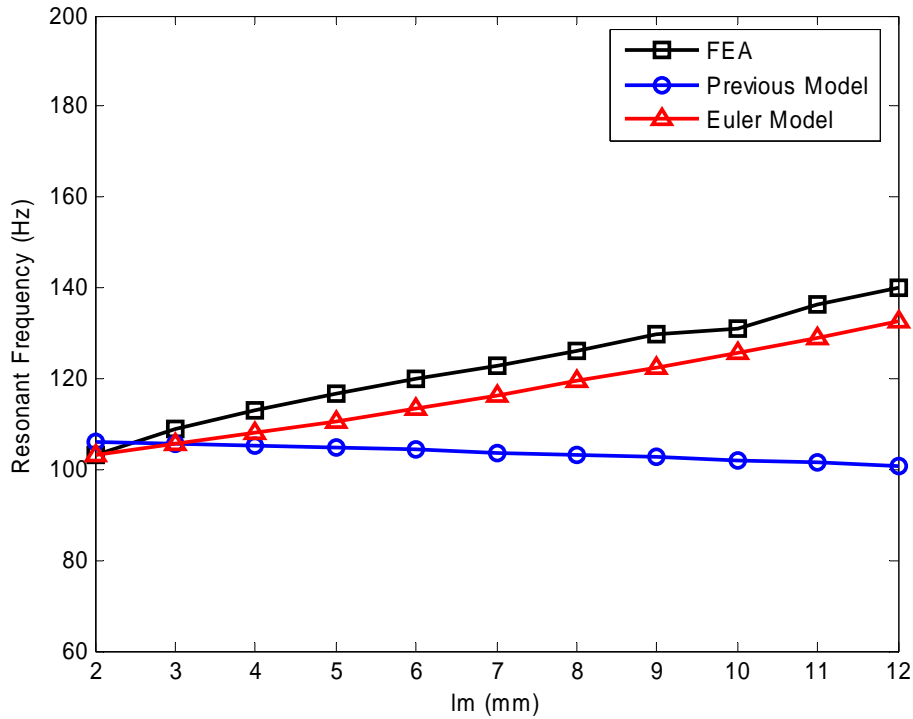


Figure 18. Length Effect of the Proof Mass on the Resonant Frequency.

In brief, the geometric effects of the bimorph and the geometric and mass effects of the proof mass have been studied. The analysis results can be used as guidelines for the design of a PCB generator. For example, if the resonant frequency of a given design is higher than the frequency of ambient vibration, there are several ways to reduce it, such as increasing the length of the PZT layer, decreasing the thickness of the PZT layer, selecting a proof mass composed of a higher density material, or directly bonding additional proof mass to the original PCB. Further, since the specific resonant frequency of the device can be predicted using the new analytical model, it is feasible to appropriately select the dimensions of the piezoelectric bimorph and the proof mass to tune the resonant frequency of the generator to the ambient vibration frequency so that maximum power can be harvested. Laboratory experiments were performed to further validate the new frequency model and to test the SDOF tip displacement calculation presented in Equation 3.17. A description of the experiment and the results are presented in the next section.

## Experimental Validation of Frequency Model and Tip Displacement Model

A laboratory prototype of the piezoelectric bimorph generator (Q220-A4-203Y) was set up and tested, as is shown in Figure 19.

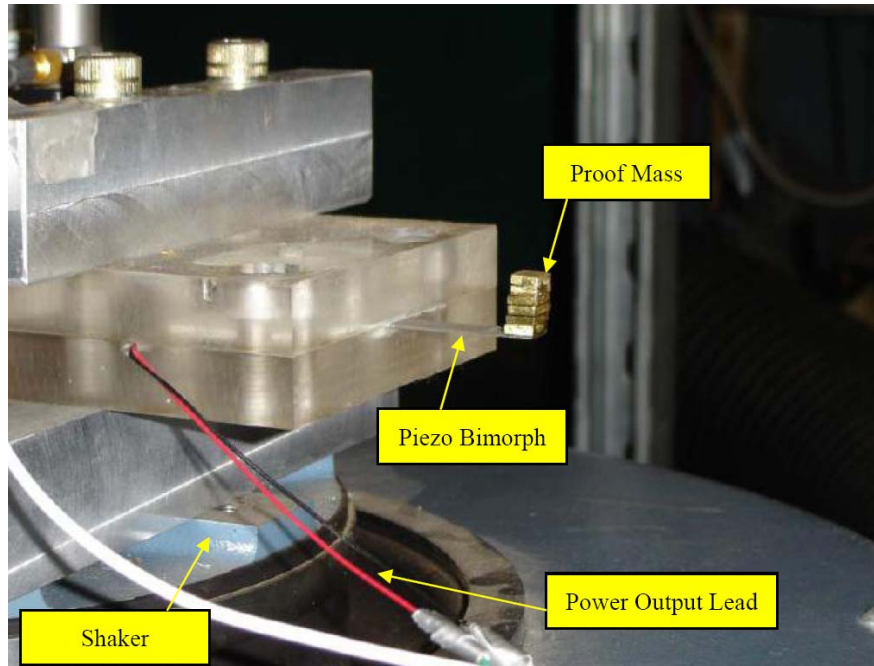


Figure 19. A Prototype of PCB Energy Harvester.

During the testing, one piece of brass proof mass with the dimensions of  $5.3\text{mm} \times 6.345\text{mm} \times 1.6\text{mm}$  was added to the top surface of the previously bonded proof mass at each step, as is shown in Figure 20. A sinusoidal sweep test of the piezoelectric device was performed with the shaker input acceleration amplitude kept at  $11.8 \text{ m/s}^2$ . The resonant frequency of the structure was obtained from the Fast Fourier Transform (FFT) of the prototype open-circuit voltage data, which was collected using MATLAB XPC Target, based on the principle that the power output of the PCB generator is maximized at its resonant frequency. The tip displacement of the prototype was measured using a PSV300 vibrometer in additional experiments.

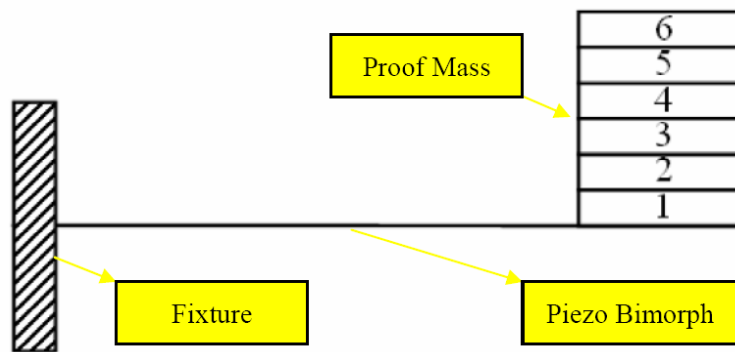


Figure 20. Experimental Procedures of PCB Energy Harvester.

### Experimental Results of the Resonant Frequency

The resonant frequency results of the prototype with 0-6 pieces of brass proof mass are shown in Figure 21, where the new analytical frequency model is simply called the Euler model. The figure compares Shen et al.'s (2006) model, the new analytical model (Euler Model), and the FEA against the experimental results. Table 5 provides the specific experimental data and the results calculated from the three models. It can be seen that increasing the proof mass height leads to a decrease of the prototype resonant frequency, which demonstrates the aforementioned weight effect of the proof mass on the resonant frequency of the generator, i.e. the higher the proof mass, the lower the resonant frequency. Further, it can be seen that each of the models produces results that are relatively close to those of the experiment. This would seem to suggest that each of the three models can be used as an effective design tool for determining the appropriate dimensions of a PCB generator to match its resonant frequency to the frequency of the ambient vibrations and thus maximize the harvested energy.

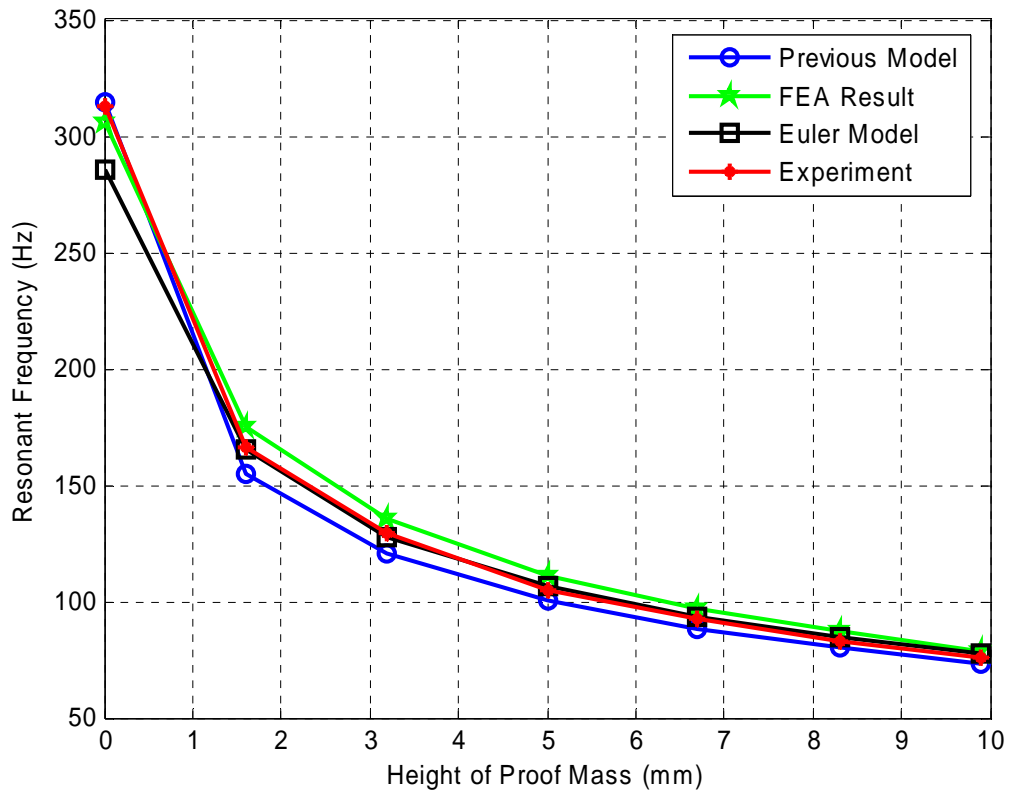


Figure 21. The Resonant Frequency Results by Models and Experiment

Table 5

Specific Data of Three Models and Experiment

<i>Case</i>	<i>0 P</i>	<i>1 P</i>	<i>2 P</i>	<i>3 P</i>	<i>4 P</i>	<i>5 P</i>	<i>6 P</i>
<i>Models</i>	(Hz)						
Previous	314.7	154.9	120.5	100.3	88.2	80.0	73.4
FEA	306.1	175.3	135.3	111.4	96.9	87.4	78.4
Euler Model	285.6	165.3	127.8	106.5	93.7	85.0	78.1
Experiments	312.5	166.0	129.4	105.0	92.8	83.0	75.7

Note: "n P" means n pieces of brass proof mass added to the bimorph.

## Experimental Results of the Tip Displacement

As the thickness of the proof mass varies, the tip displacement of the prototype can be calculated using the SDOF tip displacement model shown in Equation 3.17, where the resonant frequency is calculated using the new analytical frequency model, and the damping ratio is  $\zeta \approx 0.03$ , since the mechanical quality factor for the bimorph Q220-A4-203Y is  $Q \approx 15$ , according to Piezo System, the manufacturers of the PCB. The experimental measurement of the tip displacement is performed using a PSV300 laser vibrometer.

The tip displacement results of the SDOF model and the experiment are shown in Figure 22. It can be seen that, as predicted, the tip displacement of the piezoelectric prototype increases with the increasing thickness of the proof mass, i.e. the weight increase of the proof mass leads to an increase of the tip displacement. With the smaller proof masses, the model and the experiment match only in general trends. However, with increasing proof masses, the matches become significantly closer. In addition, the relationship between the tip displacement and the resonant frequency is shown in Figure 23, where the tip displacement is inverse proportional to the resonant frequency, which is compatible with Equation 3.17.

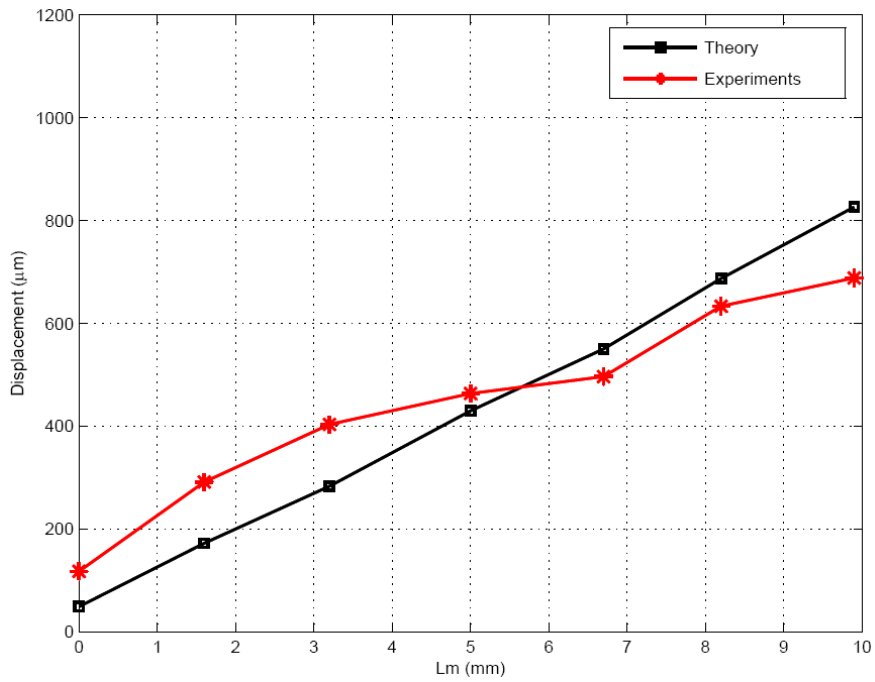


Figure 22. Tip Displacement Results of SDOF Model and Experiment.

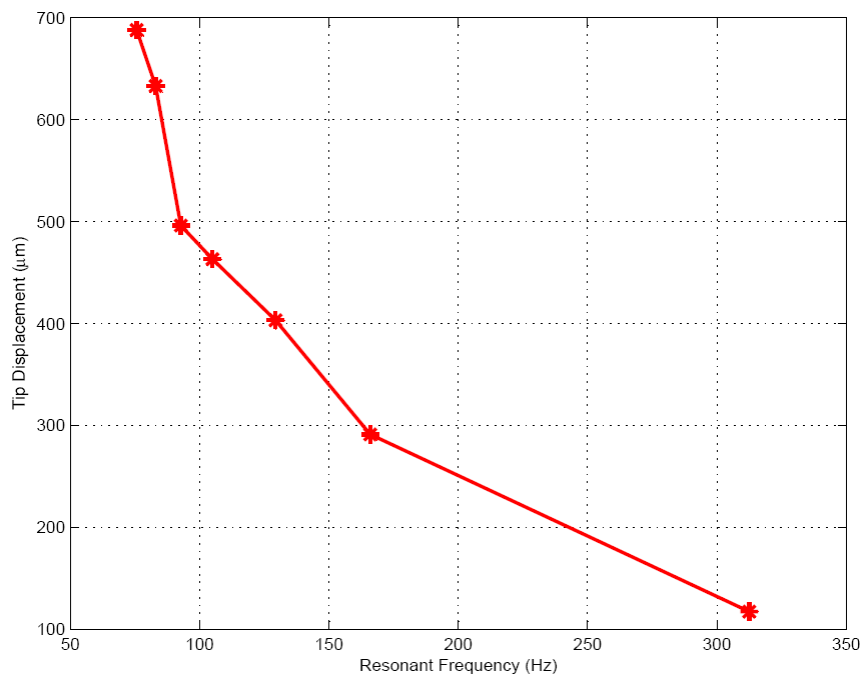


Figure 23. Experimental Results of Tip Displacement vs. Resonant Frequency.

## Summary

In an effort to study the geometric effect of the bimorph and the proof mass on the resonant frequency and the tip displacement of the PCB generator, a new analytical model of the resonant frequency of the PCB generator and an SDOF tip displacement model were presented and validated through finite element analysis and experiments in this chapter.

The analyses show that the resonant frequency of the PCB generator increases with decreasing length or increasing thickness of the piezoelectric bimorph, or with the weight decrease and the length increase of the proof mass. Those relations may be used as guidelines to regulate the resonant frequency of the generator. In addition, the frequency model comparison and the partial experimental demonstration show that, to some extent, the new analytical model can better predict the resonant frequency of the device than the model presented by Shen et al. (2006), although the latter has a more concise explicit expression. Together with the FEA, the new analytical model can be used to select the appropriate dimensions of the bimorph and the proof mass to tune the resonant frequency of the generator to the frequency of the ambient vibration so that maximum power can be harvested.

Second, the single degree of freedom (SDOF) model of the tip displacement shows that the tip displacement is inversely proportional to the square value of the resonant frequency of the PCB generator. In addition, compared with the experiment, the SDOF model can provide a rough prediction of the tip deflection of the PCB generator. Based on the frequency models and the tip displacement model, an examination of the modified voltage and power output model of the PCB generator will be presented in the next chapter.

## CHAPTER 4

### ANALYTICAL MODELING FOR PCB ENERGY HARVESTER

A reasonable goal for a piezoelectric energy harvester design is to realize completely self-powered portable electronics or wireless sensor systems. Therefore, it is very important to study the factors that influence the power output of piezoelectric generators. In this chapter, based on the work presented in Zhang and Williams (2010A), two previous models on the power output of a piezoelectric cantilever bimorph (PCB) energy harvester are first described. The development of a modified power model is then presented. The three analytical models are then compared against the results of a laboratory experiment. The results indicate that the three models can closely predict the open-circuit voltage and closed-circuit voltage of a PCB generator and can also be used to produce a rough prediction of the power output.

#### **Previous Models for Power Output of PCB Generator**

Numerous mathematical models of the piezoelectric generators have been well developed and widely accepted in the field of energy harvesting over the years. Among those models, there are two widely applied models, i.e. the mechanical equivalent spring-damper-mass model and the electrical equivalent resistor-inductor-capacitor model. In this section, these two models will be briefly introduced, and their performance in predicting the electrical output of a PCB will be examined in the later sections. The geometric configuration of the PCB is identical to the device shown previously Figure 9, where the piezoelectric bimorph is cantilevered and a proof mass is bonded to its free end.

### Mechanical Equivalent Spring-Mass-Damper Model

Williams and Yates (1996) proposed a general model for the conversion of vibration energy into electrical energy. Their model was independent of the conversion mechanism; that is, it was applicable for electromagnetic, electrostatic, or piezoelectric energy harvesters. That general model treats the PCB as a spring-damper-mass system, as is shown in Figure 24. That model is identical to the SDOF model used to predict the tip displacement of the PCB, as described in Chapter 3.

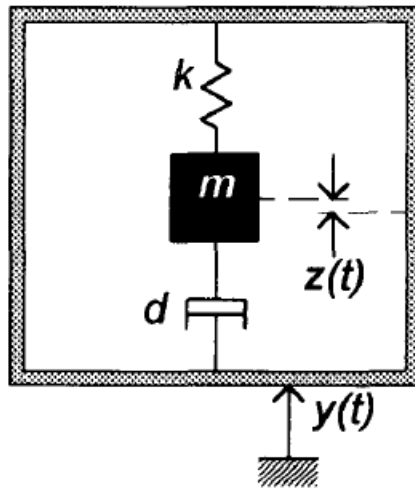


Figure 24. A General Model for Vibration Energy Conversion (Williams & Yates, 1996).

The basic equation for the motion of the generator can be obtained with:

$$m\ddot{z} + d\dot{z} + kz = -m\ddot{y} \quad (4.1)$$

where  $z$  is the tip displacement of the PCB,  $y$  is the base motion,  $m$  is the proof mass, and  $d$  and  $k$  are the damping coefficient and the spring stiffness constant of the device, respectively.

The force acting on the whole system that is induced by the ambient vibration is:

$$F = -m\ddot{y}(t) \quad (4.2)$$

The vibration-induced instantaneous mechanical power of the PCB generator is then

obtained as a product of the force acting on the system and simultaneous system velocity:

$$p(t) = F * [\dot{y}(t) + \dot{z}(t)] = -m\ddot{y}(t) * [\dot{y}(t) + \dot{z}(t)] \quad (4.3)$$

By assuming the sinusoidal vibration of the form,  $y(t) = Y_0 * \cos(\omega t)$ , the power output of the PCB generator was derived by Williams and Yates (1996) to be:

$$|P(j\omega)| = \frac{m\zeta Y_0^2 \omega^3 \frac{\omega}{\omega_n}}{\left(1 - \frac{\omega^2}{\omega_n^2}\right)^2 + \left(2\zeta \frac{\omega}{\omega_n}\right)^2} \quad (4.4)$$

where  $\omega_n$  is the resonant frequency of the generator,  $\omega$  is the driving frequency of the ambient vibration,  $Y_0$  is the amplitude of ambient vibration displacement, and  $\zeta$  is the system damping ratio. To relate Equations (4.3) and (4.4), it is necessary to use the well-known relationships  $k = m\omega_n^2$  and  $d = 2m\zeta\omega_n$ .

If the resonant frequency of the generator matches the frequency of the ambient vibration, the above model reduces to:

$$|P(j\omega)| = \frac{mY_0^2 \omega_n^3}{4\zeta} \quad (4.5)$$

The above equation represents the power output of the PCB generator under an open-circuit condition. Therefore, the open-circuit voltage can then be derived from it. As suggested by Park (2001), the best-fit circuit model for the PZT sensor is a voltage generator in series with a capacitor, as shown in Figure 25, where  $C_b$  represents the internal capacitance of the piezoelectric bimorph. For sinusoidal ambient vibration at the resonant frequency of the PCB (i.e.  $\omega = \omega_n$ ), the open-circuit voltage  $V_{open}$  is assumed to be  $u(t) = \sqrt{2} * U_{eff} * \sin(\omega_n t)$ , where  $U_{eff}$  is the effective value of the AC voltage.

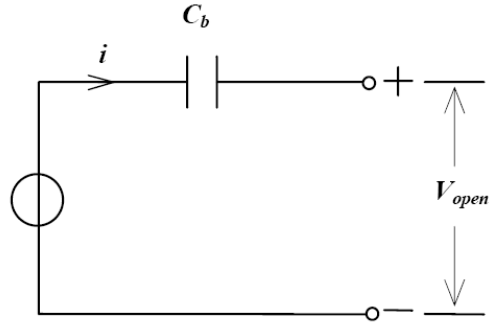


Figure 25. Open-circuit Model of Piezoelectric Energy Harvester.

The AC current is defined as the time derivative of electrical charge across the circuit:

$$i(t) = \frac{dQ(t)}{dt} = C_b * \frac{du(t)}{dt} = \sqrt{2} * I_{eff} * \cos(\omega_n t) \quad (4.6)$$

where  $I_{eff} = C_b \omega_n U_{eff}$  is the effective value of the AC current. The amplitude of the reactive power consumed by the capacitor is then:

$$Q_{amp} = - U_{eff} * I_{eff} = - C_b \omega_n U_{eff}^2 \quad (4.7)$$

Substituting Equation 4.7 into Equation 4.5, the effective value of the PCB open-circuit voltage is:

$$U_{eff} = \frac{Y_0 \omega_n}{2} \sqrt{\frac{m}{\zeta C_b}} \quad (4.8)$$

Hence, the transient open-circuit voltage of the generator is given by:

$$u(t) = \sqrt{2} U_{eff} \sin(\omega_n t) = Y_0 \omega_n \sqrt{\frac{m}{2\zeta C_b}} \sin(\omega_n t) \quad (4.9)$$

For a closed circuit, the equivalent capacitor of the piezoelectric bimorph is connected in series with the load, as is shown in Figure 26.

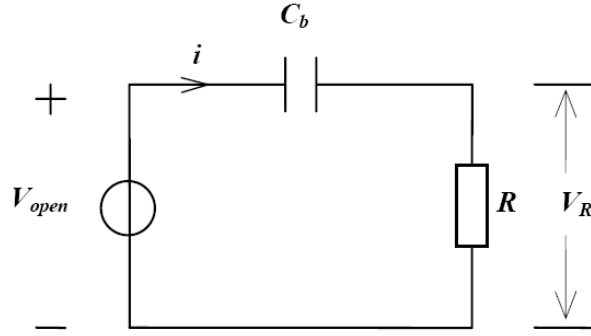


Figure 26. Close-circuit Model of Piezoelectric Energy Harvester

Using the complex impedances, the open-circuit voltage of the device can be simplified as  $u(t) = U_{eff} \angle 0^\circ$ , and the total impedance of the close circuit is given by:

$$Z = R + \frac{1}{j\omega_n C_b} = \sqrt{R^2 + \frac{1}{(\omega_n C_b)^2}} \angle -\varphi \quad (4.10)$$

where  $\varphi = \tan^{-1}\left(\frac{1}{\omega_n C_b R}\right)$ . The voltage across the resistive load is then calculated as:

$$u_R = \frac{R}{Z} u(t) = \frac{\omega_n C_b R}{\sqrt{1 + \omega_n^2 C_b^2 R^2}} U_{eff} \angle \varphi \quad (4.11)$$

Hence, the transient close-circuit voltage across the resistive load is given by:

$$u_R(t) = \sqrt{2} * \frac{\omega_n C_b R}{\sqrt{1 + \omega_n^2 C_b^2 R^2}} U_{eff} \sin(\omega_n t + \varphi) \quad (4.12)$$

The power consumption of the resistive load can then be directly calculated as:

$$P_R = \frac{U_R^2}{R} = \frac{\omega_n^2 C_b^2 R}{1 + \omega_n^2 C_b^2 R^2} U_{eff}^2 \quad (4.13)$$

where  $U_R$  represents the effective value of the AC voltage of the resistive load. Further, the optimal value of  $R$  for the maximum power output of the generator is found to be:

$$R_{opt} = \frac{1}{\omega_n C_b} \quad (4.14)$$

## Electrical Equivalent Circuit Model

A convenient method for studying the characteristics of a PCB is to utilize an electrical equivalent circuit model that expresses both mechanical and electrical portions of the piezoelectric system as circuits. For the PCB generator shown in Figure 27, an equivalent circuit representation developed by Roundy (2004) is shown in Figure 28, where  $\sigma_{in}$  represents the stress generator excited by input vibration; inductor  $L_m$  represents the mass of the generator; resistor  $R_b$  represents the mechanical damping; capacitor  $C_k$  represents the mechanical stiffness;  $n$  is the number of turns of the transformer, which represents the electromechanical coupling of the PCB generator;  $C_b$  represents the inner capacitance of piezoelectric bimorph; and  $V$  represents the open-circuit voltage.

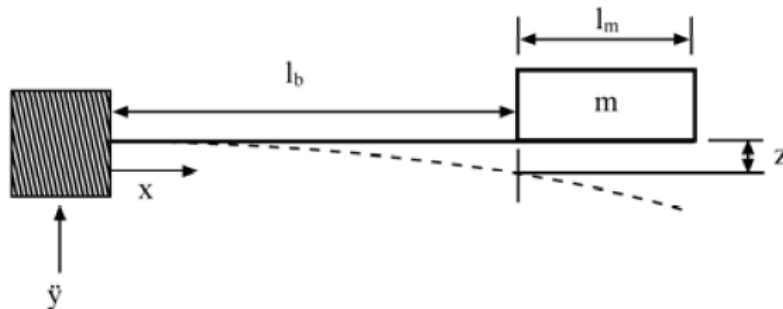


Figure 27. A Schematic Diagram of the Generator, Roundy (2004).

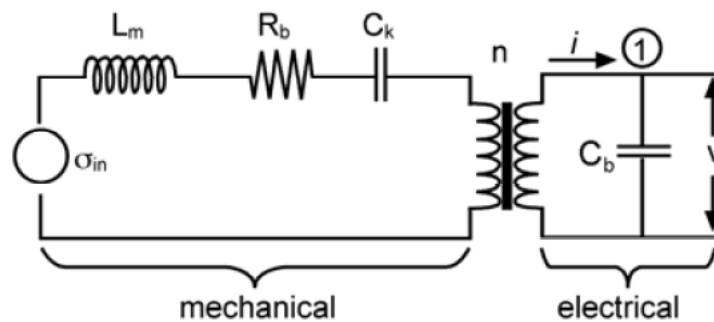


Figure 28. Circuit Representation of the Piezoelectric Generator, Roundy (2004).

The closed-circuit voltage of a generator with a resistive load was derived by Roundy (2004) as:

$$V = \frac{j2\omega c_p d_{31} t_p / (a\epsilon k_2)}{\frac{\omega_n^2}{RC_b} - \left( \frac{1}{RC_b} + 2\zeta\omega_n \right) \omega^2 + j\omega[\omega_n^2(1+k_{31}^2) + \frac{2\zeta\omega_n}{RC_b} - \omega^2]} \quad (4.15)$$

where  $R$  is the resistive load and the open-circuit voltage can be obtained with  $R \rightarrow \infty$ ;

$$k_2 = \frac{(L-L_m)^2(4L-L_m)}{3L(t_{sh}+t_p)}; k_{31} = \frac{d_{31}^2 c_p}{\epsilon}$$

is the coupling coefficient of the generator;  $\omega$  and  $A_m$  are the driving frequency and the acceleration amplitude of the base vibration, respectively;  $\omega_n$  is the resonant frequency of the device;  $c_p$ ,  $L_b$ ,  $t_p$ ,  $\epsilon$ , and  $d_{31}$  are the Young's modules, effective length, thickness, dielectric constant, and piezoelectric strain coefficient of a single piezoelectric layer, respectively;  $a = 1$  for a pair of piezoelectric layers wired for series operation and  $a = 2$  for two piezoelectric layers wired for parallel operation;  $c_{sh}$  and  $t_{sh}$  are the Young's modules and the thickness of the central brass shim;  $L_m$  is the length of the proof mass; and  $\zeta$  is the damping ratio of the device.

If the driving frequency  $\omega$  of the base vibration matches the resonant frequency  $\omega_n$  of the PCB generator and the load is resistive, the rms power transferred to the load and the optimal load resistance are derived by Roundy (2004) as:

$$P = \frac{1}{2\omega_n^2} \frac{RC_b^2 \left( \frac{2c_p d_{31} t_p}{k_2 a \epsilon} \right)^2 A_m^2}{(4\zeta^2 + k_{31}^4)(RC_b \omega_n)^2 + 4\zeta k_{31}^2 (RC_b \omega_n) + 4\zeta^2} \quad (4.16)$$

$$R_{opt} = \frac{1}{\omega_n C_b} \frac{2\zeta}{\sqrt{4\zeta^2 + k_{31}^4}} \quad (4.17)$$

## **A Modified Analytical Model for PCB Generator**

Based on an analysis of internal energy and thermodynamic equilibrium, Wang et al. (1999) derived an analytical expression for the sensor effect of a PCB subjected to mechanical input, including moment  $M$ , tip force  $F$ , and body force  $p$  excitations. Kim, Johnson, and Clark (2004) used the same principle to study the voltage generation of unimorph, interdigitated unimorph, bimorph, and interdigitated bimorph cantilever benders and diaphragms. Further, Ng and Liao (2005) and Ajitsaria et. al (2007) extended the work by Wang et al. and Kim, Johnson, and Clark and studied the voltage generation of a piezoelectric cantilever bimorph with a proof mass bonded at the free end. However, the effect of the proof mass on the piezoelectric effect of the bimorph was not taken into consideration in the above studies. In this section, a modified analytical model for the PCB generator will be presented based on the previous research.

It is assumed that the PZT parts under the proof mass do not contribute to the voltage generation of the PCB generator subjected to ambient vibration. In other words, the PZT material under the proof mass will be treated as a rigid body and will not result in any piezoelectric effect in this modified model. The legitimacy of this assumption is demonstrated by the equivalent strain distribution of a PCB generator under first bending mode, as calculated using FEA and shown in Figures 29 and 30. In those figures, the equivalent elastic strain distribution of the top and bottom surfaces reveals that the induced strain of the PZT material under the proof mass is negligible, as compared with PZT material not covered by the proof mass. As such, the material under the proof mass will result in negligible electrical potential generation based on the strain-dependent characteristics of piezoelectric materials. To further confirm this assumption, the equivalent strain distribution of the PCB generator with a longer proof mass is shown in Figures 31 and 32, where the equivalent elastic strain of the PZT part under the longer proof mass is still

negligible. These results are not surprising, as the relatively tall proof mass will result in a much higher bending stiffness than the much thinner beam section. A second assumption in the model is that the proof mass will be treated as a point mass when calculating its acting force on the bimorph.

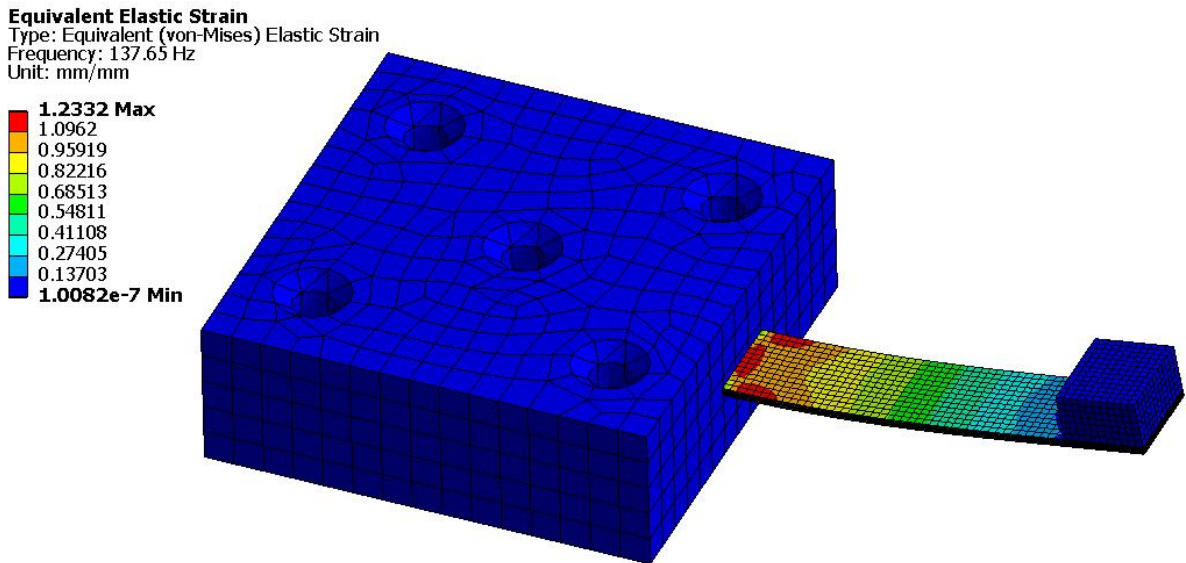


Figure 29. Top Surface Equivalent Elastic Strain of PCB Generator.

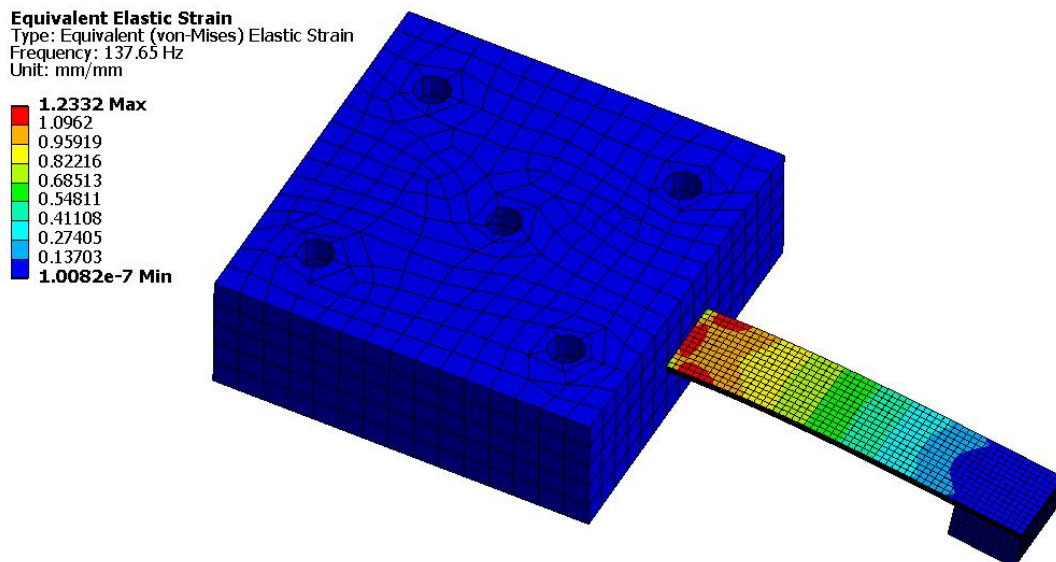


Figure 30. Bottom Surface Equivalent Elastic Strain of PCB Generator.

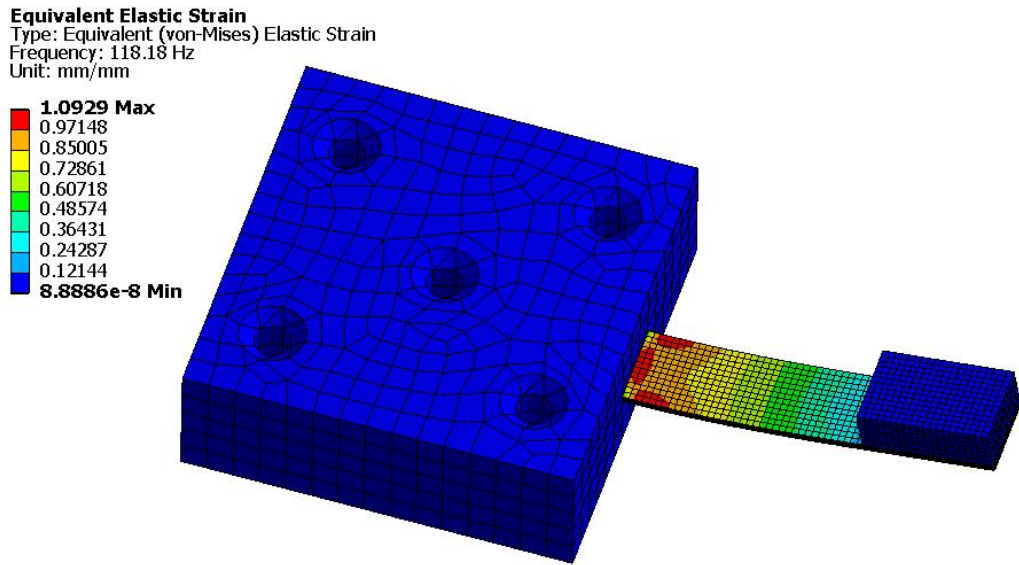


Figure 31. Top Surface Equivalent Strain of PCB Generator with Longer Proof Mass.

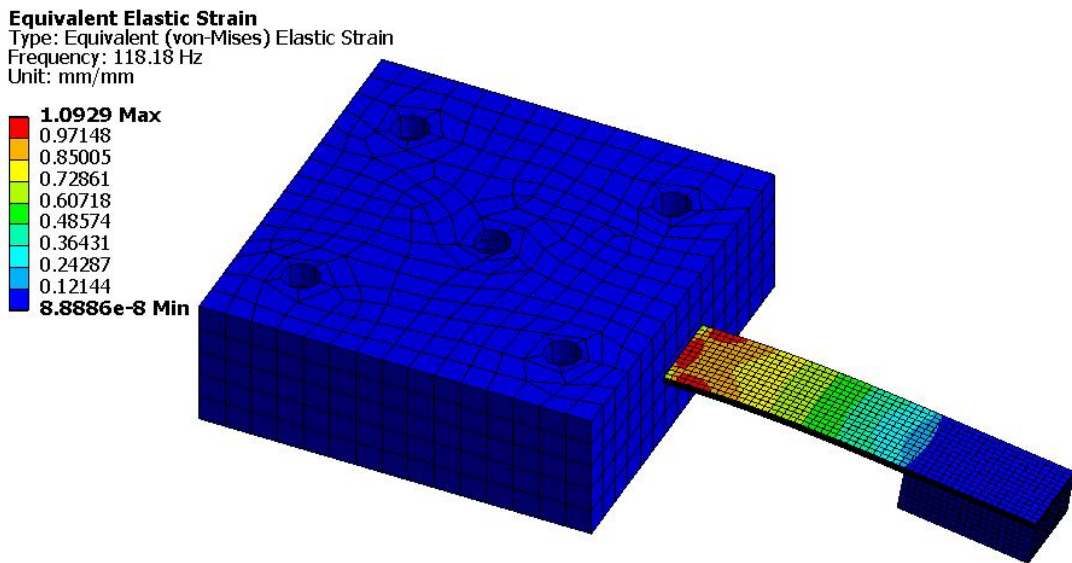


Figure 32. Bottom Surface Equivalent Strain of PCB Generator with Longer Proof Mass.

The detailed derivation of the modified model based on Kim (2002) for the voltage and power output of the PCB generator is presented next. The constitutive equations for the top and bottom PZT layer are expressed by the following equations:

$$\begin{cases} S_1 = \frac{1}{c_p} \sigma_1 \mp d_{31} E_3 \\ D_3 = \mp d_{31} \sigma_1 + \varepsilon_{33} E_3 \end{cases} \quad (4.18)$$

where the operation symbol  $\mp$  indicates that the top and bottom PZT layers of the bimorph are poled in opposite directions;  $S_1$  and  $\sigma_1$  are the mechanical strain and stress in the longitudinal direction (the '1' direction), respectively;  $c_p$  is the piezoelectric Young's modulus;  $D_3$  and  $E_3$  are the electric displacement and electric field intensity in the transverse '3' direction, respectively;  $d_{31}$  is the piezoelectric strain coefficient; and  $\varepsilon_{33}$  is the dielectric constant.

Since the central brass shim is an elastic layer, the stress across it and the PZT layers can then be expressed as:

$$\begin{cases} \sigma_1 = c_p (S_1 \pm d_{31} E_3) \\ \sigma_{sh} = c_{sh} S_1 \end{cases} \quad (4.19)$$

Due to the geometric symmetry of the piezoelectric bimorph, the neutral axis is the middle surface of the central brass shim. According to Euler beam theory, the relationship between strain  $S_1$  and curvature  $\rho$  can be obtained with:

$$S_1 = -\rho z \quad (4.20)$$

where  $z$  represents the distance from the neutral surface. Substituting Equation 4.20 into Equation 4.19, the stress of the PCB generator is then expressed by:

$$\begin{cases} \sigma_1 = -c_p (\rho z \mp d_{31} E_3) \\ \sigma_{sh} = -c_{sh} \rho z \end{cases} \quad (4.21)$$

Then the moment in the PCB generator can be calculated by integrating the stress across the cross section:

$$M = \int_{A_{PZT\_top}} \sigma_{1_{PZT\_top}} z dz + \int_{A_{center}} \sigma_{center} z dz + \int_{A_{PZT\_bottom}} \sigma_{1_{PZT\_bottom}} z dz \quad (4.22)$$

where  $A_{PZT\_top}$ ,  $A_{Center}$ , and  $A_{PZT\_bottom}$  represents the cross sectional areas of the top PZT, central brass, and bottom PZT layers, respectively. Substituting Equation 4.21 into Equation 4.22:

$$M = \int_{\frac{t_{sh}}{2}}^{\frac{t_{sh}}{2}+t_p} c_p (-\rho z + d_{31} E_3) w z dz + \int_{-\frac{t_{sh}}{2}}^{\frac{t_{sh}}{2}} -c_{sh} \rho z w z dz + \int_{-\frac{t_{sh}}{2}}^{-\frac{t_{sh}}{2}+t_p} c_p (-\rho z - d_{31} E_3) w z dz \quad (4.23)$$

According to Ng and Liao (2005), the equivalent excitation force of the proof mass acting on the piezoelectric bimorph subjected to the ambient vibrations can be obtained as:

$$F = -m\omega^2 Y * \sin(\omega t) \quad (4.24)$$

where  $m$  is the mass of the proof mass,  $Y$  is the displacement amplitude of the proof mass, and  $\omega$  is the driving frequency of ambient vibration. Thus, the moment induced by the excitation force  $F$  can be obtained as:

$$M = F * (L - \frac{1}{2} L_m - x) \quad (4.25)$$

where  $x$  is the distance from the clamped end to the center of the proof mass. Combining Equation 4.23 and Equation 4.25, the curvature  $\rho$  of the PCB generator can be solved with:

$$\rho = \frac{F}{g_1} (L - \frac{1}{2} L_m - x) - \frac{g_2}{g_1} E_3 \quad (4.26)$$

where  $g_1 = -\frac{2}{3} c_p w (t_p^3 + \frac{3}{2} t_p^2 t_{sh} + \frac{3}{4} t_p t_{sh}^2) - \frac{1}{12} c_{sh} w * t_{sh}^3$  and  $g_2 = c_p w d_{31} (t_p^2 + t_p t_{sh})$ .

The energy densities of the PZT layers and the central brass layer are then given by:

$$\begin{cases} dU_{PZT} = \frac{1}{2} S_1 \sigma_1 + \frac{1}{2} D_3 E_3 \\ dU_{shim} = \frac{1}{2} S_1 \sigma_{sh} \end{cases} \quad (4.27)$$

where the 2<sup>nd</sup> term on the right-hand side of the 1<sup>st</sup> equation represents the energy density contributed by the piezoelectric effect, while the 1<sup>st</sup> terms on the right-hand side of both

equations represent the elastic energy densities of the different sections. After substituting Equations 4.21 and 4.26 into Equation 4.27, the specific energy densities of the PCB generator are:

$$\begin{cases} dU_{PZT\_top} = \frac{1}{2}c_p\rho^2z^2 + \frac{1}{2}(-c_p d_{31}^2 + \varepsilon_{33})E_3^2 \\ dU_{PZT\_bot} = \frac{1}{2}c_p\rho^2z^2 + \frac{1}{2}(-c_p d_{31}^2 + \varepsilon_{33})E_3^2 \\ dU_{sh} = \frac{1}{2}c_{sh}\rho^2z^2 \end{cases} \quad (4.28)$$

From the above equation, it can be seen that the energy density of the top PZT layer is exactly identical to that of the bottom PZT layer, although they always operate in the opposite modes, i.e., one is in tension and the other is in compression. Thus, the total internal energy in the bimorph can be calculated by integrating the energy density over the whole device:

$$\begin{aligned} U = & \int_0^L \int_0^w \int_{\frac{t_{sh}}{2}}^{\frac{t_{sh}+t_p}{2}} dU_{PZT\_top} dz dy dx - \int_{L-L_m}^L \int_0^w \int_{\frac{t_{sh}}{2}}^{\frac{t_{sh}+t_p}{2}} \frac{1}{2}(\varepsilon_{33} - c_p d_{31}^2) E_3^2 dz dy dx \\ & + \int_0^L \int_0^w \int_{-\frac{t_{sh}}{2}}^{\frac{t_{sh}}{2}} dU_{sh} dz dy dx \\ & + \int_0^L \int_0^w \int_{-\frac{t_{sh}+t_p}{2}}^{-\frac{t_{sh}}{2}} dU_{PZT\_bot} dz dy dx - \int_{L-L_m}^L \int_0^w \int_{\frac{t_{sh}}{2}}^{\frac{t_{sh}+t_p}{2}} \frac{1}{2}(\varepsilon_{33} - c_p d_{31}^2) E_3^2 dz dy dx \end{aligned} \quad (4.29)$$

where the 2<sup>nd</sup> and the 5<sup>th</sup> terms on the right-hand side of the equation that indicate the piezoelectric effect of the PZT parts under the proof mass is not taken into consideration, due to their previously noted negligible strain generation. Substituting Equation 4.28 into Equation 4.29, the energy of the piezoelectric bimorph can be obtained as:

$$\begin{aligned} U = & \frac{F^2 w g_3}{24 g_1^2} (24 c_p g_5 + c_{sh} t_{sh}^3) - \frac{w g_2 g_4}{24 g_1^2} (24 c_p g_5 + c_{sh} t_{sh}^3) F * E_3 \\ & + [\frac{w g_2^2 L}{24 g_1^2} (24 c_p g_5 + c_{sh} t_{sh}^3) + (\varepsilon_{33} - c_p d_{31}^2)(L - L_m) t_p w] * E_3^2 \end{aligned} \quad (4.30)$$

where  $g_3 = \frac{1}{3}L^3 - \frac{1}{2}LL_m(L - \frac{1}{2}L_m)$ ;  $g_4 = L(L - L_m)$ ; and  $g_5 = \frac{1}{3}(t_p^3 + \frac{3}{2}t_p^2t_{sh} + \frac{3}{4}t_p t_{sh}^2)$ . Since the top PZT layer and the bottom PZT layer are wired for parallel operation, the relationship between the electric field intensity  $E_3$  and the voltage  $V$  across the electrodes is:

$$E_3 = \frac{V}{t_p} \quad (4.31)$$

Substituting the above equation into Equation 4.30 and differentiating it with regard to the voltage  $V$  gives the generated electrical charge:

$$Q = -\frac{wg_2g_4g_6}{48g_1^2t_p}F + \left[ \frac{wg_2^2Lg_6}{48g_1^2t_p^2} + \frac{1}{2t_p}(\epsilon_{33} - c_p d_{31}^2)(L - L_m)w \right] * V \quad (4.32)$$

where  $g_6 = (24c_p g_5 + c_{sh} t_{sh}^3)$ . For the two terms on the right-hand side of the equation, the 1<sup>st</sup> term is the electrical charge induced by the ambient vibration, represented by  $Q_m$ , and the 2<sup>nd</sup> term is the electric charge stored in the bimorph, which cannot be captured for energy harvesting. The inner capacitance of the bimorph can then be found by differentiating the generated electrical charge  $Q$  with respect to  $V$ :

$$C_b = \frac{\partial Q}{\partial V} = \frac{wg_2^2g_6L}{48g_1^2t_p^2} + \frac{1}{2t_p}(\epsilon_{33} - c_p d_{31}^2)(L - L_m)w \quad (4.33)$$

According to Coulomb's Law, the open-circuit voltage of the PCB energy harvester induced by the ambient vibration can be obtained as:

$$V_{open} = \frac{Q_m}{C_b} = \frac{-g_2g_4g_6t_p m \omega_n^2 Y}{[g_2^2g_6L + 24g_1^2t_p(\epsilon_{33} - c_p d_{31}^2)(L - L_m)]} * \sin(\omega_n t) \quad (4.34)$$

where the driving frequency of the ambient vibration is assumed to match the resonant frequency of the device. The closed-circuit voltage and power of the PCB with a resistive load can be calculated by Equation 4.12 and 4.13 from the last section:

$$u_R(t) = \sqrt{2} * \frac{\omega_n C_b R}{\sqrt{1 + \omega_n^2 C_b^2 R^2}} U_{eff} \sin(\omega_n t + \varphi) \quad (4.35)$$

$$P_R = \frac{U_R^2}{R} = \frac{\omega_n^2 C_b^2 R}{1 + \omega_n^2 C_b^2 R^2} U_{eff}^2 \quad (4.36)$$

where  $U_{eff} = \frac{-g_2 g_4 g_6 t_p m \omega_n^2 Y}{\sqrt{2} [g_2^2 g_6 L + 24 g_1^2 t_p (\epsilon_{33} - c_p d_{31}^2) (L - L_m)]}$  and  $\varphi = \tan^{-1}(\frac{1}{\omega_n C_b R})$ .

### Experimental Validation and Model Comparison

Laboratory experiments were performed to provide data against which the modified analytical model could be compared. The laboratory prototype of the PCB generator and the experimental setup are identical to those of the resonant frequency experiment setup described in Chapter 3, where a PCB generator prototype was constructed using a piezoelectric bimorph Q220-A4-203Y and a brass proof mass. A schematic diagram of the experiment setup is shown in Figure 33, where the data acquisition system is realized by the MATLAB XPC Target that was used to both provide the sinusoidal/chirp signal as the input to the electromagnetic shaker and to collect the voltage signal produced by the PCB when subjected to shaker vibration.

The prototype was tested with six different proof mass levels. The different proof mass levels were realized by bonding an additional proof mass onto the top of the previous proof mass. Prior to each voltage collection test, a sinusoidal vibration sweep was performed to obtain the fundamental resonant frequency of the PCB. The driving frequency of the shaker was then set to the resonant frequency of the PCB, and the vibration amplitude of the shaker was set to 1.15 g (11.2 m / s<sup>2</sup>), with a voltage amplitude of 0.75 V input into the shaker controller.

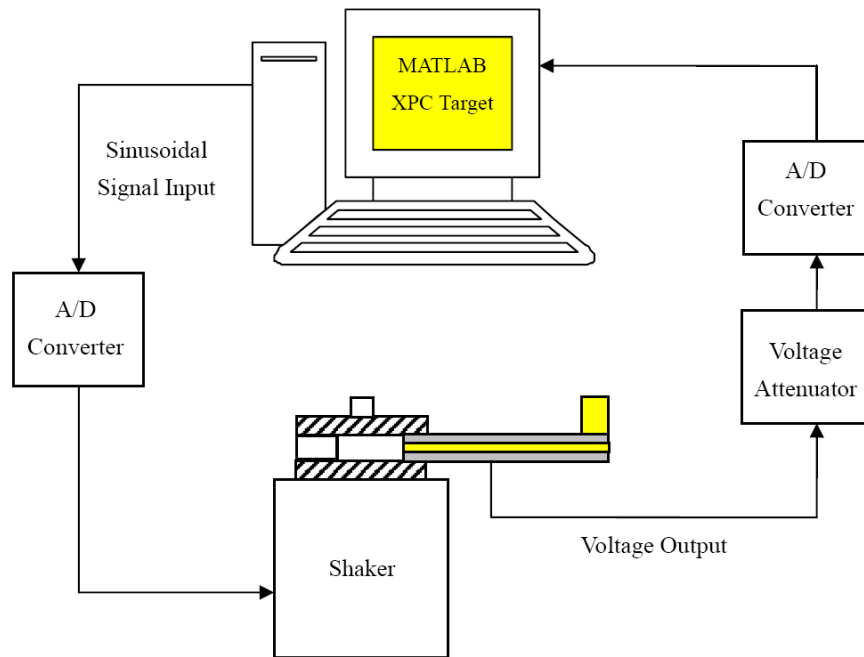


Figure 33. A Schematic Diagram of the Experiment Setup.

The damping ratio of the device was determined experimentally. An impulse excitation was applied to the shaker using a hammer, effectively providing an impulse base excitation for the PCB. An example of the resulting impulse response of the PCB is shown in Figure 34. The damping ratio can be calculated by the two successive peaks of the impact response, as is shown in the following equation, according to Tongue (2002):

$$\zeta = \frac{\ln[x(t_p) / x(t_{p+1})]}{2\pi} \quad (4.37)$$

There were over 75 impulse responses measured, to reduce the risk of measurement errors. The mean damping ratio calculated from the test results measurements was 0.0205, with a standard deviation of 0.0080. The measurement procedure was repeated for the PCB generator with each of the six different proof mass configurations. For all cases, the measured damping ratios were near 0.021, which will be used in the following calculations.

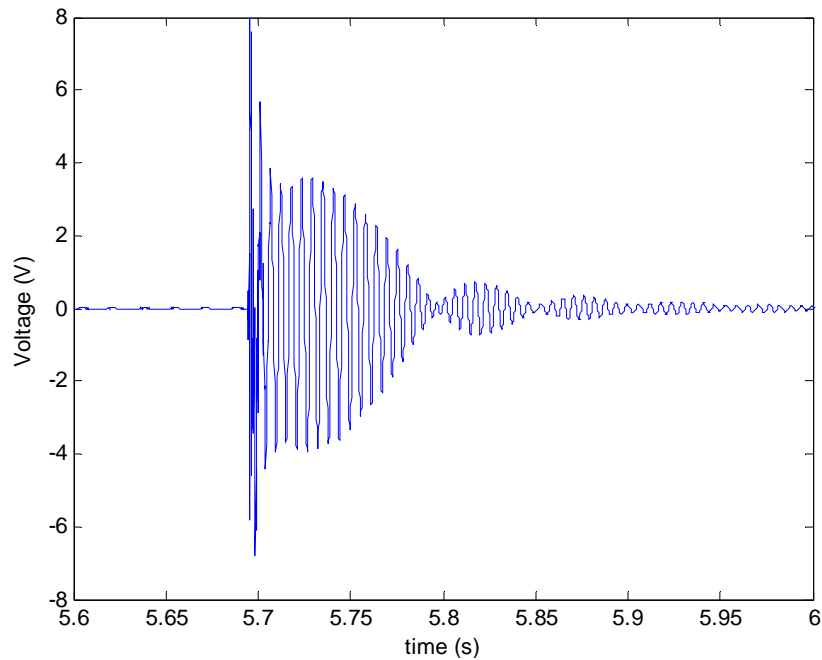


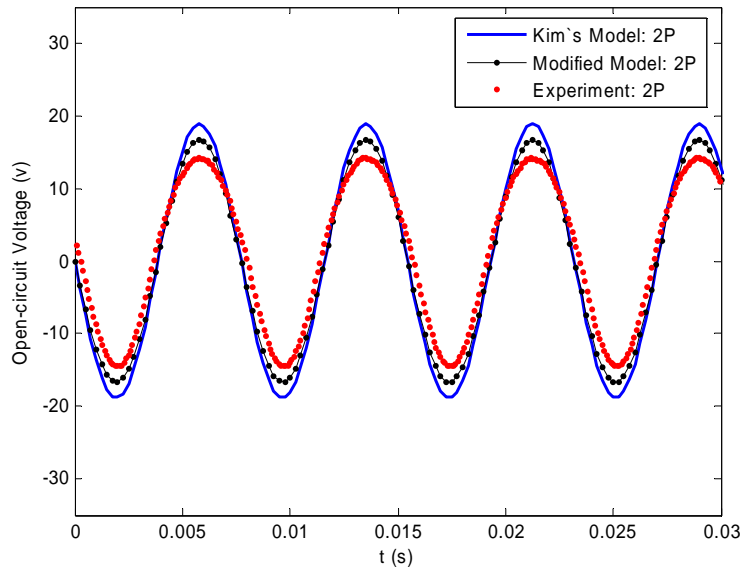
Figure 34. An Example of the Impulse Response of the PCB Generator.

Since the modified model considers the effect of the proof mass on the piezoelectric bimorph, i.e. the piezoelectric effect of the PZT parts under the proof mass will be largely reduced due to the rigidity of the proof mass, as is not covered in the original model by Kim, Johnson, and Clark (2004). In the next section, the modified model will be compared against Kim, Johnson, and Clark's model in terms of the open-circuit voltage and the close-circuit voltage. Both analytical models are compared against the results of the laboratory experiment. In addition, the modified model will also be compared with the previous mechanical equivalent model and the electrical equivalent model.

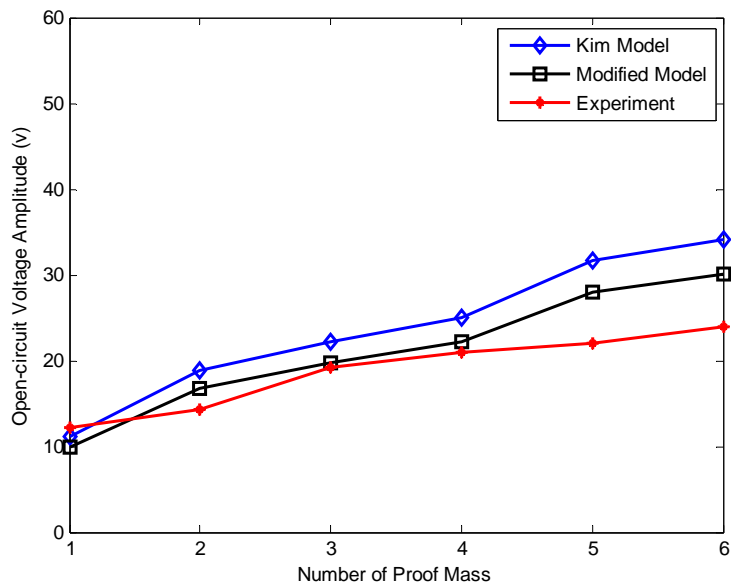
### **Open-Circuit Voltage**

The steady-state open-circuit voltages calculated by the modified model and by Kim, Johnson, and Clark's (2004) model are compared against the experimental results, as shown in Figure 35a and 35b, where '2P' in Figure 33a represents a proof mass of 2. It is noted that the

experimentally measured tip displacement and resonant frequency were accounted for in the calculations, since there is no such a mechanism in the theoretical models to calculate these two parameters.



(a). Time-domain Open-circuit Voltage Response.



(b). Open-circuit Voltage Amplitude Comparison.

Figure 35. Open-circuit Voltage of the Modified Model and Kim, Johnson, & Clark's Model.

It is noted that in Figure 35, all phase angles of the two models and the experiment are discarded for the convenience of comparison. Since the modified model for the PCB generator does not consider the piezoelectric effect of the PZT parts under the proof mass, due to the negligible elastic strain generation of those parts, the open-circuit voltage of the PCB generator calculated by the modified model is smaller than that calculated by Kim, Johnson, and Clark's (2004) model. Further, it is clear in Figure 35b that the open-circuit voltage amplitudes of the modified model are closer to the experimental results than those of Kim, Johnson, and Clark's model.

The open-circuit voltage of the modified model is also compared with that of Williams and Yates' (1996) mechanical equivalent model and Roundy's electrical equivalent model, as are shown in Figure 36, where the  $x$  axis represents the number of pieces of the proof mass and the  $y$  axis represents the open-circuit voltage amplitude of the PCB generator.

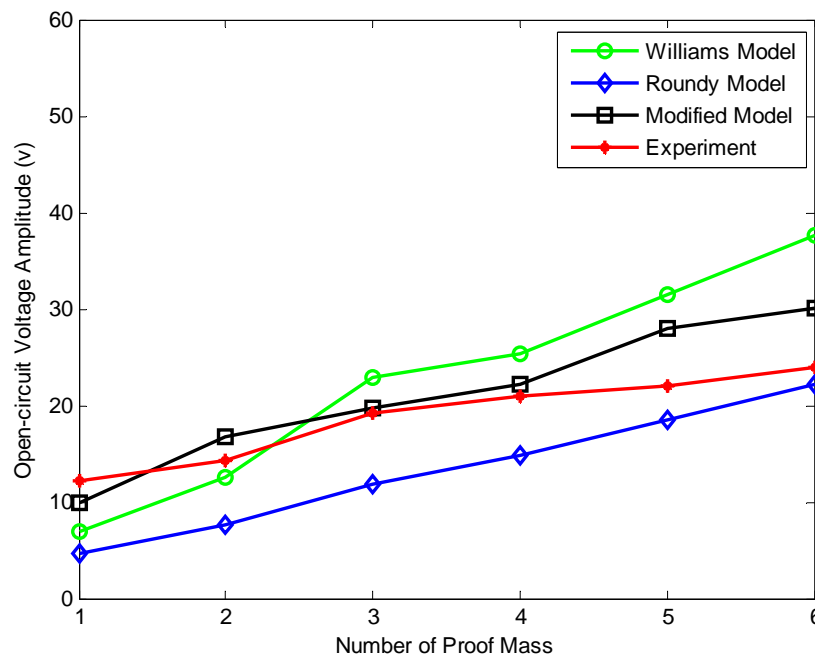


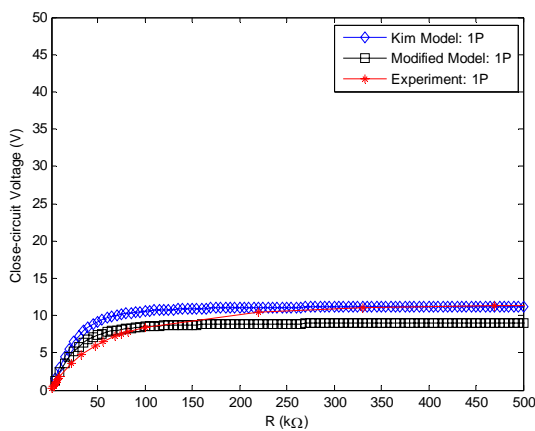
Figure 36. Open-circuit Voltage Amplitude Comparison of Three Models.

Disregarding the phase angle differences between the analytical models and the experimental measurement, it can be seen from Figure 36b that the modified model is better at predicting the open-circuit voltage amplitudes of the PCB generator than Roundy's electrical equivalent model and Williams and Yates' (1996) mechanical equivalent model.

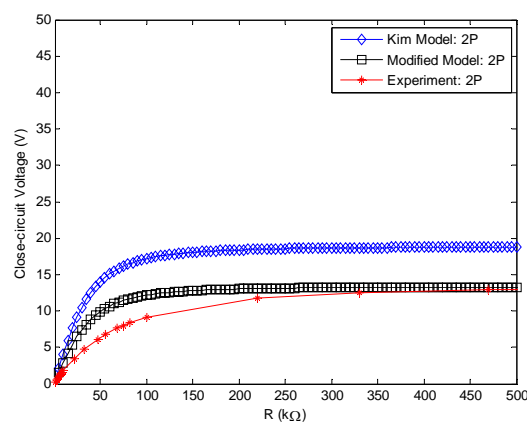
### Close-Circuit Voltage

Closed-circuit tests of the PCB generator connected with resistive loads were also performed for each of the six different proof mass configurations. Tests were performed for each of 23 different resistive loads. The loads varied between  $1\text{ K}\Omega$  and  $0.47\text{ M}\Omega$ . In Figure 37, the closed-circuit peak-to-peak voltages value calculated by Kim, Johnson, and Clark's (2004) model and by the modified model are compared against the experimental data. In that figure, 3P is used to indicate that three proof masses were bonded to the PCB generator.

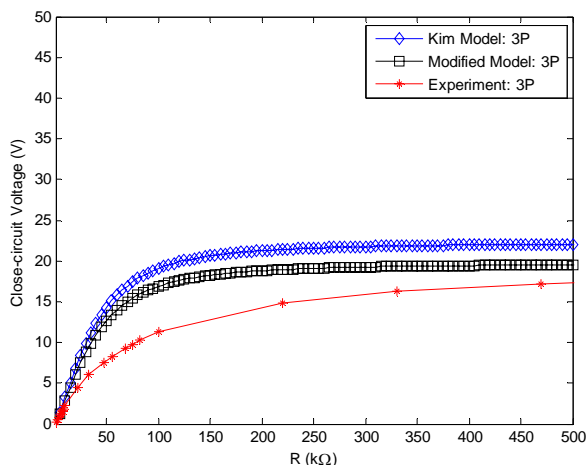
In Figure 37, it is apparent that increasing the load resistance leads to an increased closed-circuit PCB voltage. As the resistance becomes very large, the closed-circuit voltage approaches the open-circuit voltage. Further, it is clear that the increase in proof mass weight leads to the increase of the close-circuit voltage, since more elastic strain energy is generated. In addition, the modified model is closer to the experiment than Kim, Johnson, and Clark's (2004) model.



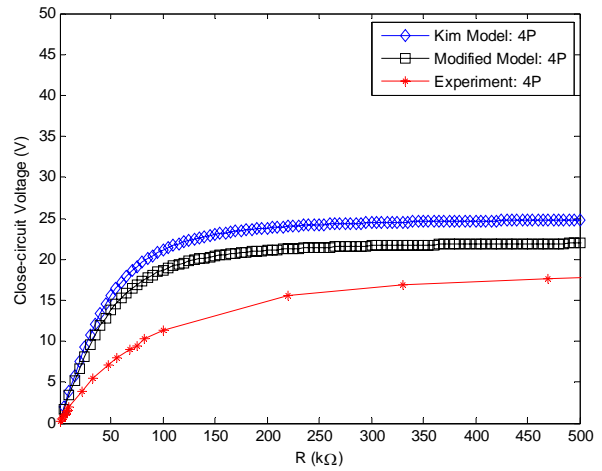
(a). 1 Proof Mass.



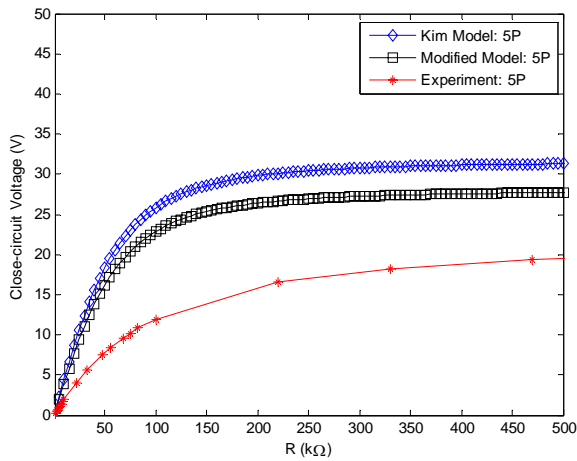
(b). 2 Proof Mass.



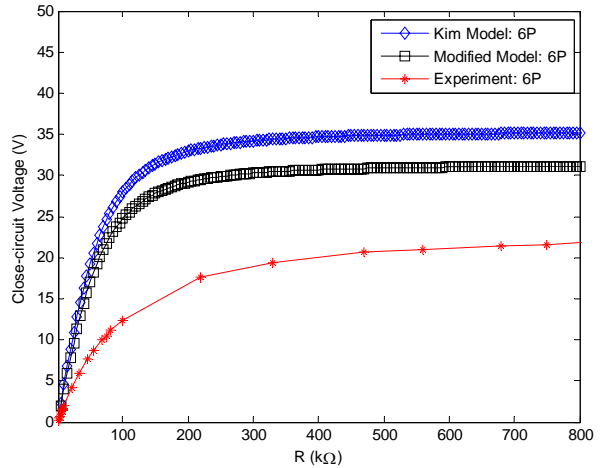
(c). 3 Proof Mass.



(d). 4 Proof Mass.



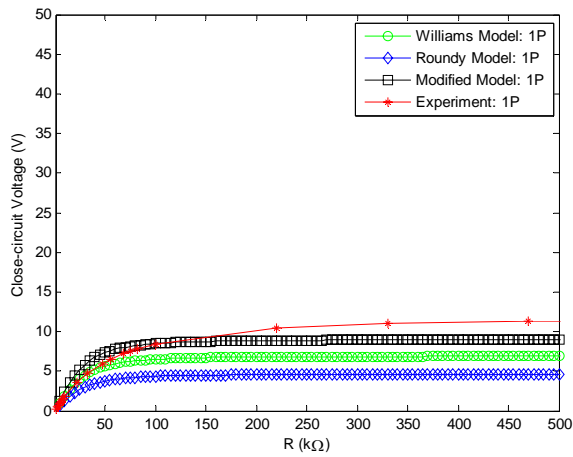
(e). 5 Proof Mass.



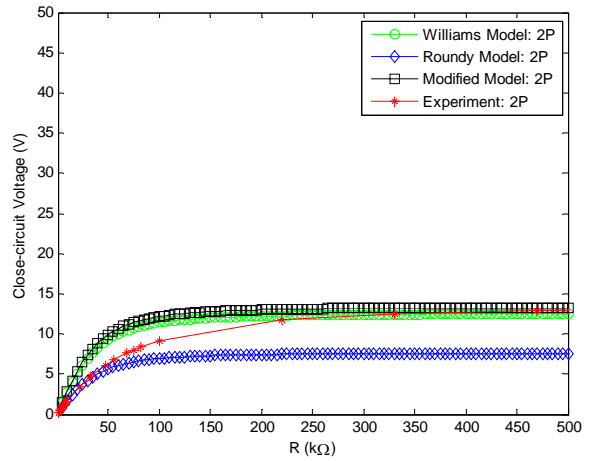
(f). 6 Proof Mass.

Figure 37. Close-circuit Voltage of Kim, Johnson, & Clark's Model and the Modified Model.

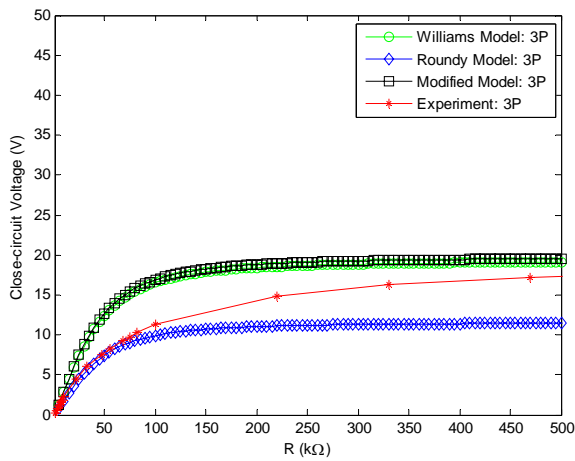
In Figure 38, the closed-circuit voltage of the modified model is again compared to the experimental data, along with the mechanical equivalent model of Williams and Yates' (1996) and Roundy's (2004) electrical equivalent model. It can be seen that the modified model and Williams' model better predict the closed-circuit voltage of the PCB generator with smaller amounts of proof mass, while Roundy's model provides a better prediction of the closed-circuit voltage at higher proof mass levels.



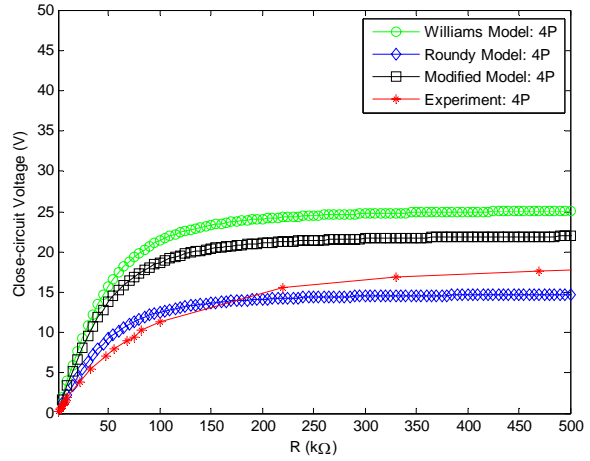
(a). 1 Proof Mass.



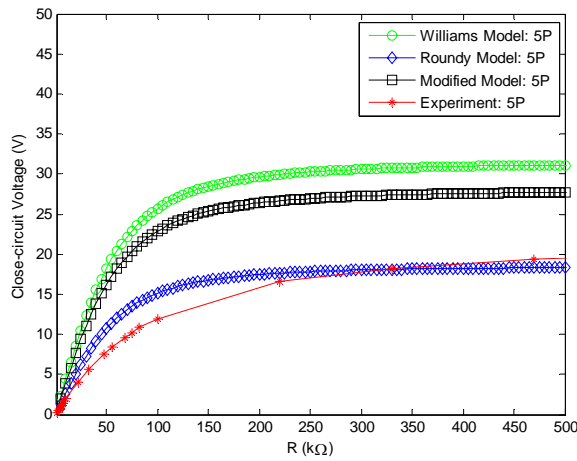
(b). 2 Proof Mass.



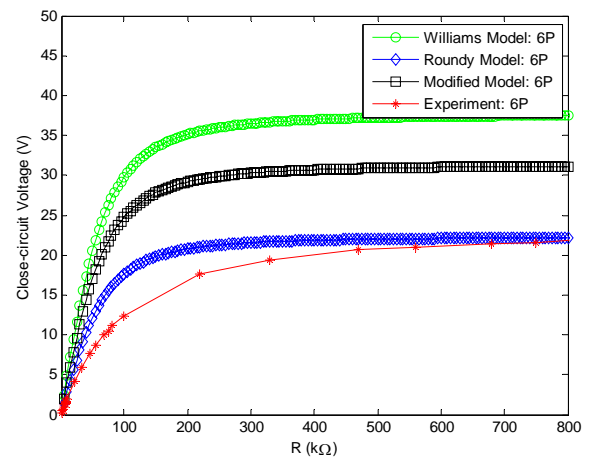
(c). 3 Proof Mass.



(d). 4 Proof Mass.



(e). 5 Proof Mass.



(f). 6 Proof Mass.

Figure 38. Close-circuit Voltage Comparison of Three Models.

## Power Output

The output power of the PCB generator can be calculated by the close-circuit peak-to-peak voltage presented in the last section:

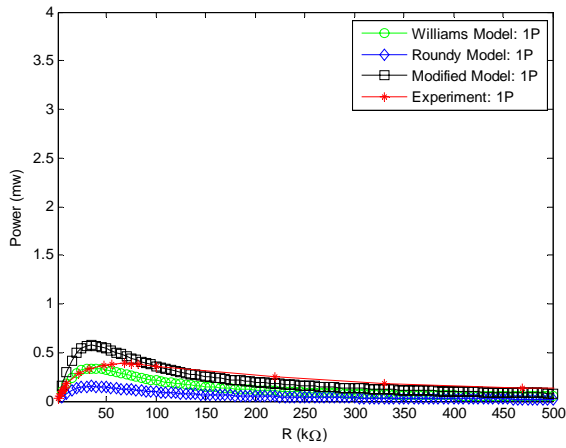
$$P = \frac{V_p^2}{2R}, \quad (4.38)$$

where  $V_p$  is the peak-to-peak value of closed-circuit voltage across the load and  $R$  is the load resistance. The results of Williams' mechanical equivalent model, Roundy's electrical equivalent model, and the modified model are compared against the experimental results, as is shown in Figure 39.

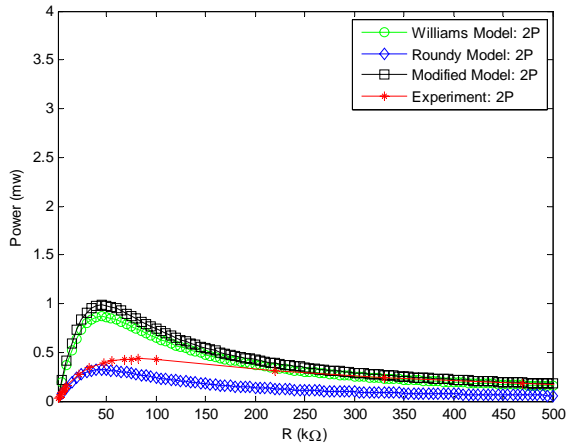
It can be seen that the power output of the PCB generator increases with the weight increase of the proof mass (from 1P to 6P). This is attributed to the larger structural deformations associated with larger proof masses. Further, the power results of the modified model are closer to the experiment for the PCB generator with less proof mass, while Roundy's model becomes much closer to the experiment for the PCB generator with more proof mass. In most cases, Williams and Yates' (1996) model has the worst prediction for the power output of the PCB generator.

The differences between the models' outputs and the experimental results are attributed to differences between the models and the actual device being tested. More specifically, error in the estimation of the PCB resonant frequency could result in a significant variation in the open- and closed-loop voltage calculations. Similarly, measurements of the tip displacement and damping ratio, geometric irregularities in the proof mass, and variations in the material properties of the piezoelectric bimorph would all cause errors in the voltage estimations. Such errors would be amplified when considering the power calculations, given the fact that the output power is a function of the square of the voltage. Despite the obvious differences, the models all still capture

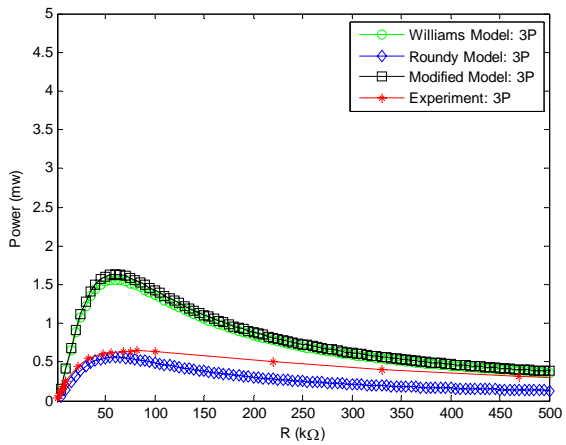
the general behavior of the PCB. In particular, the optimal resistor values of three models are very close to those of the experiment, as can be seen in the figures.



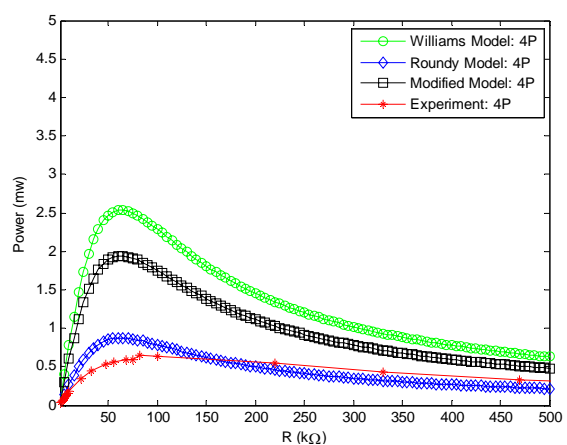
(a). 1 Proof Mass.



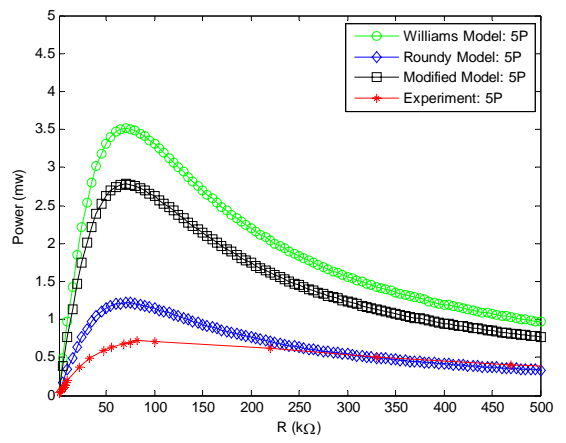
(b). 2 Proof Mass.



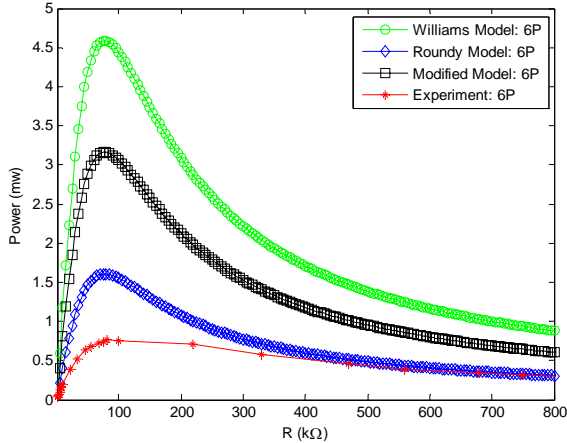
(c). 3 Proof Mass.



(d). 4 Proof Mass.



(e). 5 Proof Mass.



(f). 6 Proof Mass.

Figure 39. Power Output Comparison of Three Models.

## Summary

Building on the resonant frequency model of the PCB energy harvester described in the previous chapter, the voltage and power output models of the PCB generator were presented in this chapter. One modified analytical model based on a previous researcher's model was developed based on the assumption that the PZT parts of the piezoelectric bimorph under the proof mass generate negligible strain energy, and thus negligible electrical energy, since the piezoelectric effect of the PZT parts under the proof mass is greatly decreased due to the high rigidity of the proof mass. In addition, two PCB models available in the literature, i.e. the mechanical equivalent model and the electrical equivalent model, were also introduced. Following the model development, laboratory experiments were performed to provide experimental data against which to compare the different models. In examining the results, it can be seen that, when considering the two first-principles models, the modified model can better predict the open- and closed-circuit voltage of the PCB generator than the model presented by Kim, Johnson, and Clark (2004). Comparisons between the modified model, the mechanical equivalent model, and the electrical equivalent circuit model indicate that no single model is better at predicting the output of the PCB. For example, the modified model and the mechanical equivalent model of Williams and Yates (1996) both provide significantly better estimations of the PCB closed-circuit voltage at low proof-mass levels, but the electrical equivalent circuit model of Roundy (2004) is much better at predicting the voltage for higher proof mass levels. The significant differences in the power output estimated by the models and the actual power output measured experimentally is attributed to measurement errors in the resonant frequency, tip displacement, damping ratio, and potential errors in estimating the material properties of the piezoelectric bimorph. In spite of the model errors, it is believed that the models can still be used

to provide rough designs for the geometry of a PCB generator to provide a desired power level. Among the different models, the electrical equivalent model of Roundy appears to provide the closest approximation to the actual power output of the PCB. In addition, it has the advantage of an explicit expression in terms of simple parameters. As such, that will be used as the fitness function for the design optimization of a PCB generator that will be described in Chapter 6.

## CHAPTER 5

### FINITE ELEMENT ANALYSIS FOR THE DYNAMIC RESPONSES OF PCB GENERATOR

Compared with the traditional analytical modeling of a PCB generator, finite element analysis (FEA) is a more tractable approach to predicting the dynamic response of the generator, especially for devices with complicated geometric configurations. Further, for the design of MEMS-scale piezoelectric energy harvesters, the prototype fabrication and laboratory testing generates big challenges and difficulties during the process. In this section, based on the work given in Zhang and Williams (2010B), the use of FEA to study the dynamic response of a PCB generator subjected to a harmonic excitation is presented. The FEA simulation was performed using ANSYS® Multiphysics and Workbench and is compared against experimental results, in terms of both the PCB tip displacement and the induced electrical potential of the PCB generator. It is shown that FEA of piezoelectric devices in ANSYS® is a feasible way to simulate the practical laboratory testing and should therefore be a suitable tool for the design of PCB energy harvesters.

#### **Piezoelectric Analysis in ANSYS®**

The linear constitutive equation for the piezoelectric materials can be expressed as follows, according to Roundy (2004):

$$\{S\} = [s^E]\{T\} + [d]^t\{E\} \quad (5.1)$$

$$\{D\} = [d]\{T\} + [\varepsilon^T]\{E\} \quad (5.2)$$

where  $\{S\}$  and  $\{T\}$  are the strain and stress vectors, respectively (six components  $x, y, z, yz, xz, xy$ );  $\{D\}$  and  $\{E\}$  are the electric displacement vector and electric field vector, respectively (three components  $x, y, z$ );  $[s^E]$  is the six by six compliance matrix evaluated at constant electric field, i.e. short circuit;  $[d]$  is the three by six piezoelectric coefficient matrix relating strain and electric field;  $[d]^t$  is its transposed matrix; and  $[\varepsilon^T]$  is the three by three dielectric matrix evaluated at constant stress. In addition, the superscript  $E$  represents the data measured under constant electric field, i.e. PZT electrodes under short-circuit condition, and the superscript  $T$  represents the data measured under constant stress.

As mentioned previously, piezoelectric material exhibits strong electro-mechanical energy. Consequently, FEA of such a device requires the use of a multi-physics package such as ANSYS® Multiphysics. Since different manufactures of piezoelectric materials might provide different data formats, such as strain coefficient  $[d]$  vs. stress coefficient  $[e]$ , it is very important to input the correct data format, which is consistent with the ANSYS® APDL command. The conversions between the common piezoelectric data formats can be shown as follows:

$$[c] = [s^E]^{-1} \quad (5.3)$$

$$[e] = [c][d] \quad (5.4)$$

$$[\varepsilon^S] = [\varepsilon^T] - [e]^t [d] \quad (5.5)$$

where  $[c]$  is the elasticity matrix evaluated at a constant electric field;  $[e]$  is the piezoelectric stress matrix relating the piezoelectric stress and the corresponding electric field; and  $[\varepsilon^S]$  is the dielectric matrix evaluated at constant strain. For orthotropic materials, the flexibility or compliance matrix  $[s]$  and piezoelectric strain matrix  $[d]$  can be expressed as:

$$[s] = \begin{bmatrix} \frac{1}{E_x} & -\frac{\nu_{xy}}{E_x} & -\frac{\nu_{xz}}{E_x} & 0 & 0 & 0 \\ -\frac{\nu_{yx}}{E_y} & \frac{1}{E_y} & -\frac{\nu_{yz}}{E_y} & 0 & 0 & 0 \\ -\frac{\nu_{zx}}{E_z} & -\frac{\nu_{zy}}{E_z} & \frac{1}{E_z} & 0 & 0 & 0 \\ 0 & 0 & 0 & \frac{1}{G_{xy}} & 0 & 0 \\ 0 & 0 & 0 & 0 & \frac{1}{G_{yz}} & 0 \\ 0 & 0 & 0 & 0 & 0 & \frac{1}{G_{xz}} \end{bmatrix}, \quad [d] = \begin{bmatrix} 0 & 0 & d_{31} \\ 0 & 0 & d_{31} \\ 0 & 0 & d_{33} \\ 0 & 0 & 0 \\ 0 & d_{15} & 0 \\ d_{15} & 0 & 0 \end{bmatrix},$$

where  $E_x$  is the Young's modulus in the  $x$  direction;  $\nu_{xy}$  and  $\nu_{yx}$  are the major and minor Poisson ratios, respectively; and  $G_{xy}$  is the shear modulus in the  $xy$  plane. The compliance matrix  $[s]$  is symmetric so that  $\nu_{yx}/E_y = \nu_{xy}/E_x$ ,  $\nu_{zx}/E_z = \nu_{xz}/E_x$  and  $\nu_{zy}/E_z = \nu_{yz}/E_y$ . In addition, the above matrices assume that the piezoelectric material is poled in the  $z$  direction. Therefore, if the piezoelectric finite element model implemented in ANSYS® is poled in the  $y$  direction, another conversion changing the piezoelectric material properties in  $y$  direction with those in  $z$  direction correspondingly is also needed prior to performing analysis.

The finite elements in ANSYS® that can be used to model the piezoelectric devices include SOLID5, PLANE13, SOLID98, PLANE223, SOLID226, and SOLID227, and the specific descriptions of these elements can be found in the ANSYS® theory manual (2005).

Further, applying the variational principle and discretization of the finite elements of the piezoelectric system, the coupled finite element matrix equation is expressed as follows:

$$\begin{bmatrix} [M] & [0] \\ [0] & [0] \end{bmatrix} \begin{Bmatrix} \{\ddot{u}\} \\ \{\ddot{V}\} \end{Bmatrix} + \begin{bmatrix} [C] & [0] \\ [0] & [0] \end{bmatrix} \begin{Bmatrix} \{\dot{u}\} \\ \{\dot{V}\} \end{Bmatrix} + \begin{bmatrix} [K] & [K^z] \\ [K^z]^T & [K^d] \end{bmatrix} \begin{Bmatrix} \{u\} \\ \{V\} \end{Bmatrix} = \begin{Bmatrix} \{F\} \\ \{L\} \end{Bmatrix} \quad (5.6)$$

where  $\{u\}$  is the nodal displacement vector;  $\{V\}$  is the nodal electrical potential vector;  $[M]$  and

$[C]$  are the mass matrix and the structural damping matrix;  $[K]$ ,  $[K^z]$ , and  $[K^d]$  are the mechanical stiffness matrix, the piezoelectric stiffness matrix, and the dielectric stiffness matrix, respectively; and  $[F]$  and  $[L]$  are the force vector and the charge vector, respectively.

### **FEA and Experimental Validation**

In this section, finite element analysis of a PCB generator subjected to harmonic excitation is performed using ANSYS®. Two outputs are obtained: tip displacement and electrical potential generation, also referred to as open-circuit voltage. Laboratory harmonic testing was also performed to provide data against which the FEA results could be compared. In addition, the previously presented tip displacement model is also compared against the FEA and experimental data.

The generator prototype is composed of a Q220-A4-203Y PZT bimorph, whose dimensions and material properties were shown in Table 2 and Table 3 in Chapter 3. The piezoelectric matrices used for the ANSYS® simulation are calculated with Equations 5.3 – 5.5. In addition, since the solid model of the PCB generator created in ANSYS® is poled in  $y$  axis direction, which is different from the common  $z$  axis polarization, the corresponding conversions must be performed according to the ANSYS® manual. The final piezoelectric matrices used for ANSYS® simulations are shown as follows:

$$\text{Compliance Matrix } [s]: 10^{-12} m^2 / N \quad \begin{bmatrix} 15.2 & 4.70 & 5.96 & 0 & 0 & 0 \\ 4.70 & 15.2 & 5.96 & 0 & 0 & 0 \\ 5.96 & 5.96 & 1.92 & 0 & 0 & 0 \\ 0 & 0 & 0 & 3.97 & 0 & 0 \\ 0 & 0 & 0 & 0 & 5.04 & 0 \\ 0 & 0 & 0 & 0 & 0 & 5.04 \end{bmatrix}$$

$$\text{Relative Dielectric Matrix } [\varepsilon^T]: \quad \begin{bmatrix} 1800 & 0 & 0 \\ 0 & 1800 & 0 \\ 0 & 0 & 1800 \end{bmatrix}$$

$$\text{Piezoelectric Strain Matrix } [d] 10^{-12} m / V \quad \begin{bmatrix} 0 & -190 & 0 \\ 0 & 390 & 0 \\ 0 & -190 & 0 \\ 600 & 0 & 0 \\ 0 & 0 & 600 \\ 0 & 0 & 0 \end{bmatrix} \cdot$$

In order to reduce the number of finite elements and to increase FEA calculation efficiency, the mounting plate that the PCB generator prototype is clamped to can be simplified as a large mass point with rigid rods connecting to the clamped end of the cantilevered structure, based on the Large Mass Method (LMM), as discussed by David (2000) and Lu, Wang, and Ai (2002). The finite element distribution of the PCB generator in the ANSYS® simulation is shown in Figure 40 where: the large mass point on the left end is modeled using point element MASS21 with 6 degrees of freedom (DOF) and 10 Kg mass; the connecting rod is modeled using a 2-node truss element LINK8 with 3 DOF's; the PZT layers are modeled using 8-node coupled-field element SOLID5 with 4 DOF's in  $U_x$ ,  $U_y$ ,  $U_z$ , and Volt; and the central brass layer and the proof mass are modeled using 8-node structural element SOLID45 with 3 DOF's.

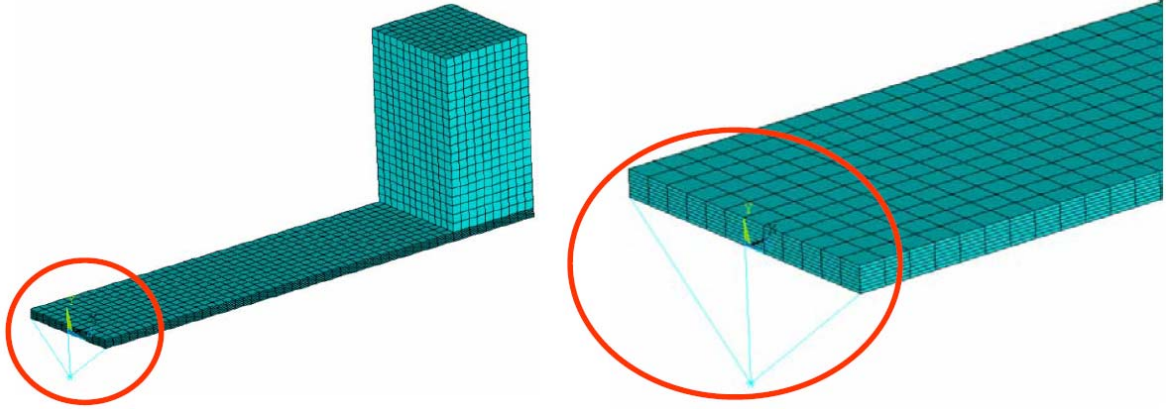


Figure 40. Finite Element Distribution of PCB Generator.

The laboratory testing setup of the prototype is identical to that used in the testing of the resonant frequency and the power output, as is shown in Figure 19, where 6 proof mass blocks were sequentially added to the tip of the PZT bimorph. The harmonic excitation with the amplitude of  $11.2 \text{ m/s}^2$  in the frequency range of  $0 \sim 300 \text{ Hz}$  is input to the shaker. The tip displacement of the PCB generator was measured using a laser vibrometer, and the electrical potential was measured using MATLAB XPC Target, as was shown in Figure 31.

### Tip Displacement

The single degree-of-freedom (SDOF) generator was presented in Chapter 3, where the system transfer function can be further derived to obtain the tip displacement of the PCB generator subjected to harmonic excitations as follows:

$$|\bar{z}| = \frac{A_{in}}{\omega^2} \sqrt{\frac{\omega_n^4 + (2\zeta\omega\omega_n)^2}{(\omega^2 - \omega_n^2)^2 + (2\zeta\omega\omega_n)^2}} \quad (5.7)$$

$$\phi = \tan^{-1}\left(2\zeta \frac{\omega}{\omega_n}\right) - \tan^{-1}\left(\frac{2\zeta\omega_n\omega}{\omega_n^2 - \omega^2}\right) \quad (5.8)$$

where  $|\bar{z}|$  is the amplitude of the tip displacement,  $\phi$  is the phase difference between the input

vibration and the tip displacement,  $\zeta$  is the damping ratio,  $\omega_n$  is the resonant frequency of the device,  $\omega$  and  $A_{in}$  are the driving frequency and the acceleration amplitude of the input vibration, respectively. In addition, the resonant frequency can be calculated using the definition of  $\omega_n = \sqrt{K / M}$ , as described in Chapter 3:

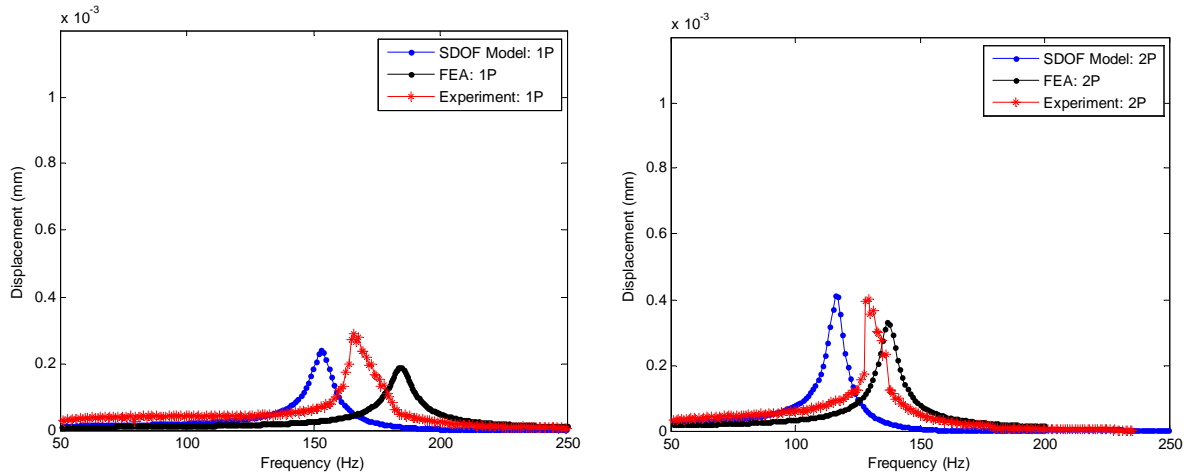
$$K = \frac{Dw}{4L^3} c_{sh} c_p \quad (5.9)$$

$$M = \frac{33}{140} M_{bimorph} + M_{proofmass} \quad (5.10)$$

where  $D = \frac{2(3t_{sh}^2 t_p + 6t_{sh} t_p^2 + 4t_p^3)}{c_{sh}} + \frac{t_{sh}^3}{c_p}$ ,  $M_{bimorph}$  and  $M_{proofmass}$  are the mass of the PZT

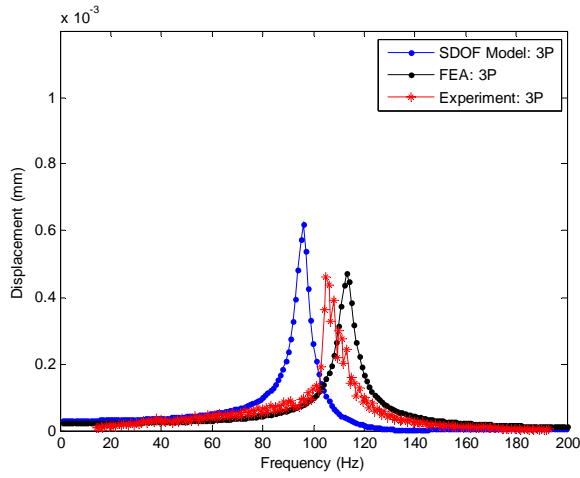
bimorph and the proof mass, respectively, and the other parameters are the geometric dimensions and mechanical properties consistent with those described in previous chapters.

The measured tip displacement of the prototype under harmonic excitation is shown in Figure 41, along with the tip displacements calculated by the SDOF model and the FEA.

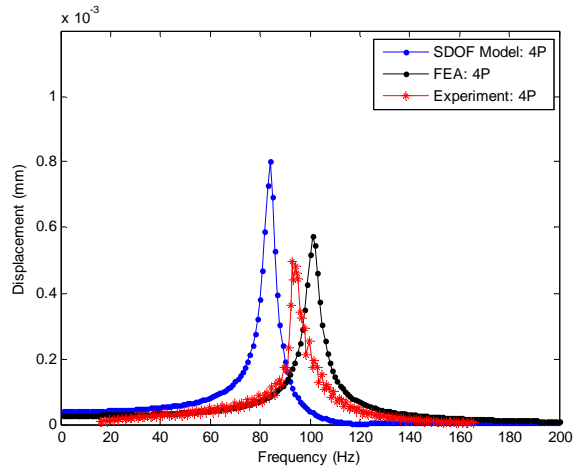


(a). 1 Proof Mass.

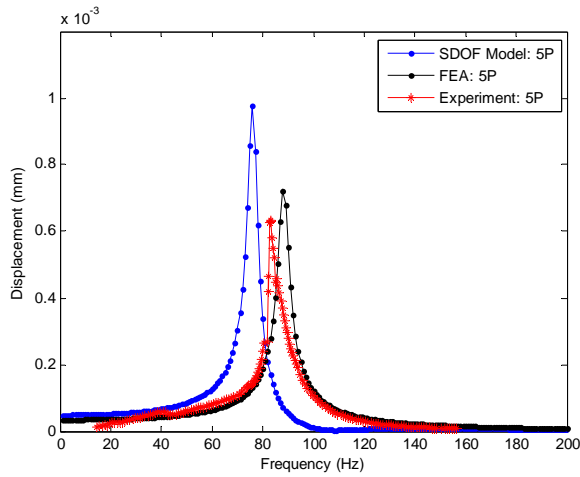
(b). 2 Proof Mass.



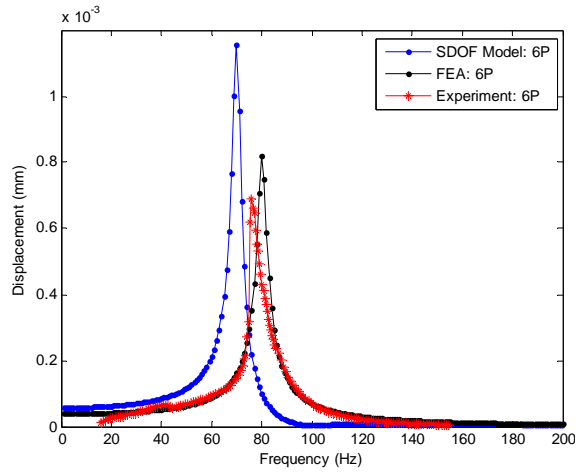
(c). 3 Proof Mass.



(d). 4 Proof Mass.



(e). 5 Proof Mass.



(f). 6 Proof Mass.

Figure 41. Harmonic Responses of the Prototype Tip Displacement.

In the above figure,  $nP$  represents  $n$  pieces of proof mass currently added to the tip of the PZT bimorph. In examining the results shown in Figure 41, it can be seen that the peak value of the tip displacement increases with the increasing proof mass. Further, while the FEA results over-predict the actual resonant frequency of the PCB at low proof mass levels, for most of the tests, the FEA and the experimental results match quite well. Therefore, the FEA is considered to be a valid representation of the tip displacement of the PCB and can be used in the modified model

presented in Chapter 4 to predict the voltage and power output of the PCB generator.

### Open-Circuit Voltage

The harmonic response of the open-circuit voltage collected by the data acquisition system is the time-domain signal, as is shown in Figure 42, where 3P represents the PCB generator with 3 proof mass blocks. Fast Fourier Transform (FFT) code from the software package MATLAB can be used to obtain the frequency response of the harmonic testing. Finite element harmonic analysis of the PCB generator is performed in the range of  $0 \sim 2000 \text{ Hz}$ ; one example of the open-circuit voltage response is shown in Figure 43, where there are two peaks corresponding to the first two bending modes of the PCB generator.

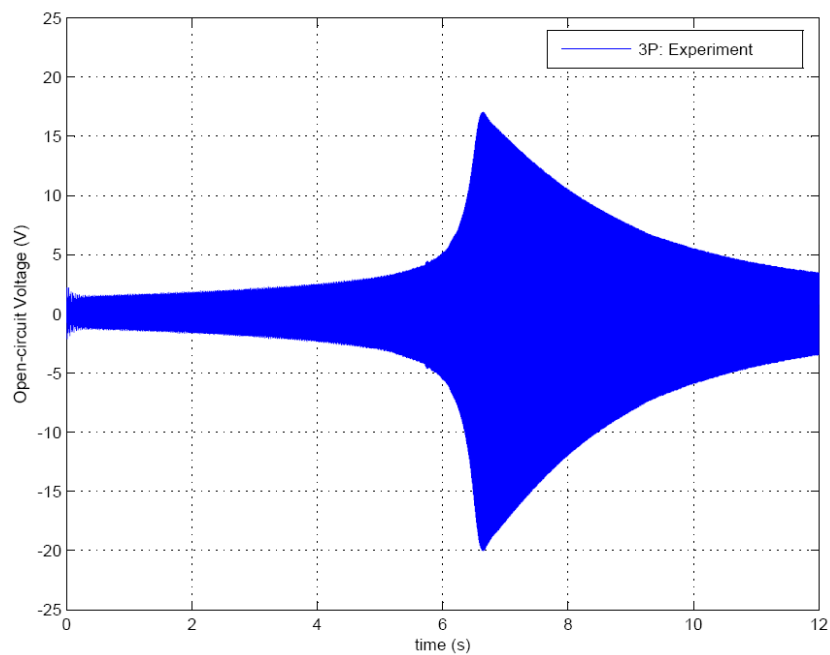


Figure 42. Experimental Harmonic Response of Open-circuit Voltage.

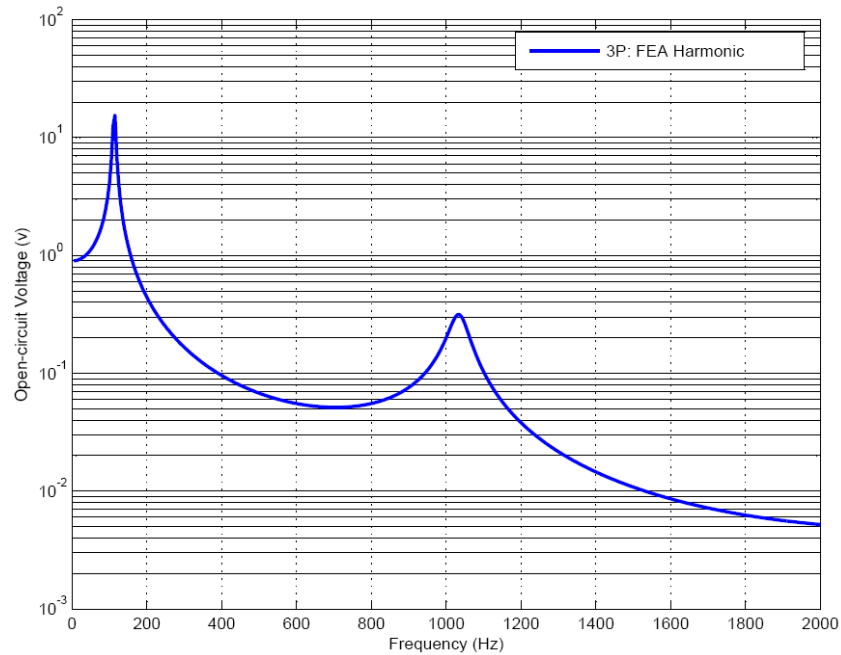
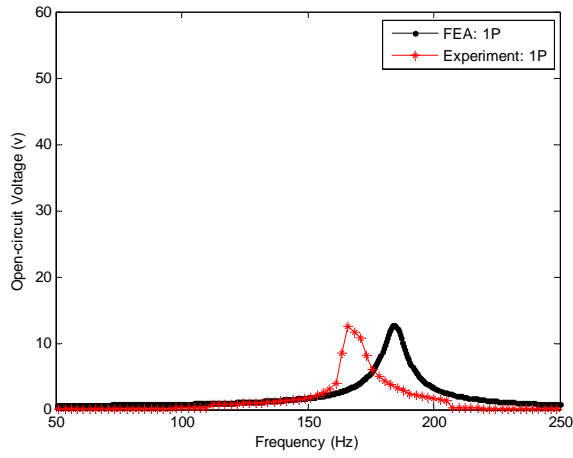
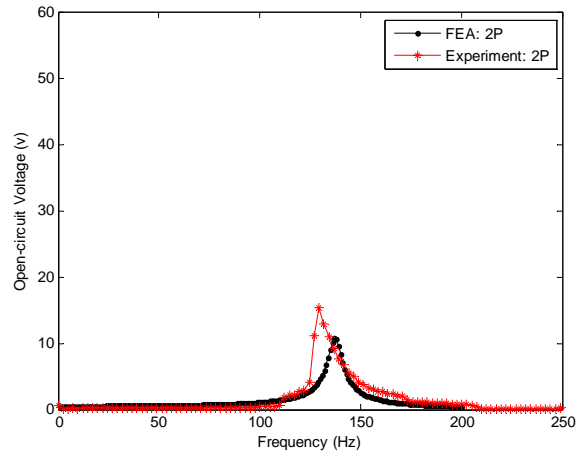


Figure 43. Finite Element Harmonic Analysis of PCB Generator in 0 ~ 2000 Hz.

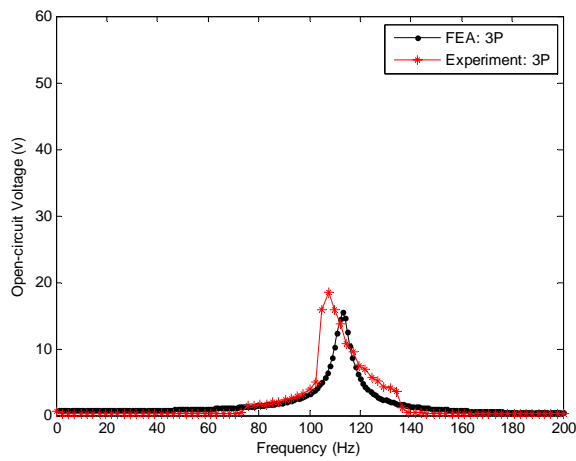
The open-circuit voltage comparison between FEA and experiment for the PCB generator with 6 different proof mass blocks is shown in Figure 44. As expected, it is clear that the peak value of the open-circuit voltage increases with increasing proof mass. Further, it can be seen that, with the exception of the single proof mass test, the FEA results are quite close to the experimental data in terms of both the peak amplitude of the open-circuit voltage and the frequency at which it occurs. Therefore, FEA of PZT dynamic responses is a feasible and convenient way to study and design piezoelectric energy harvesters with more complicated configurations. Similarly, the bias may be attributed to the geometric irregularity of the proof mass, the bonding effectiveness of the super glue, and the material property bias of the PZT bimorph used for FEA simulation.



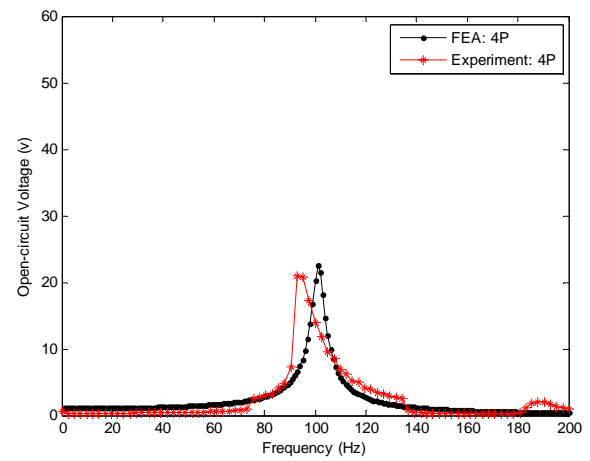
(a). 1 Proof Mass.



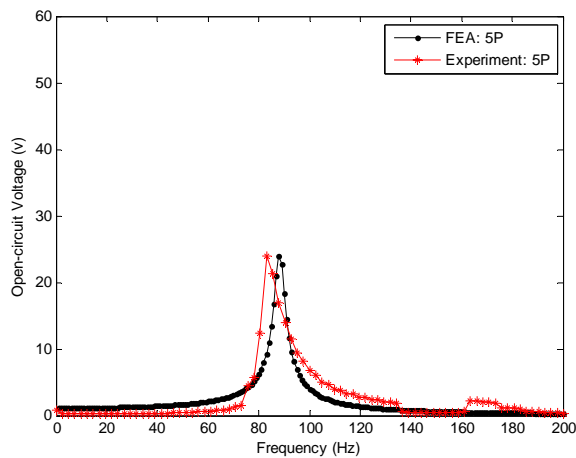
(b). 2 Proof Mass.



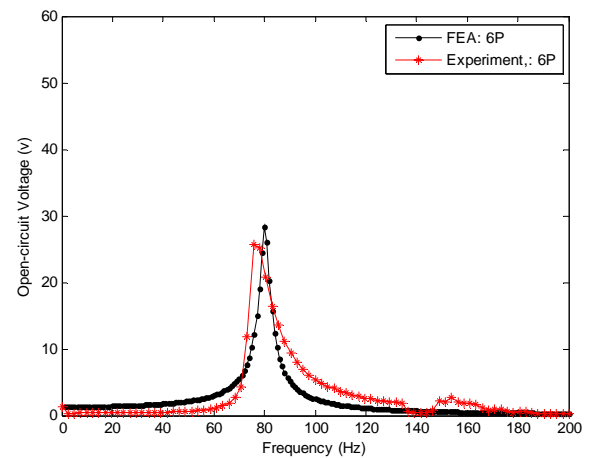
(c). 3 Proof Mass.



(d). 4 Proof Mass.



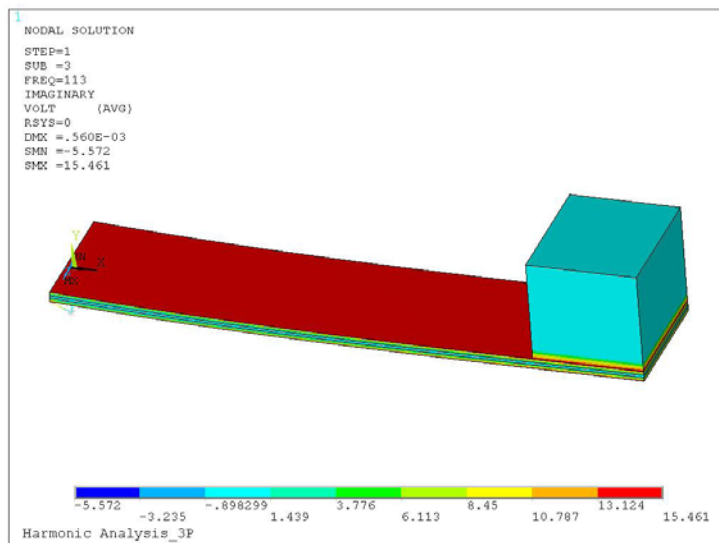
(e). 5 Proof Mass.



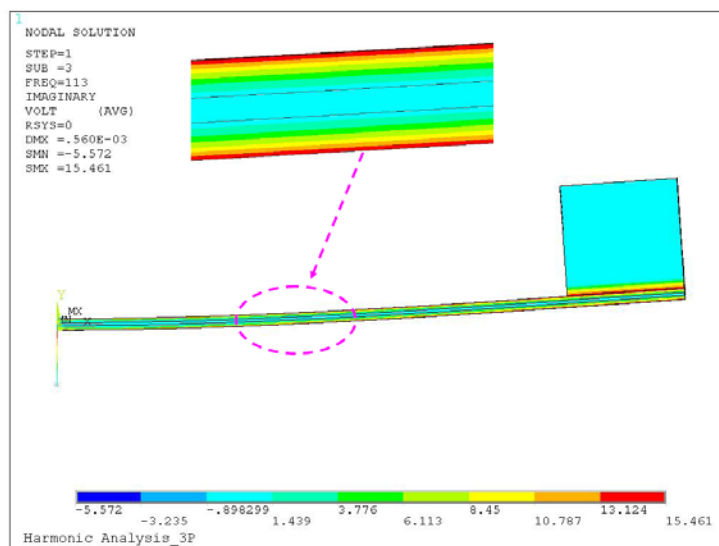
(f). 6 Proof Mass.

Figure 44. Harmonic Responses of the Prototype Open-circuit Voltage.

The electrical potential distribution across the PCB bimorph with 3 proof mass blocks is shown in Figure 45, where the top and bottom surfaces have the highest identical electrical potentials, since the two PZT layers are poled in the opposite direction along the y axis and the top and bottom electrodes are coupled together, while the central brass layer is grounded with 0 volts.



(a) ISO View



(b) Front View and Magnified Part.

Figure 45. Electrical Potential Distribution of the Piezoelectric Bimorph.

## Summary

In this chapter, finite element analysis (FEA) carried out to study the dynamic response of the PCB generator subjected to harmonic excitations was presented. Results for the two research objectives of predicting tip displacement and open-circuit voltage were obtained and compared to experimental results. For the tip displacement study, a previous single degree of freedom (SDOF) model for the tip displacement of the PCB generator presented in Chapter 3 was modified, and results from that model were compared against those obtained from the FEA and from the experiment. It was shown that the FEA can better predict the PCB response than the SDOF model in terms of both the peak amplitude of the tip-response and the resonant frequency of the PCB, and thus it can be used in the modified model for the prediction of the voltage and power output of the PCB generator presented in Chapter 4. For the electrical potential analysis, the results of FEA are also close to the experimental measurements, in terms of both the peak value of the open circuit voltage and the frequency at which it occurred. The relatively small errors that still exist between the FEA results and the experimental data are attributed to the geometric irregularity of the proof mass, the bonding effectiveness of the super glue, and the material properties used for the ANSYS® simulation. In addition, the FEA electrical potential distribution of the piezoelectric bimorph shows that the top and bottom have the highest identical voltage, which explains the 31 working mode of the piezoelectric benders to some extent, i.e., the strain is generated along  $x$  axis (1 direction), while the electrical potential is generated along the transverse direction (3 direction). To summarize, it has been demonstrated that an FEA should be useful as a tool for the design of a PCB energy harvester.

## CHAPTER 6

### DESIGN OPTIMIZATION OF PCB GENERATOR

Parameter optimization plays an important role in structural design, particularly when dealing with a lightly damped system such as a PCB energy harvester. With the basic design concept of the PCB energy harvester defined, and analytical models to predict the resonant frequency and the voltage and power output presented in the former chapters, the final element of this research effort is an examination of design optimization of the device. Based on the work presented in Zhang and Williams (2010C), three design optimization approaches are presented in this chapter, including design optimization of a single PCB generator using a genetic algorithm (GA), band-pass design optimization of PCB generators, and design optimization of the PCB generator with new geometric features. The goal of this chapter is to present some general approaches for design optimization of the PCB energy harvester, thus contributing to the ultimate goal of a PCB energy harvester that can provide power for completely self-powered portable electronics or wireless sensor networks.

#### **Genetic Algorithm Optimization of a Single PCB Generator**

As a search technique, a GA was first proposed by Holland (1975), who brought forward the notion that optimized solutions for an equation can be approached by iteratively combining an initial pool of solutions and varying successive iterations in a fashion similar to the process of “genetic evolution.” Principally, there are two different evolving processes, unconstrained evolution and evolution within specified boundary conditions. The latter approach ensures that

the end solution will fit within imposed optimization constraints. The evolution of a GA starts with a randomly selected population and evolves over generations. A basic evolution procedure of a GA obtained from Xie (2008) is shown in Figure 46, where a parent generation evolves to a new generation via the three basic steps of selection, cross-over, and mutation. The new generation then becomes the next parent generation and continues the evolution process.

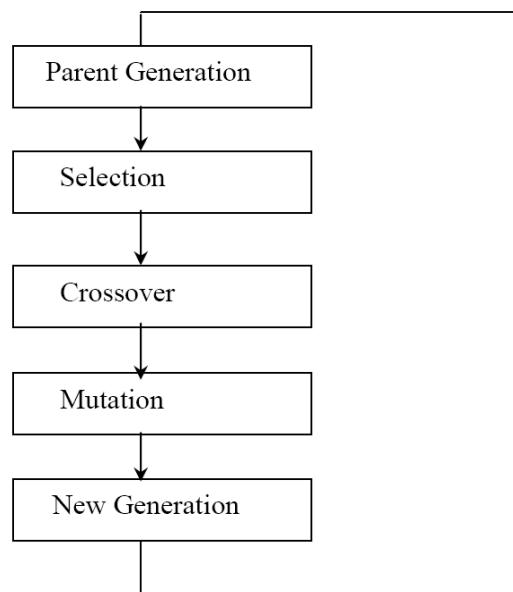


Figure 46. Basic Procedure for Genetic Algorithm (Xie, 2008).

A given generation is usually represented as a genome, a chromosome sequence, or a digital bit string. From that population, a parent population will be selected based on those members of the population with higher fitness values. A common approach to selection is to use what is known as a roulette wheel selection scheme, in which a sequence or a bit string with a higher fitness will be allocated to a larger part of the wheel and thus will be more easily selected. Mathematically, the fitness value is the calculated result of a theoretical model. For example, in the selection of characteristics of a PCB energy harvester, for a given parameter, a value that results in a higher open-circuit voltage will be allocated a larger percentage of the “roulette

wheel” than a different value of the same parameter. The new “parent” parameter will then be selected at random from among those finite values listed on the “roulette wheel.” In the random selection process, therefore, the parameter value resulting in a higher open-circuit voltage has a higher probability of being selected than one that does not. However, there is still some chance that the parameter value resulting in a lower open-circuit voltage will be selected, in spite of the lower probability of such an occurrence. Crossover involves the exchange of a finite sub-set of the bits of one parent for the similar sub-set of bits in the other parent and vice versa. Mutation involves the random alternation of a bit in the digital string that is the genetic code of a parent. It is noted that the mutation rate should be controlled appropriately; otherwise, the genetic information will be lost quickly.

In this section, the geometric parameters of a single PCB generator are optimized using a GA implemented in the software MATLAB. Due to its explicit expression, the power output model shown in Equation 4.16, developed by Roundy (2004), rather than the modified model presented in Chapter 4, is used as the fitness function, since the modified model for the PCB generator requires the measurement of the resonant frequency and the tip displacement of the device to calculate the force of the proof mass acting on the bimorph. The parameters to be optimized are shown in Table 6, where the representations are consistent with those used in the former chapters.

In his work, Roundy (2003B) measured the ambient vibrations of common appliances and found that most such vibrations occur at 120 Hz. Measured appliances included a kitchen blender, a clothes dryer, a microwave oven, a bread maker, and a washing machine. In light of those measurements, and having demonstrated in a former chapter that the power output of a PCB generator is maximized when the device is excited at its fundamental resonant frequency,

during design optimization, the resonant frequency of the PCB energy harvester is constrained to be 120 Hz, which is accomplished using Equation 3.6 of the frequency model of Dong, Meng, and Peng (2006) presented in Chapter 3. In addition, with the ultimate goal of using a PCB energy harvester as the main power source for MEMS and wireless sensor networks, the total volume of the generator should be small and is thus constrained to fit with a volume of less than  $1 \text{ cm}^3$  in this GA optimization. Further, the geometric parameters should have practical meaning (i.e.  $> 0$ ). The formulation of the optimization problem is shown in Figure 47.

Table 6

Design Variables for Optimization

Variables	Description
$L$	Length of the PZT cantilever bimorph
$w$	Width of the PZT cantilever bimorph*
$t_p$	Thickness of the single piezoelectric layer
$t_{sh}$	Thickness of the central brass layer
$l_m$	Length of the proof mass
$h_m$	Height of the proof mass
$R_{load}$	Load Resistance

\* The width of the proof mass is always identical with that of the bimorph during optimization.

$$\text{Fitness Function: } Power = \frac{1}{2\omega_n^2} \frac{RC_b^2 (2c_p d_{31} t_p)^2 / (k_2 a \epsilon)^2 A_m^2}{(4\zeta^2 + k_{31}^4)(RC_b \omega_n)^2 + 4\zeta k_{31}^2 (RC_b \omega_n) + 4\zeta^2}$$

$$\text{Boundary Conditions: } f_n(L, w, t_p, t_{sh}, l_m, h_m) \approx 120 \text{ Hz}$$

$$Lw(2t_p + t_{sh}) + l_m w_m h_m \leq 1 \text{ cm}^3$$

$$L - l_m > 0$$

$$L, w, t_p, t_{sh}, l_m, w_m, h_m, R > 0$$

Figure 47. Formulation of Optimization Problem.

Other parameters, such as the bender capacitance and the proof mass size, are determined by the design variables with the following assumptions. First, PZT-A4, identical with the piezoelectric material used for the laboratory experiment presented in Chapters 3 and 4, is selected as the piezoelectric material with the corresponding mechanical and piezoelectric properties held fixed for the optimization. Second, brass is adopted as the proof mass material with a density of  $8800 \text{ Kg} / \text{m}^3$ . Third, base excitation with an amplitude of  $11 \text{ m} / \text{s}^2$  is used as the excitation. The reason for selecting the fixed vibration characteristics is that the goal is to optimize the design parameters of the PCB energy harvester, rather than optimize the exterior environment parameters, such as the vibration frequency and amplitude. However, the optimization routine could be repeated for any particular vibration input magnitude and frequency and would potentially yield different optimized design parameters.

The optimization problem detailed above was solved using a GA, and the resulting design parameters and predicted open-circuit voltage and power output are shown in Table 7, where an open-circuit voltage of  $32.36 \text{ V}$  and a power output of  $7.84 \text{ mW}$  can be obtained for a PCB generator with a total volume of  $1.02 \text{ cm}^3$ , and the resonant frequency is about  $120 \text{ Hz}$ . This

optimal design assumes that a PZT bimorph with any thickness could be purchased. However, most PZT manufactures or distributors only provide a limited number of discrete PZT thicknesses. For instance, Piezo System, Inc., the PZT supplier of the Q220-A4-203Y used in previous experiments, only provides PZT thicknesses of 0.139 *mm* , 0.191 *mm* , and 0.278 *mm* . Another limitation is that the fitness function defined by Equation 4.16 of Roundy's (2004) power output model, and the resonant frequency boundary condition defined by Equation 3.6 of Dong, Meng, and Peng's (2006) frequency model, are based on Euler beam theory, in which the optimized length of the bimorph should be at least five times longer than its width. Any smaller length/width ratio would result in questionable applicability of Euler beam theory. The optimized design parameters and predicted output for a single PCB generator with three different specific PZT thicknesses are shown in Table 8.

Table 7

Optimized Design Parameters and Outputs for a Single PCB Generator.

Variables	Optimized Value
$L$	32.676 mm
$w$	8.519 mm
$t_p$	0.294 mm
$t_{sh}$	0.4171 mm
$l_m$	9.682 mm
$w_m$	8.519 mm
$h_m$	8.971 mm
$R_{load}$	8.97 k $\Omega$
$f_n$	119.0 Hz
<i>Volume</i>	1.02 cm <sup>3</sup>
$V_{open-circuit}$	32.36 V
$P_{out}$	7.84 mW

Table 8

Optimized Parameters and Outputs under Additional Constraints.

Variables	Optimized Values		
	$t_p = 0.139 \text{ mm}$	$t_p = 0.191 \text{ mm}$	$t_p = 0.278 \text{ mm}$
$L \text{ (mm)}$	36.085	45.702	44.416
$w \text{ (mm)}$	11.208	7.992	6.342
$t_{sh} \text{ (mm)}$	0.658	0.905	0.856
$l_m \text{ (mm)}$	8.552	10.745	11.126
$w_m \text{ (mm)}$	11.208	7.992	6.342
$h_m \text{ (mm)}$	6.694	6.354	8.723
$R_{load} \text{ (k}\Omega\text{)}$	16.80	9.05	20.19
$f_n \text{ (Hz)}$	119.0	119.0	119.0
$Volume \text{ (cm}^3\text{)}$	1.02	1.02	1.01
$V_{open-circuit} \text{ (V)}$	11.81	13.84	23.02
$P_{out} \text{ (mW)}$	2.47	3.13	4.42

A damping ratio of 0.021 is used for the above optimization, based on the measurements described in Chapter 4. The above results indicate that 4.42 mW can be achieved for a PCB generator with PZT thickness of 0.278 mm under a total volume of 1 cm<sup>3</sup>. As would be expected, with their thinner PZT layers, the other two designs have less predicted power output. In order to examine the feasibility of the above design optimizations, an FEA was performed. In Figures 48-50, the open-circuit voltage of the optimized PCB generator is calculated by Equation 4.15, using the optimized parameters in Table 8 and compared against the ANSYS® simulation.

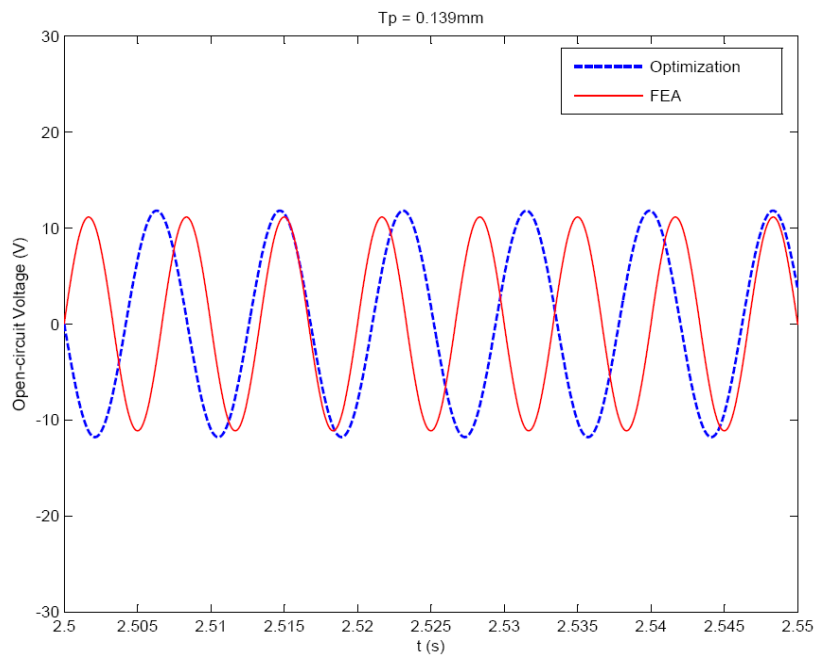


Figure 48. GA Optimization of PCB Generator with  $t_p = 0.139mm$ .

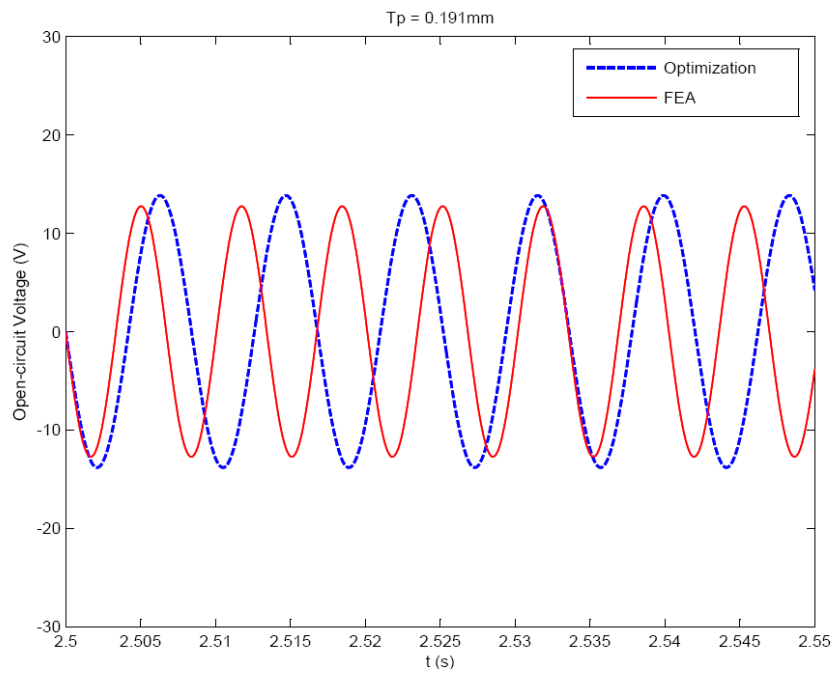


Figure 49. GA Optimization of PCB Generator with  $t_p = 0.191mm$ .

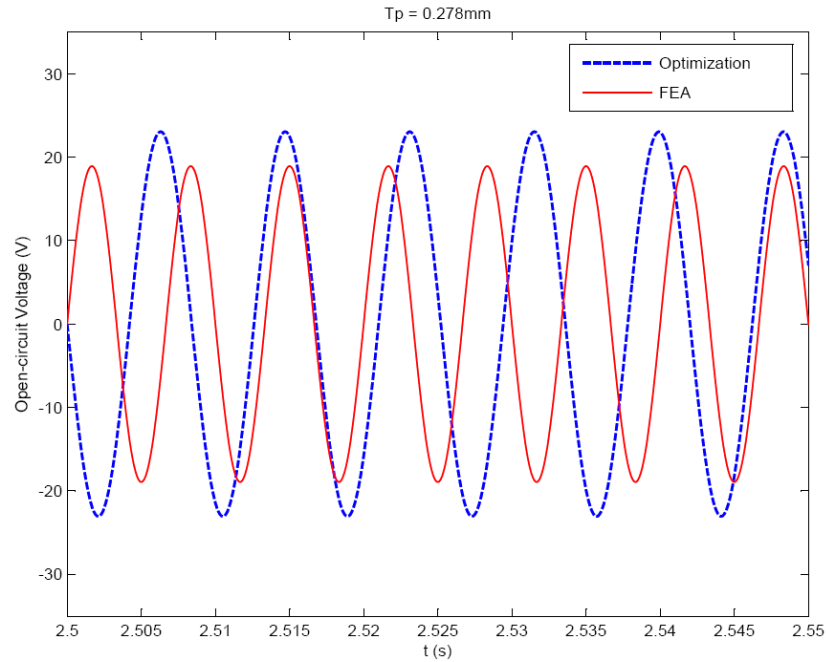


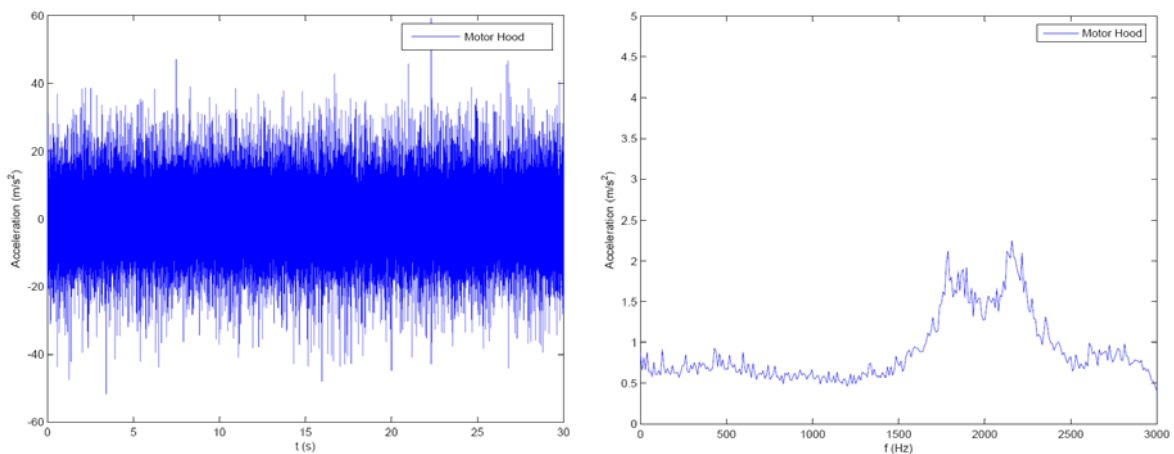
Figure 50. GA Optimization of PCB Generator with  $t_p = 0.278mm$ .

In examining Figures 48-50, it can be seen that the open-circuit voltage amplitudes of three optimization designs are close to the FEA results, although there is about 30 Hz frequency difference between GA optimization and FEA for each optimized design, which is attributed to the inaccuracy of the frequency model used as the boundary condition. Further, due to the bias between the power model and the experiment presented in Chapter 4, the practical power based on the geometry obtained from GA optimization can be less than those shown in Table 8.

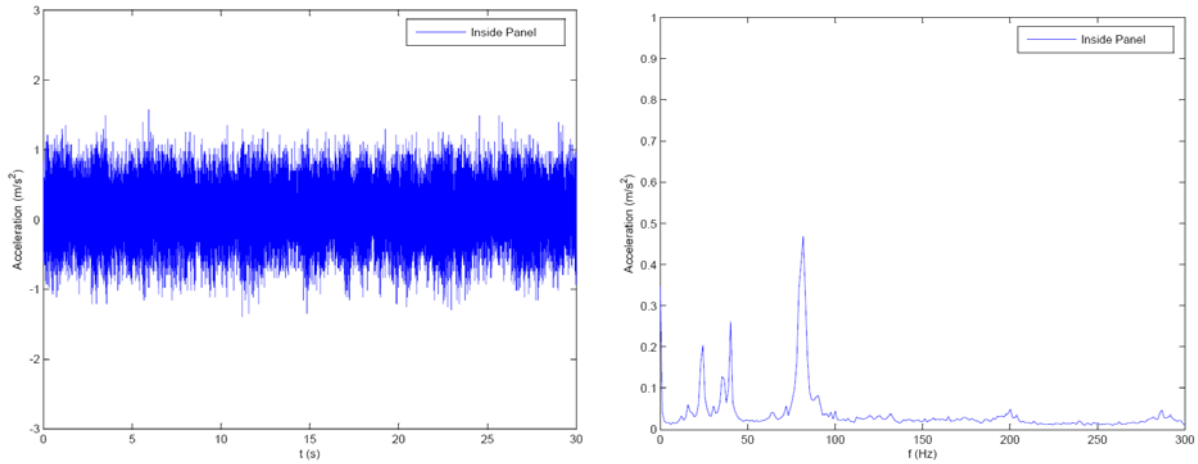
Assuming the fitness functions and constraint functions defined by the theoretical models are effective, optimization using a GA is a feasible and convenient method for nonlinear optimization of the PCB geometry. In practice, other design constraints may be required, such as the total length and weight, and the geometric configuration of the piezoelectric energy harvester. However, by using the combination of GA and FEA, the design optimization of piezoelectric energy harvesters can be explored and examined effectively.

## Band-pass Design Optimization of PCB Generators

The aforementioned optimization is performed for a single PCB generator working at its resonating frequency, which matches the frequency of the ambient vibration. However, in many situations, ambient vibration is not limited to a single frequency and may actually be spread over a band of frequencies. For example, the motor hood vibration and the panel vibration of an operating Chevrolet Malibu 2000 are measured and shown in Figure 51, where the left-hand sides of the figure are the vibration signals in the time domain, and the right-hand sides are the vibration signals' frequency response obtained through the use of the FFT. It can be seen that the motor hood vibration shows a relatively high frequency response over a frequency band of 1700  $Hz$  to 2200  $Hz$ , while the inside panel vibration reveals several frequency peak responses around 20  $Hz$ , 40  $Hz$ , and 85  $Hz$ . In either case, the vibration has a relatively large signal strength spread across bands of frequencies, rather than concentrated at a single frequency. Therefore, it is of benefit to consider the design of PCB energy harvesters that can be applied to work over a frequency band. Such a device is considered to be a band-pass PCB energy harvester.



(a). Motor Hood Vibration

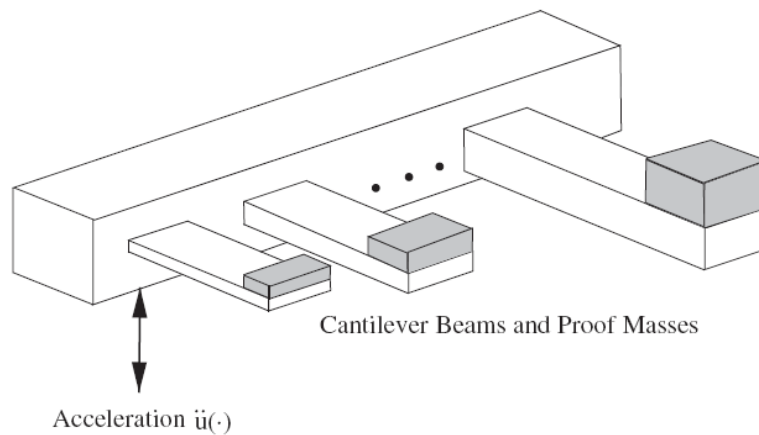


(b). Inside Panel Vibration.

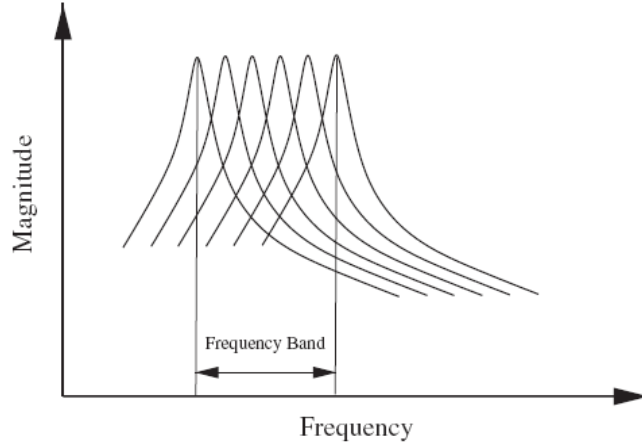
Figure 51. Ambient Vibrations from Motor Hood and Inside Panel.

### Band-pass Design of PCB Energy Harvesters

Shahruz (2006A, 2006B, & 2008) proposed the design of mechanical band-pass filters for energy scavenging, where the device consists of a group of piezoelectric cantilever beams, each with a tip-mounted proof mass, shown in Figure 52a. If the dimensions of the piezoelectric beams and masses of the proof mass are chosen appropriately, energy harvesting can be realized across a band of frequencies, as shown in Figure 52b.



(a). A Band-pass Filter Made of Cantilever Beams.



(b). Frequency Response of the Band-pass Filter.

Figure 52. A Band-pass Filter and Its Frequency Response, Shahruz (2005).

During Shahruz's theoretical derivation, however, the piezoelectric characteristics of the beams were not taken into consideration, and the piezoelectric beams were only treated as general elastic beams. In addition, the PZT beam under investigation was just a single PZT layer; the PZT bimorph generator was not covered. In this section, the band-pass piezoelectric energy harvester, using an ensemble of PCB generators, will be explored.

Due to its simplicity and explicit form, the aforementioned electrical equivalent model for the PCB generator developed by Roundy (2004) is used as the baseline model for the band-pass design derivation. Following Roundy's derivation, the closed-circuit voltage of a single PCB generator can be obtained as follows:

$$V(s)[s^3 + (\frac{1}{RC_b} + \frac{b_m}{m})s^2 + (\frac{k}{m}(1 + \frac{d_{31}^2 c_p}{\epsilon}) + \frac{b_m}{mRC_b})s + \frac{k}{mRC_b}] = \frac{2c_p d_{31} t_p}{k_2 a \epsilon} s A_m(s) \quad (6.1)$$

where the parameters have been described in Chapters 3 and 4. For the sake of convenience, they

are repeated briefly as follows:  $k_1 = \frac{b(2L_b + L_m - L_e)}{2I}$ ;  $k_2 = \frac{L_b^2(2L_b + \frac{3}{2}L_m)}{3b(2L_b + L_m - L_e)}$ ;

$I = 2\left[\frac{wt_p^3}{12} + wt_p b^2\right] + \frac{\eta_s wt_{sh}^3}{12}$  is the effective moment of inertia of the piezoelectric bimorph;

$\eta_s = c_{sh} / c_p$ ;  $b = (t_p + t_{sh}) / 2$ ;  $k = \frac{c_p}{k_1 k_2}$  is the effective stiffness the device;  $\frac{k}{m} = \omega_n^2$  and

$\frac{b_m}{m} = 2\zeta\omega_n$ ;  $R$  is the resistive load;  $\zeta$  is the damping ratio;  $L$  and  $L_m$  are the length of the

piezoelectric bimorph and the proof mass, respectively;  $L_b = L_e = L - L_m$  is the effective

electrode length of the top PZT layer;  $c_p$ ,  $c_{sh}$ ,  $t_p$ , and  $t_{sh}$  are the Young's modulus and the

thickness of the PZT layer and the center brass layer, respectively;  $a = 1$  and  $a = 2$  represents

the two piezoelectric layers are wired for series operation and parallel operation, respectively;  $\varepsilon$

is the piezoelectric permittivity; and  $A_{in}$  is the input acceleration to the system.

From Equation 6.1, the system transfer function of the PCB generator can be obtained as:

$$G(s) = \frac{V(s)}{A_{in}(s)} = \frac{\frac{2c_p d_{31} t_p}{k_2 a \varepsilon}}{s^2 + 2\zeta \sqrt{\frac{k}{m}} s + \frac{k}{m} \left(1 + \frac{d_{31}^2 c_p}{\varepsilon}\right)} \quad (6.2)$$

Substituting  $s = j\omega$  into  $G(s)$ , the amplitude of the transfer function is obtained as:

$$|G(j\omega)| = \frac{\frac{2c_p d_{31} t_p}{k_2 a \varepsilon}}{\sqrt{\left[\omega_n^2 \left(1 + \frac{d_{31}^2 c_p}{\varepsilon}\right) - \omega^2\right]^2 + (2\zeta\omega_n\omega)^2}} \quad (6.3)$$

where the maximum amplitude occurs at the driving frequency of the ambient vibration

$\omega_d = \omega_n \sqrt{(1 - 2\zeta^2 + d_{31}^2 c_p / \varepsilon)}$ . The second term  $d_{31}^2 c_p / \varepsilon$  under the square root represents the

piezoelectric effect on the system, since it is well known that the maximum amplitude of the

SDOF system under the forced vibration occurs at  $\omega = \omega_n \sqrt{(1 - 2\zeta^2)}$ .

The  $H_\infty$ -norm of the transfer function  $G(s)$  is defined as the maximum amplitude:

$$\|G\|_\infty = \max_{\omega \in \mathbb{R}} |G(j\omega)| \quad (6.4)$$

Substituting  $\omega_d = \omega_n \sqrt{(1 - 2\zeta^2 + d_{31}^2 c_p / \varepsilon)}$  and  $\omega_n = \frac{k}{m}$  into Equation 6.4, the maximum amplitude of the transfer function can be obtained as:

$$\|G\|_\infty = \frac{k_1 t_p d_{31} m}{a \zeta \varepsilon \sqrt{1 - \zeta^2 + d_{31}^2 c_p / \varepsilon}} \quad (6.5)$$

where  $m = \frac{33}{140} M_{bimorph} + M_{proofmass}$  is the effective mass of the SDOF system, obtained from the single degree-of-freedom (SDOF) model of Ng and Liao (2005).

The above equation relates the maximum voltage frequency response of the piezoelectric energy harvester system with its own geometric configuration. If its dimensions are chosen appropriately, the PCB generator could be made into a band-pass energy harvester with a stable response amplitude over a desired frequency band. For instance, assuming that the norm  $\|G\|_\infty$  is a fixed valued  $\gamma$ , the bimorph length  $L$  and the proof mass thickness  $h_m$  are treated as variables, and other geometric parameters are kept stable, the relationship between  $L$  and  $h_m$  could be obtained as follows:

$$h_m = \frac{1}{c_3} \left( \frac{\gamma}{c_1 L} - c_2 L \right) \quad (6.6)$$

where  $c_1 = \frac{b t_p d_{31}}{2 a \varepsilon \zeta I \sqrt{1 - \zeta^2 + d_{31}^2 c_p / \varepsilon}}$ ;  $c_2 = \frac{33 w}{140} (2 d_p t_p + d_{sh} t_{sh})$ ;  $c_3 = d_m L_m w$ ; and  $d_p$ ,  $d_{sh}$ , and

$d_m$  are the mass density of the piezoelectric layer, the central brass shim, and the proof mass, respectively.

Therefore, based on the above derivation, the identical gain level of the open-circuit

( $R \rightarrow \infty$ ) voltage of the PCB generator over the vibration input can be obtained by appropriately selecting the dimensions of a group of piezoelectric bimorphs and proof masses, resulting in a band-pass piezoelectric energy harvester.

### **FEA Validation of Band-pass Generator Design**

In this section, finite element simulation of a band-pass PCB energy harvester is performed to examine the effectiveness of the above theoretical design. The piezoelectric 3D element SOLID5, PZT material properties of Q220-A4-203Y (Piezo Systems Inc.), and brass proof mass are adopted for FEA simulation, as described previously in Chapter 5. Harmonic analysis of the band-pass generator is performed from 0 – 2000 Hz, with the input vibration amplitude set at  $11.2 \text{ m/s}^2$ . A constant damping ratio of 0.025 is adopted for the simulation. Further, the Large Mass Method (LMM) is adopted to simplify the clamped end configuration of the band-pass generator and increase the efficiency of the finite element calculations.

During the design process, it is assumed the width and thickness of the bimorph and the width and length of the proof mass are fixed. The thickness  $h_m$  of the proof mass can be calculated through Equation 6.6 as the length  $L$  of the PZT bimorph varies. Having defined or calculated all of the parameters of the band-pass generator, the frequency response (Bode plot) of the device can be obtained through the system transfer function shown in Equation 6.2.

Assuming the norm  $\gamma = 1.53$ , the theoretical dimension of a band-pass generator made of a group of PCB generators is shown in Table 9, where the height of the proof mass is calculated as the length of the PZT bimorph varies from 10 mm to 43 mm.

Table 9

Theoretical Dimensions of a Band-pass Generator with  $\gamma = 1.53$ 

Beam	$L$ (mm)	$h_m$ (mm)	Frequency $\omega_d$ , rad/s (Hz)
1	10	10.559	5096.7 (811.2)
2	13	8.012	3057.6 (486.6)
3	16	6.398	2177.3 (346.5)
4	19	5.274	1688.5 (268.7)
5	22	4.439	1378.2 (219.3)
6	25	3.790	1163.8 (185.2)
7	28	3.267	1007.0 (160.3)
8	31	2.833	887.3 (141.2)
9	34	2.464	793.0 (126.2)
10	37	2.146	716.8 (114.1)
11	40	1.865	653.9 (104.1)
12	43	1.616	601.1 (95.7)

Notes: 1. The length and the width of the proof mass:  $w_m = 6.345$  mm and  $L_m = 5.30$  mm .

2. The width and the thickness of the PZT bimorph:  $w = 6.345$  mm,  $t_p = 0.192$  mm, and  $t_{sh} = 0.127$  mm .

Substituting the parameters in Table 9 into the system transfer function in Equation 6.2, the band-pass generator is estimated to generate an open-circuit voltage gain of 26.6 dB over a

frequency band between  $95.7 \text{ Hz}$  and  $811 \text{ Hz}$ , as shown in Figure 53. On the other hand, the normalized open-circuit voltage gain of the FEA simulation is  $26.4 \text{ dB}$  over a frequency band of  $85 \text{ Hz}$  to  $380 \text{ Hz}$ , as is shown in Figure 54.

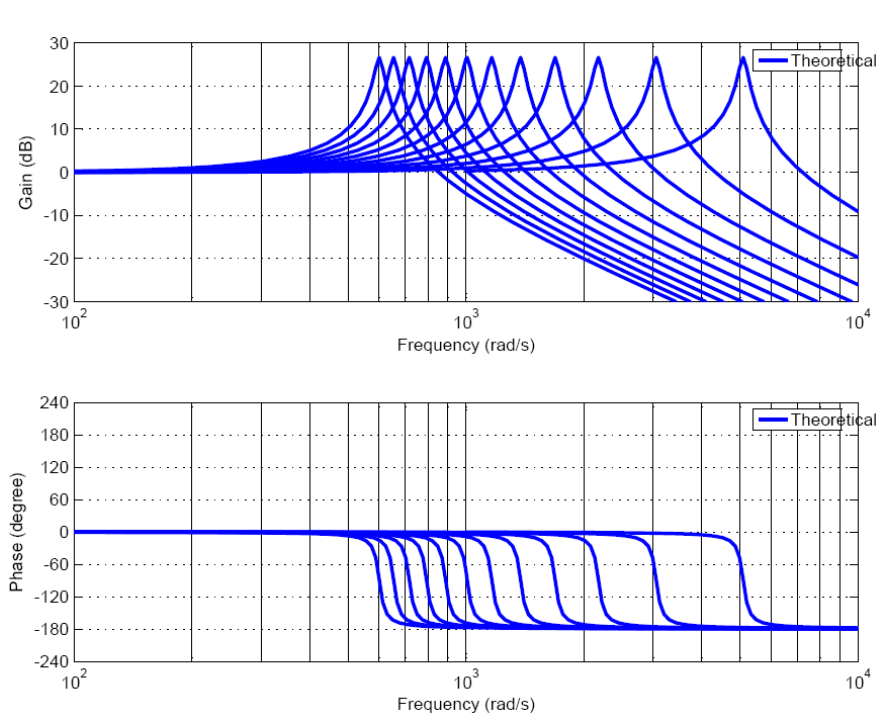


Figure 53. Theoretical Bode Plot of the Band-pass Generator with  $\gamma = 1.53$ .

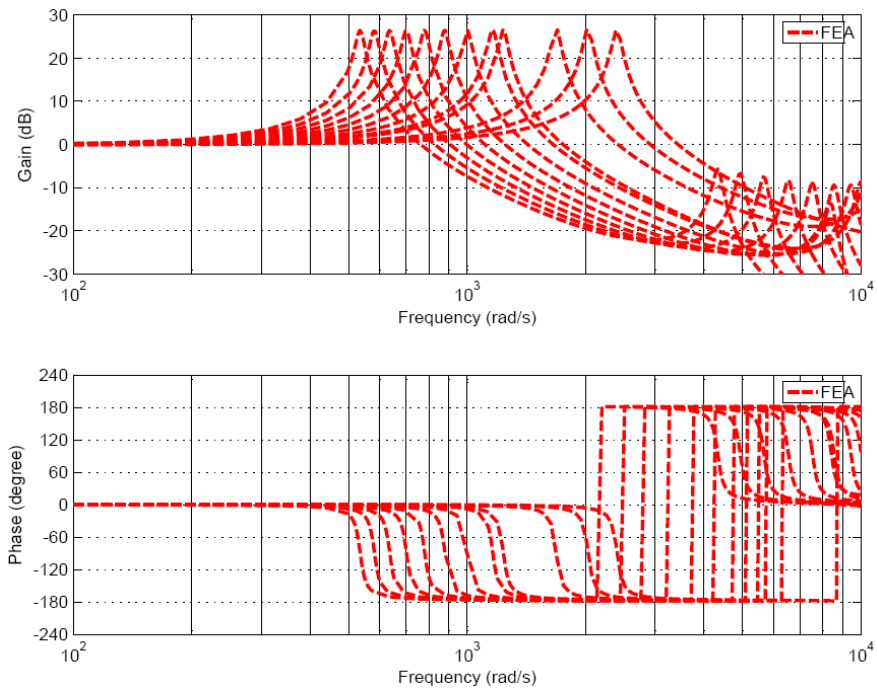


Figure 54. Normalized Frequency Response of the Band-pass Generator FEA Simulation.

It is clear that the voltage amplitude of the theoretical band-pass generator is very close to that of the FEA. However, the indicated applicable frequency band is somehow smaller for the FEA than for Roundy’s (2004) model. The differences are attributed to the Euler beam assumption adopted during the derivation of Roundy (2004), which implies that PCB generators with small length-to-width ratios ( $< 5$ ) cannot be effectively modeled. This is particularly relevant at higher frequencies, where the beam lengths become very short relative to their respective widths. For example, the resonant frequency of the PCB generator with a length-to-width ratio of  $43 \text{ mm} / 6.345 \text{ mm} = 6.77$  is  $95.7 \text{ Hz}$  (Table 9), as compared with the FEA result of  $85 \text{ Hz}$  (Figure 54), leading to a difference in resonant frequency predictions of 12.6%. In contrast, the resonant frequency of the PCB generator with a length-to-width ratio of  $10 \text{ mm} / 6.345 \text{ mm} = 1.576$  is  $811.2 \text{ Hz}$ , as compared with the FEA result of  $380 \text{ Hz}$ , leading to a difference between the two model results of 113%. In addition, due to the single degree-of-

freedom feature of the theoretical model, other modes, rather than the fundamental resonant mode (1<sup>st</sup> bending mode: B1) of the single PCB generator component cannot be demonstrated in the theoretical design plot, while they can be found in the frequency response function (FRF) plot of the FEA simulation, as shown in Figure 54, where the 1<sup>st</sup> torsion (T1) mode of the single PCB generator can be seen.

It is apparent that the FEA of the PCB bimorphs has further applicability to the design and optimization of the band-pass PCB energy harvesters. As demonstrated by the experimental vibration data, the presence of vibration across bands of frequencies provides opportunities for implementation of such devices, as opposed to single-beam PCB energy harvesters that target a single fixed frequency.

### Geometric Feature Design Optimization

The PCB energy harvesters considered in this work thus far have all been conventional cantilevered beams with tip-mounted proof masses, as shown in Figure 55a. Due to the strain-dependent characteristics of the piezoelectric material, the PZT material under the proof mass contributes only negligibly to energy generation. This is demonstrated by the strain distribution along the bimorph shown in Figure 56, where the PZT parts under the proof mass experience negligible strain compared to material at other locations along the PZT bimorph.

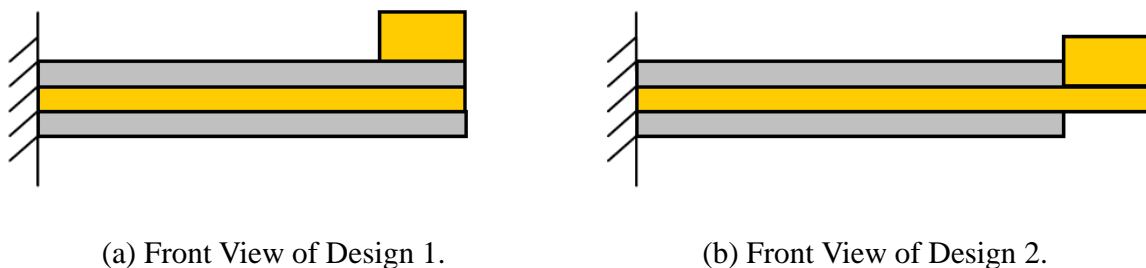


Figure 55. Two Geometric Configurations of PCB Generators.

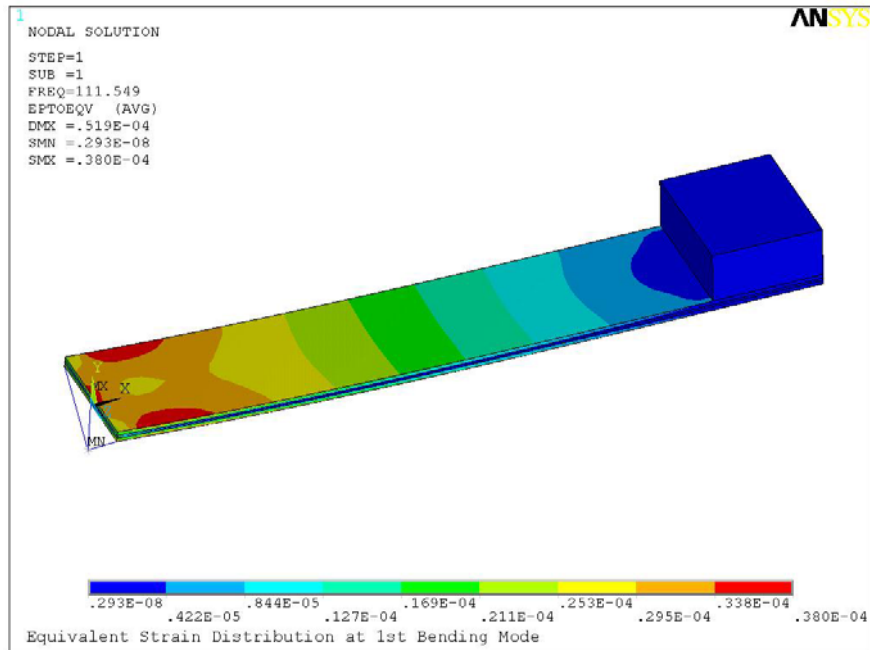


Figure 56. Equivalent Strain Distribution of 1<sup>st</sup> PCB Generator Design.

The above analysis is performed for the PCB generator with the bimorph dimensions of  $34 \text{ mm} \times 6.345 \text{ mm} \times (0.139 \text{ mm} + 0.190 \text{ mm} + 0.139 \text{ mm})$  and the proof mass dimensions of  $5.3 \text{ mm} \times 6.345 \text{ mm} \times 2.464 \text{ mm}$  working under the 1<sup>st</sup> bending mode of  $111.5 \text{ Hz}$ . The piezoelectric material properties are identical with those of Q220-A4-203Y, described in the former chapters.

In order to better utilize the entire piezoelectric materials of the bimorph, the central brass layer is elongated to accommodate the proof mass, as is shown in Figure 55b. In this configuration, the PCB generator has an identical PZT bimorph and proof mass to that shown in Figure 55a. The strain distribution of the 2<sup>nd</sup> PCB generator (Figure 55b) working under the 1<sup>st</sup> bending mode is shown in Figure 57. It is clear that more strain energy is generated at the locations which are the PZT parts under the proof mass for Design 1 (Figure 55a). In addition, the 1<sup>st</sup> resonant frequency of the device is lower than that of Design 1. Due to the strain-

dependent feature of the piezoelectric materials, more electrical energy will be generated under this configuration.

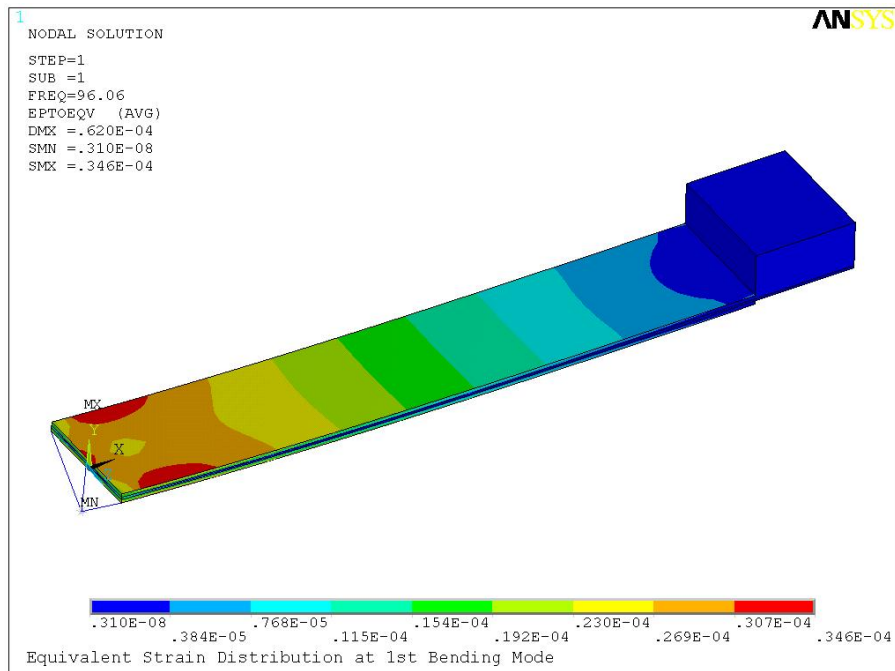
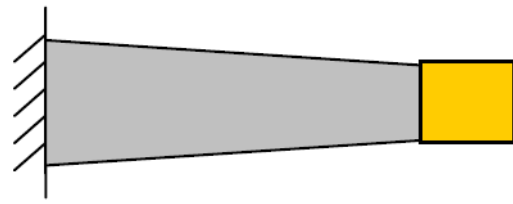


Figure 57. Equivalent Strain Distribution of 2<sup>nd</sup> PCB Generator Design.

Further examination of Figures 56 and 57 indicates that most of the strain in the PCB is occurring at locations close to the clamped end of the PZT bimorph. The lifetime of the PCB generator can be shortened if these parts are damaged due to excessive stress at those locations. Also, much of the PZT along the beam is poorly used and serves mostly as structural support for the proof mass. To decrease the potential for excessive stresses at the base of the beam and to obtain a more efficient use of the PZT material, a trapezoidal shape could be used. Such a device is shown in Figure 58b, where the total area size of the PZT bimorph is equal to that of Design 1 (Figure 58a), and the proof mass is kept identical.



(a) Top View of Design 1.



(b) Top View of Design 3.

Figure 58. Two Geometries of PCB Generators.

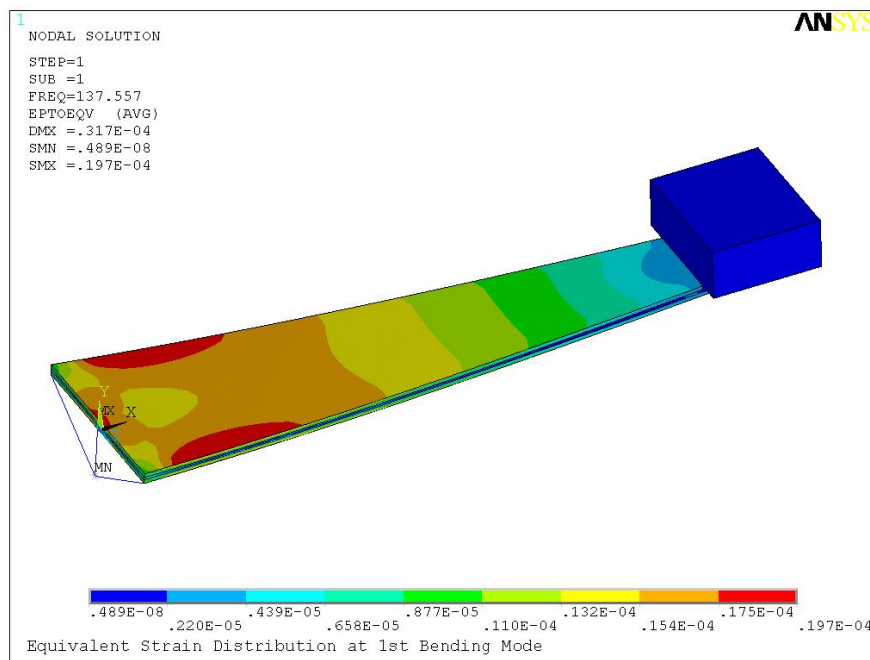


Figure 59. Equivalent Strain Distribution of 3<sup>rd</sup> PCB Generator Design.

The strain distribution of Design 3 is shown in Figure 59. It can be seen that the maximum strain is  $0.197 \times 10^{-4}$ , which is approximately half of that for Design 1 with a maximum strain of  $0.380 \times 10^{-4}$ . Nevertheless, due to more PZT parts allocated to the high strain area (close to the clamped end), and less PZT parts under the proof mass, the electrical energy generation can still be as large as that of Design 1, as can be seen in the Figure 60, where the open-circuit voltage of the three above designs are presented. It is clear that Design 1 and Design 3 have almost the same open-circuit voltage amplitude, despite the bias between their resonant

frequencies. In addition, it can be seen that the voltage amplitude of Design 2 is higher than that of Design 1, due to the fact that the proof mass is relocated onto the central elastic layer, and more strain energy can be generated in this configuration.

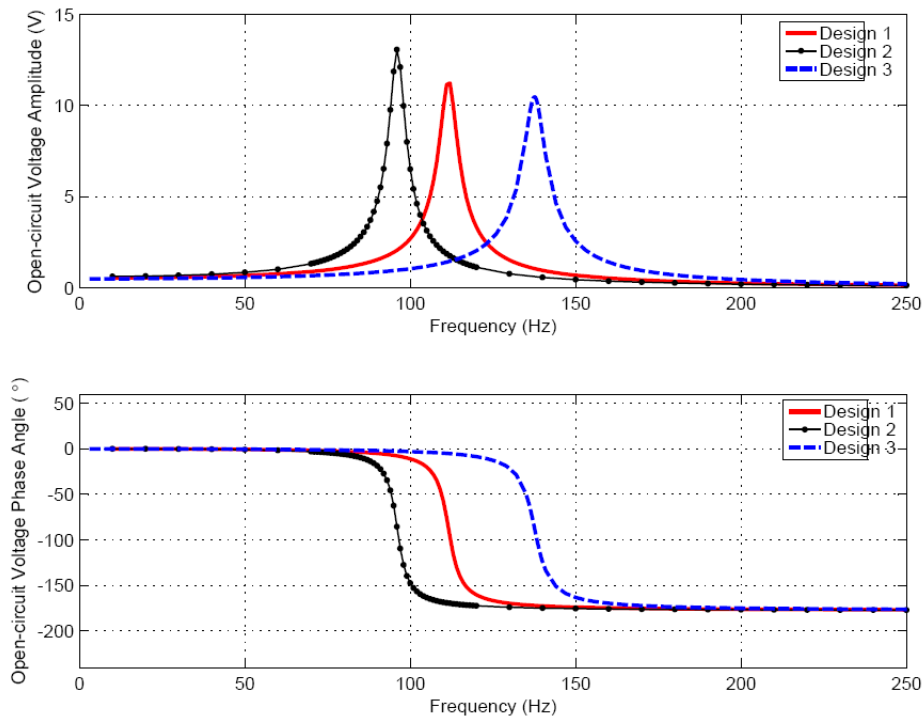


Figure 60. Open-Circuit Voltage Comparison of Three PCB Generator Designs.

### Summary

In this chapter, design optimization of a PCB generator is carried out in three categories, including single rectangular PCB generator optimization, band-pass design optimization, and alternative geometric design optimization. First, a Genetic Algorithm (GA) was used to perform multi-parameter optimization for a single PCB generator. Several sets of the parameters were obtained that corresponded to specific constraint conditions. FEA of the PCB energy harvesters with the optimized parameters validates the GA results and reveals the resonant frequency inaccuracy of the theoretical model used for GA calculation. The second optimization involved

targeting of vibration acting across a band of frequencies. A band-pass generator consisting of a group of PCB generators was derived based on the voltage model of Roundy (2004), and the FEA was carried out to validate the band-pass generator design, although there was a frequency band bias between the analytical model and the FEA. Third, new design features for the PCB generator were presented. Due to the strain-dependent characteristics of the piezoelectric materials, the proof mass is relocated onto the top surface of the central elastic layer, which leads to more electrical energy generation, due to more strain energy generated across the PZT bimorph. Furthermore, in order to increase the life time of the PCB generator, the trapezoidal configuration is compared against the rectangular one. The result shows that the strain in the trapezoidal configuration is almost half that seen in the standard rectangular configuration, while the generated open-circuit voltages are still quite similar. In summary, a great deal of potential for design optimization of a PCB generator is seen.

## CHAPTER 7

### CONCLUSIONS AND RECOMMENDATIONS

#### **Conclusions**

The objectives of this work were to examine analytical models for a piezoelectric cantilever bimorph (PCB) energy harvester and to demonstrate how those models might be used to optimize such a device. A background and review of the literature concerning piezoelectric energy harvesting was presented first. Due to the flexibility of varying the harvester's resonant frequency by modifying the amount of proof mass, the geometric configuration of a PCB with a tip-mounted proof mass was selected for further investigation. Second, due to the importance of matching the resonant frequency of the PCB generator with that of the ambient vibration, a new analytical model for the resonant frequency of the PCB generator was developed using the Rayleigh-Ritz method and Lagrange's equation of motion. That model was then compared with a theoretical model in the literature, a finite element analysis (FEA), and experimental data. In addition, the geometric effects of the PCB generator on its resonant frequency are also studied during the process of model validation. The new analytical frequency model showed good potential for predicting the natural frequency of the PCB. A modified model for the voltage and power output of the PCB generator was then developed, based on the premise that the PZT parts under the proof mass generate negligible strain energy generation and thus the negligible electrical energy conversion. As a result, the PZT parts under the proof mass are treated only as elastic materials without piezoelectric effect. The modified model was then compared against the

original model on which it was based and two other analytical models in the literature for accuracy in predicting the open-circuit and closed-circuit voltage and power outputs. The experimental result reveals that the modified model has a better prediction than the original model, while having pros and cons as compared with the other two analytical models in the literature. An FEA was then performed to study the dynamic response of the PCB energy harvester when subjected to harmonic excitation. Specific outputs of the FEA were the PCB tip displacement and the electrical potential (open-circuit voltage) generation across the PZT bimorph. The result shows that FEA results are very close to the experimental results in terms of not only peak frequency, but also peak amplitude. As a result, it was concluded that the FEA is appropriate for use as a validation tool for the design and optimization of a PCB energy harvester.

After establishment of the analytical models and the FEA for the PCB generator, three different approaches to design optimization were demonstrated, including multi-parameter optimization of a single PCB generator using a genetic algorithm (GA), design of a band-pass PCB energy harvester system using a group of discrete PCB energy harvesters, and the use of alternate PCB geometries with consideration to improving the utilization of the PZT material and potentially increasing the lifetime of a PCB device. It is apparent that a number of techniques are available for optimizing a PCB energy harvester.

### **Recommendations for Further Studies**

In this work, the analytical modeling and design optimization of a PCB energy harvester have been studied, with a focus on the mechanical aspects of the design. Certainly, additional design considerations include the electrical aspects of the device, such as determining a suitable DC-DC converter or voltage regulator for the electrical energy storage and the design of working

cycles for the electronics that depend on the power output of the PCB generator. However, additional mechanical aspects can be considered as well. Specifically, future studies for design of a PCB energy harvester might be:

(1). The close-circuit voltage prediction does not match well with the experiment, and close-circuit power based on the square of close-circuit voltage compounds the error. Internal loading investigation can be performed to refine the voltage and power model of the PCB generator.

(2). Analytical plate models for the PCB generator with a proof mass on the free tip could be developed, in order to realize a more precise approximation of the resonant frequency of the PCB generator than those models based on the Euler beam theory.

(3). A PCB energy harvester with a resonant frequency that can be online tuned to match the frequency of the ambient vibration, and thus maximize the energy harvesting, can be designed. Approaches for realizing an online tunable PCB energy harvester might include: ① investigation of the possibility of using energy harvested from the energy-harvesting layer of the bimorph to power a simple controller circuit that could automatically adjust the capacitance of PCB to keep the resonant frequency of the structure appropriately tuned; ② investigation of the use of passive shunt capacitors to change the stiffness of the tuning layer and hence the resonant frequency of the bimorph bender. To implement this concept on a real structure, a capacitor array could be used.

(4). Due to the rapid development of the Nano-tube transducer, there is a potential to utilize it as an electrical energy harvester, although currently most of the electrolytes necessary for the conversion are liquid, and solid-state electrolytes are developed rapidly. In addition, nano-tube reinforced piezoelectric energy harvesters is also a promising field, since the nano-

tubes can generate higher strain than the PZT transducers, due to their remarkable mechanical properties.

## REFERENCES

- Ajitsaria, J., Choe, S., Shen D., & Kim, D. (2007). Modeling and analysis of a bimorph piezoelectric cantilever beam for voltage generation. *Smart Structures and Systems*, 16(2), 447-454.
- Allik, H. & Hughes, T. (1970). Finite element method for piezoelectric vibration. *International Journal for Numerical Methods in Engineering*, 2: 151-157.
- Amirtharajah, R. & Chandrakasan, A. (1998). Self-powered signal processing using vibration-based power generation. *IEEE Journal of Solid-State Circuits*, 33(5), 687-695.
- ANSYS®, Inc. (2005). Theory reference, *ANSYS® Release 10.0*.
- Baldwin Sawyer, C. (1931). The use of Rochelle salt crystals for electrical reproducers and microphones, *Proc. RE*, 19(11), 2020-2029.
- Benjeddou, A., Trindade, M. & Ohayon, R. (1999). New shear actuated smart structure beam finite element. *AIAA Journal*, 37(3): 378-383.
- Cao, X., Chiang, W., King, Y. & Lee, Y. (2007). Electromagnetic energy harvesting circuit with feedforward and feedback DC-DC PWM boost converter for vibration power generator system. *IEEE Transactions on Power Electronics*, 22(2), 679-685.
- Chen, C. & Priya, S. (2006). Electric Energy Generator. *IEEE Transaction Ultrasonic Ferroelectric Frequency Control*, 53(3), 656-661.
- Chiu, Y., Kuo, C. & Chu, Y. (2007). MEMS design and fabrication of an electrostatic vibration-to-electricity energy converter. *Microsystems Technologies*, 13(1), 1663-1669.
- Choi, W., Jeon, Y., Jeong, J., Sood, R. & Kim, S. (2006). Energy harvesting MEMS device based on thin film piezoelectric cantilevers. *Journal of Electroceram*, 17: 543-548.
- Churchill, L., Hamel, J., Townsend, P. & Arms, W. (2003). Strain energy harvesting for wireless sensor networks. *Proceedings of SPIE*, 5055: 319-327.
- David, H. (2000). Harmonic sweep. <http://ansys.net/tips/harmonic-large-mass-method.pdf>.
- Dong, X., Meng, G. & Peng, J. (2006). Vibration control of piezoelectric smart structures based on system identification technique: Numerical simulation and experimental study, *Journal of Sound and Vibration*, 297: 680-693.

- Eggborn, T. (2003). Analytical models to predict power harvesting with piezoelectric materials. Master Thesis, Virginia Polytechnic Institute and State University, VA.
- Ericka, M., Vasic, D., Costa, F., Poulin, G. & Tliba, S. (2005). Energy harvesting from vibration using a piezoelectric membrane. *Journal of Physics IV France*, 128: 187-193.
- Holland, J. H. (1975). *Adaptation in Natural and Artificial System*. Ann Arbor: The University of Michigan Press.
- Horowitz, S., Sheplak, M., Cattafesta, L. & Nishida, T. (2006). A MEMS acoustic energy harvester. *Journal of Micromechanics and Microengineering*, 16(8), 174-181.
- ANSI / IEEE Standard. (1988). IEEE Standard on Piezoelectricity, 176-1987.
- Ikeda, T. (1990). *Fundamentals of Piezoelectricity*. New York: Oxford University Press.
- Jeon, Y., Sood, R., Jeong, J. & Kim, S. (2005). MEMS power generator with transverse mode thin film PZT. *Sensors and Actuators A*, 122(1), 16-22.
- Kim, S. (2002). Low power energy harvesting with piezoelectric generators. Dissertation, University of Pittsburgh.
- Kim, S., Johnson, T. & Clark, W. (2004). Harvesting energy from a cantilever piezoelectric beam. *Proceedings of SPIE – The International Society for Optical Engineering*, 5386, 259-268.
- Lerch, R. (1990). Simulation of piezoelectric devices by two- and three- dimension finite elements. *IEEE Transactions on Ultrasonics, Ferroelectrics, and Frequency Control*, 37(2), 233-247.
- Lu, B., Wang, L. and Ai, S. (2002). Application about large mass method in ANSYS dynamic analysis. *Power System Engineering*, 18 (5), 63-64.
- Malgaca, L. & Karagulle, H. (2009). Simulation and experimental analysis of active vibration control of smart beams under harmonic excitation. *Smart Structures and Systems*, 5(1), 55-68.
- MatWeb.com. Material properties for Aluminum, Brass, Lead, Steel, Titanium and Tungsten.
- Meninger, S., Mur-Miranda, J., Amirtharajah, R., Chandrakasan, A. & Lang, J. (2001). Vibration-to-electricity energy conversion. *IEEE Transaction on Very Large Scale Integration (VLSI) Systems*, 9(1), 64-76.
- Miao, P., Holmes, A., Yeatman, E. & Green, T. (2003). Micro-machined variable capacitors power generation. *Proceedings of Institute of Physics*, Edinburgh, 23-27 March 2003, 53-

58.

- Mitcheson, P., Green, T., Yeatman, E. & Holmes, A. (2004). Architectures for vibration-driven micropower generators, *Journal of Micromechanical Systems*, 13(3), 429-440.
- Ng, T. H. & Liao, W. H. (2005). Sensitivity Analysis and Energy Harvesting for a Self-Powered Piezoelectric Sensor. *Journal of Intelligent Material Systems and Structures*, 16(10), 785-797.
- Paradiso, J. & Starner, T. (2005). Energy scavenging for mobile and wireless electronics. *IEEE Pervasive Computing*, 4, 18-27.
- Park, C. (2001). On the circuit model of piezoceramics. *Journal of Intelligent Material Systems and Structures*, 12(7), 515-522.
- Priya, S. (2007). Advances in energy harvesting using low profile piezoelectric transducers. *Journal of Electroceram*, 19(3), 165-182.
- Priya, S. (2005). Modeling of electrical energy harvesting using piezoelectric windmill. *Applied Physics Letters*, 87(18), 184101-184103.
- Rao, S. (2003). Mechanical Vibrations. New Jersey, Pearson Prentice Hall.
- Richards, C., Anderson, M., Bahr, D. & Richards, R. (2004). Efficiency of energy conversion for devices containing a piezoelectric component. *Journal of Micromechanics and Microengineering*, 14(5), 717-721.
- Roundy, S., Wright, P. K., & Rabaey, J. (2003A). A study of low level vibrations as a power source for wireless sensor nodes. *Computer Communications*, 26(11), 1131-1144.
- Roundy, S. (2003B). Energy scavenging for wireless sensor nodes with a focus on vibration to electricity conversions. Dissertation, the University of California, Berkeley.
- Roundy, S. and Wright, P. (2004). A piezoelectric vibration based generator for wireless electronics, *Smart Materials and Structures*, 13(8), 1131-1142.
- Roundy, S. (2005). On the effectiveness of vibration-based energy harvesting. *Journal of Intelligent Material Systems and Structures*, 16(10), 809-823.
- Roundy, S., Leland, E. S., Baker, J., Carleton, E., Reilly, E., Lai, E., Otis, B., Rabaey, J. M., Wright, P. K. & Sundararajan V. (2005). Improving power output for vibration-based energy scavengers. *IEEE Pervasive Computing*, 4(1), 28-36.
- Shahruz, S. (2006A). Design of mechanical band-pass filters for energy harvesting. *Journal of Sound and Vibration*, 292(3), 987-998.

- Shahruz, S. (2006B). Design of mechanical band-pass filters with large frequency bands for energy harvesting. *Mechatronics*, 16(9), 523-531.
- Shahruz, S. (2008). Design of mechanical band-pass filters for energy scavenging: multi-degree-of-freedom models. *Journal of Vibration and Control*, 14(5), 753-768.
- Shen, D., Ajitsaria, J., Choe, S. & Kim, D., J. (2006). The optimal design and analysis of piezoelectric cantilever beams for power generation. *Proc. Mat. Res. Soc. Symp.* 888, 271-277.
- Smits, J. & Choi, W. (1991A). The constituent equations of piezoelectric heterogeneous bimorphs. *IEEE Transactions on Ultrasonics, Ferroelectrics and Frequency Control*, 38(3), 256-270.
- Smits, J., Dalke, S. & Cooney, T. (1991B). The constituent equations of piezoelectric bimorphs. *Sensors and Actuators A*, 28(1), 41-61.
- Sodano, H., Inman, D. & Park, G. (2004). A review of power harvesting from vibration using piezoelectric materials. *The Shock and Vibration Digest*, 36(3), 197-205.
- Sodano, H., Inman, D. & Park, G. (2005). Comparison of piezoelectric energy harvesting devices for recharging batteries. *Intelligent Material Systems and Structures*, 16(10), 799-807.
- Stordeur, M. & Stark, I. (1997). Low power thermoelectric generator — self-sufficient energy supply for micro systems. *16th International Conference on Thermoelectrics*, 575-577.
- Tashiro, R., Kabei, N., Katayama, K., Tsuboi, F. & Tsuchiya, K. (2002). Development of an electrostatic generator for a cardiac pacemaker that harness the ventricular wall motion. *Journal of Artificial Organs*, 5, 239-245.
- Tongue, B. (2002). *Principles of Vibration* (2<sup>nd</sup> Edition). Oxford Press.
- U.S. Department of Energy. (2006). Solar Energy Technologies Program: Multi-year program plan 2007-2011.
- U.S. Energy Information Administration. (2009). <http://www.eia.doe.gov>
- Wang, K. (2001). Modeling of piezoelectric generator on a vibrating beam. For Completion of Class Project in ME 5984 Smart Materials, Virginia Polytechnic Institute and State University.
- Wang, Q. & Cross, E. (1999). Constitutive equation of symmetrical triple layer piezoelectric benders. *IEEE Transactions on Ultrasonics, Ferroelectrics, and Frequency Control*, 46(6), 1343-1451.

- Wang, Q., Du, X., Xu, B. & Cross, E. (1999). Theoretical analysis of the sensor effect of cantilever piezoelectric benders. *Journal of Applied Physics*, 85(3), 1702-1712.
- Williams, C. & Yates, R. (1996). Analysis of a micro-electric generator for microsystems. *Sensors and Actuators A*, 52(3), 8-11.
- Wu, D., Chien, W., Yang, C. & Yen, Y. (2005). Coupled-field analysis of piezoelectric beam actuator using FEM, *Sensors and Actuators A*, 118(4), 171-176.
- WWEA, World wind energy report 2009, 9<sup>th</sup> World Wind Energy Conference & Exhibition Large-scale Integration of Wind Power, Istanbul, Turkey, 15-17, June, 2010.
- Xie, Z. (2008). Enhanced modeling and design optimization of constrained layer damped structure. *Dissertation*. The University of Alabama, Tuscaloosa.
- Zhang, L. & Williams, K. (2009). Enhanced modeling of resonant frequency of piezoelectric bimorph cantilever energy harvester. *Proceedings of the SPIE*, 7292(2), 72923N-72923N-9.
- Zhang, L. & Williams, K. (2010A). Comparative study on the modeling of PZT cantilever bimorph energy harvester. In preparation.
- Zhang, L. & Williams, K. (2010B). Dynamic response analysis of piezoelectric cantilever bimorph energy harvester. In preparation.
- Zhang, L. & Williams, K. (2010C). Band-pass design optimization of piezoelectric cantilever bimorph energy harvester. In preparation.